Thermal stability of magnetron sputtered W/HfO_2 and Ir/HfO_2 thin films used as selective emitter in thermophotovoltaic applications

Vom Promotionsausschuss der

Technischen Universität Hamburg

zur Erlangung des akademischen Grades

Doktor der Naturwissenschaften (Dr. rer. nat.)

genehmigte Dissertation

von

Gnanavel Vaidhyanathan Krishnamurthy

aus

Coimbatore, Indien

2023

Aufzählung der Gutachter - Prof. Dr. rer. nat. Manfred Eich

Prof. Dr. rer. nat. Gerold Schneider

Tag der mündlichen Prüfung - 27-Jun-2023

DOI : https://doi.org/10.15480/882.8364

ORCID : https://orcid.org/0000-0002-4353-7858

Contents

1 Introduction **10**

1.1 Background 15

1.2 Outline of the thesis 16

2 Experiments **18**

2.1 Thin film Preparation 18

2.2 Annealing experiments 20

2.3 Characterization Methods 21

2.3.1 X-Ray diffraction (XRD) 21

2.3.2 X-Ray reflectivity (XRR) 32

2.3.3 Fourier Transform Infrared Spectroscopy (FTIR) . . . 33

2.3.4 Surface Profilometer 34

2.3.5 Electron Microscopy 35

3 Tungsten - Hafnia selective emitter **37**

3.1 Properties and morphology of tungsten thin films 37

3.1.1 Polymorphs of tungsten thin films 38

3.1.2 Structure and microstructure of tungsten thin films based on film thickness 42
3.1.3 Structure and microstructure of tungsten thin films based on Ar gas pressure 44
3.2 Hafnia - layer thickness, structure and phase formation 46
3.3 W/HfO_2 - Metamaterial 52
3.3.1 Mechanism of oxidation in W 54
3.3.2 Ex-situ annealing in different vacuum pressure 56
3.3.3 Ex-situ annealing in inert gas atmosphere 64
3.4 Determination of the thermal stability of HfO_2/W/HfO_2 system by in-situ XRD 67

4 Iridium - Hafnia selective emitter **92**
4.1 Properties and morphology of iridium thin films 92
4.2 Thermal stability of Ir as a function of temperature and time 98
4.3 Thermal stability of Ir as a function of O_2 partial pressure . . 112
4.4 Durability between Ir/HfO_2 and W/HfO_2 selective emitters . . 117

5 Conclusion and Outlook **122**

Bibliography **128**

A Thermal validation of various materials **143**
A.1 W- strip 143
A.2 MgO substrate 148

A.3 Sapphire substrate (Al_2O_3) 150

List of Tables **157**

List of Figures **159**

Abstract

High-temperature stability and long-term operation of selective emitters are the two crucial parameters required to allow high radiative power and increased efficiency of a selective emitter used in a thermophotovoltaic system (TPV). At high temperatures, thermally activated processes like diffusion, grain growth, phase transformation, relaxation, chemical reactions like oxidation and sublimation of metal oxides become active and the thermal stability of the thin films remains a great challenge. This thesis investigates and analyzes the thermal stability and the degradation mechanism in a 1D multilayered metamaterial selective emitter containing combinations of two thin-film material systems, W/HfO_2 and Ir/HfO_2 fabricated using magnetron sputtering and characterized by x-ray diffraction. It is quite challenging to perform high temperature in-situ annealing experiments (up to 2000 °C) using strip heaters and estimate the correct temperature of the sample. Therefore, a know-how for high temperature validation of different materials using x-rays is also elaborated.

In the first part annealing experiment were performed on a W/HfO_2 se-

lective emitters at different temperature ranges between 1000 °C - 1500 °C, and at different vacuum pressure conditions between 2×10^{-6} mbar - 2×10^{-2} mbar. The W/HfO_2 selective emitter was stable for at least 6 h at 1400 °C and 2×10^{-5} mbar that is one of the highest reported temperature stability so far. In addition, a detailed analysis is presented on the degradation mechanism of a 3-layer-system, HfO_2/W/HfO_2 system using in-situ x-ray diffraction between 300 °C and 1520 °C. The major cause of failure in a W/HfO_2 selective emitters is due to oxidation of W followed by sublimation of volatile WO_x. An activation energy of 1.2 eV is calculated for the latter process. In the case of the HfO_2, polymorphic phase transformation is observed. The change of the crystalline phase cause an increase in the volume of the unit cell, which leads first to the formation of voids and later generation of transport channels along the grain boundaries in the ceramic layer.

In the second part, a systematic approach is followed to test the thermal stability of the metal against oxidation and durability in an Ir/HfO_2 selective emitter. Initially, in-situ x-ray diffraction experiments were performed on a 3-layer-system (HfO_2/Ir/HfO_2), between 800 °C - 1100 °C at 2×10^{-6} mbar, using in-situ x-ray diffraction. Ir exhibits very good thermal stability up to 1000 °C supported by hafnia as an excellent top layer. At temperatures above 1000 °C, the Ir layer starts to agglomerate, this means that the driving force is minimization of surface free energy. The thermal stability was also validated by performing ex-situ annealing experiments at different pressures

between 2×10^{-5} mbar and 1 bar, on a 3-layer-system, which is stable up to 100 h at 1000 °C, 2×10^{-2} mbar. Satellite reflections are observed around the primary (111) peak and serves as an important marker to validate the layer stability.

In the W/HfO_2 system, W layer shows good thermal stability up to 1400 °C for 6 h at 2×10^{-5} mbar. But for 20 h at 1000 °C and 2×10^{-5} mbar, W in a 3-layer-system starts to oxidize and the volatile W-oxide sublimates. However, the oxidation resistance of the W layer is not validated for durability above 1000 °C, since a good selective emitter for practical application has to perform at an elevated temperature for a longer period of time. In the case of the Ir/HfO_2 system, Ir shows good oxidation resistance and layer stability up to 1000 °C. Nevertheless above 1000 °C the thermal stability of the layer is affected by grain growth and relaxation process. Therefore, a final comparison is made between a W/HfO_2 and Ir/HfO_2 metamaterial at 1000 °C, 2×10^{-2} mbar for 100 h to validate durability. Ir exhibits excellent thermal stability and durability in comparison to W in the latter experimental conditions.

The high-temperature experiments and analysis performed in this thesis present a new perspective on the thermal stability that can be practically achieved and enable the development of selective emitters for next-generation TPV systems.

Kurze Zusammenfassung

Hochtemperaturstabilität und Langlebigkeit eines selektiven Emitters sind die beiden entscheidenden Parameter, um hohe Strahlungsleistung und einen höheren Wirkungsgrad beim Einsatz in einem thermophotovoltaischen System (TPV) zu erzielen.

Bei hohen Temperaturen sind thermisch-aktivierte Prozesse wie Diffusion, Kornwachstum, Phasentransformation, Erholung, chemische Reaktionen insbesondere Oxidation sowie Sublimation von Metalloxiden wirksam und somit stellt die thermische Stabilität eines Dünnschichtsystems eine besondere Herausforderung dar. In dieser Arbeit wurden die thermische Stabilität und die Versagensmechanismen einer 1D-Metamaterial-Vielfachschicht als selektiver Emitter untersucht und analysiert. Zwei Dünnschichtsysteme: W/HfO_2 und Ir/HfO_2 standen aufgrund ihrer besonderen Materialeigenschaften (hoher Schmelzpunkt und niedriger Vakuumdampfdruck) im Fokus. Sie wurden mittels Magnetron sputtering hergestellt und durch Röntgenbeugung (XRD) untersucht. Die in-situ Hochtemperaturuntersuchungen (bis zu 2000 °C) unter Verwendung von Heizbändern und die Abschätzung der Proben-

temperatur waren herausfordernd, dadurch wurde ein spezielles Wissen für die Hochtemperaturvalidierung unterschiedlicher Materialien aufgebaut.

Der erste Teil der Arbeit zeigt die Heizexperimente an selektiven W/HfO_2-Emitterschichten in verschiedenen Temperatur- (1000 °C bis 1520 °C) und Vakuumdruckbereichen (2×10^{-2} mbar bis 2×10^{-6} mbar). Eine selektive W/HfO_2-Emitterschicht ist bis 6 h bei 1400 °C und 2×10^{-5} mbar stabil, welches bisher einer der weltweit höchsten erreichten Werte ist. Darüber hinaus erfolgte eine detaillierte in-situ Röntgenanalyse am Schichtsystem $HfO_2/W/HfO_2$ zwischen 300 °C und 1520 °C im Hinblick auf die Mechanismen, die zu strukturellen und mikrostrukturellen Veränderungen wie Relaxation, Phasenumwandlung, Kornwachstum und schließlich zum Versagen (Degradation) führen. Der Hauptgrund des Versagens in einer selektiven W/HfO_2-Emitterschicht ist auf die Oxidation des Wolframs gefolgt durch eine Sublimation des flüchtigen Wolframoxids zurückzuführen. Für diesen Prozess wurde eine Aktivierungsenergie von 1.2 eV abgeschätzt. Im Falle des HfO_2 wurde eine polymorphe Phasentransformation beobachtet. Die strukturelle Umwandlung der Phasen verursacht einen Anstieg des Volumens der Einheitszelle, der wiederum zur Bildung von Leerstellen, Poren sowie der Entstehung von Transportkanälen entlang der Korngrenzen in der keramischen Schicht führt.

Im zweiten Teil wird ein systematischer Ansatz verfolgt, um die thermische Stabilität des Metalls Iridium gegen Oxidation und die Lebensdauer der selektiven Ir/HfO2-Emitterschicht zu testen. Zunächst wurden in-situ

XRD-Untersuchungen am Schichtsystem: HfO_2/Ir/HfO_2 zwischen 800 °C – 1100 °C bei 2×10^{-6} mbar durchgeführt. Iridium zeigte eine sehr gute thermische Stabilität bis zu 1000 °C unterstützt durch HfO_2 als hervorragende Deckschicht. Bei Temperaturen über 1000 °C begann die Iridium-schicht zu agglomerieren, was bedeutet, dass die treibende Kraft eine Minimierung der Oberflächenenergie ist. Die thermische Stabilität wurde auch durch ex-situ XRD-Untersuchungen bei unterschiedlichen Drücken von 1 bar bis zu 2×10^{-5} mbar im Schichtsystem HfO_2/Ir/HfO_2 verifiziert, welche bis zu 100 h bei 1000 °C und 2×10^{-2} mbar stabil ist. Satellitenreflexe wurden nahe am primären (111) Ir-Peak beobachtet, die als wichtiger Hinweis für die thermische Stabilität dienen können. Ein finaler Vergleich erfolgte zwischen verschiedenen Metamaterialschichten bestehend aus W/HfO_2 und Ir/HfO_2 bei 1000 °C und 2×10^{-2} mbar. Über 100 h weist Iridium eine exzellente thermische Stabilität im Vergleich zu Wolfram auf. Die in dieser Arbeit durchgeführten Hochtemperaturexperimente und – analysen bieten eine neue Perspektive auf die thermische Stabilität, die in Dünnschichtsystemen praktisch erreicht werden kann und ermöglichen die Entwicklung selektiver Emitter für TPV-Systeme der nächsten Generation.

Chapter 1

Introduction

Fossil fuels still remain the primary source of energy for industries and global energy system, and account up to 75% of primary demand. Electricity generation using natural gas and coal to date is the most used resource for power generation [1].

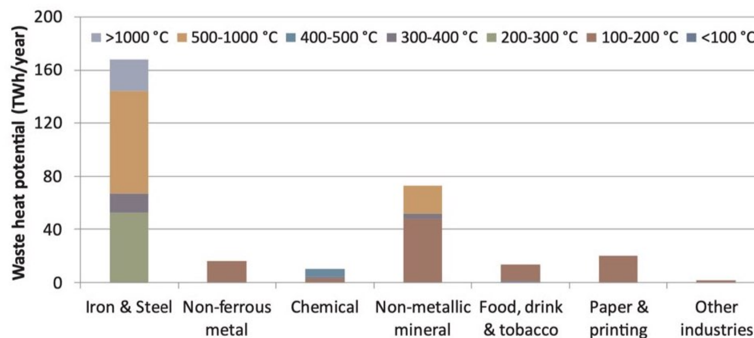

Figure 1.1: Potential waste heat recovery above 1000 °C (4 %) from the iron and steel industry in the UK during 2015 [2].

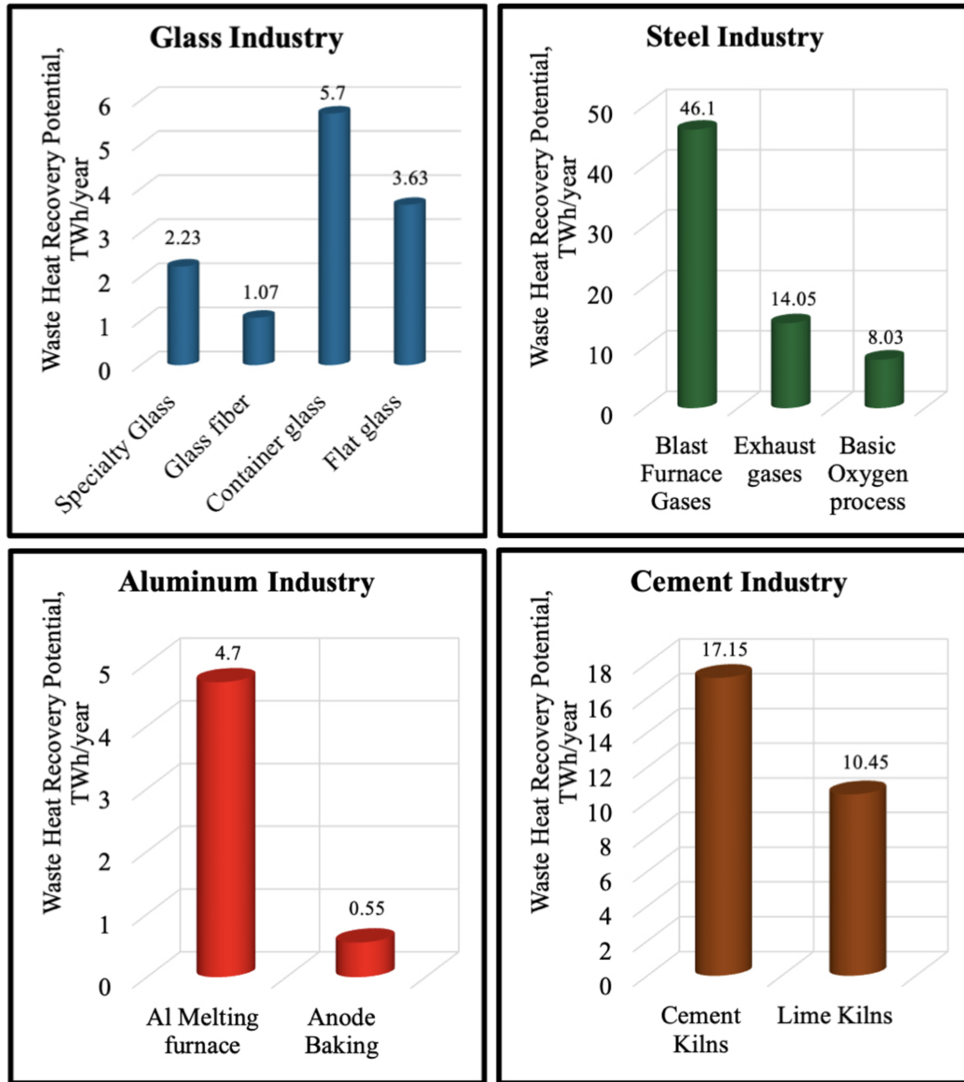

Figure 1.2: Potential waste heat recovery above 1000 °C (3 %) from the glass, steel, aluminum and cement industry in the US during 2014 [3].

A vast portion of the energy consumed by industries ends up as unexploited waste heat. The total waste heat potential estimated in the European

Union (EU) in the year 2015 was 300 TWh/year [2] of which 4% is above 1000 °C (Figure 1.1), it is important to mention that the contribution from renewable energy was 29%. A successful implementation of TPV system will enhance the renewable energy contribution by 10%. The amount of heat wasted by the manufacturing sector in the United States of America (U.S.A) for the year 2014 was 747.6 TWh/year [3], of which 3% is above 1000 °C (Figure 1.2). Depending on the type of industrial processes, waste heat can be generally classified into three categories, high ($>$ 400 °C), medium (100 °C - 400 °C), and low ($<$ 100 °C) [4]. There are numerous methods available for the direct conversion of waste heat into electricity like thermionic generation (TG) [5], thermoelectric generators (TEG) [6], piezoelectric power generation (PEPG) [7], and thermophotovoltaics (TPV) [8].

A TPV system can produce electricity also from fossil fuels [9], solar radiation [10], [11], [12], [13], [14] and radioisotope thermoelectric generators (RITEGs) [15], [16], [17]. The invention of TPV systems dates back to 1956 by Pierre Airgain, who discussed the concept in his lectures at the Massachusetts Institute of Technology (MIT). The basic TPV system (Figure 1.3) consists of a heat source, an emitter, and a photovoltaic (PV)cell.

The emitter in the TPV system is heated to high temperatures, typically above 1000 °C, and its radiant energy is converted to electricity using a PV cell [18], [19], [20], [21]. Hence the emitter functions similar to a blackbody and follows Kirchhoff's radiation law that states, "The energy absorbed at wavelength λ, must equal the energy radiated and this is true for all materials

no matter how different" [22].

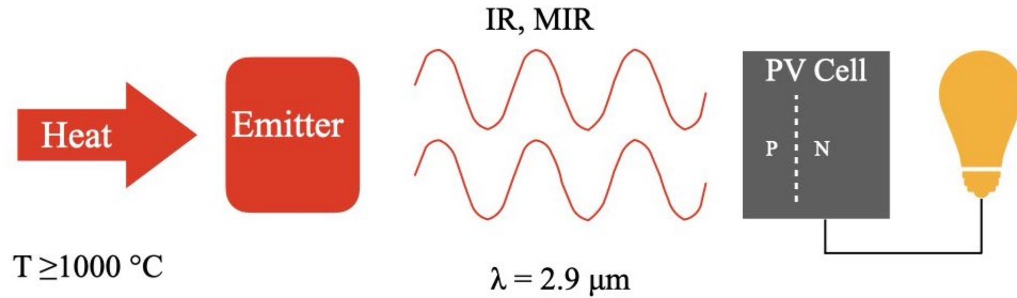

Figure 1.3: Schematic of a thermophotovoltaic system (TPV).

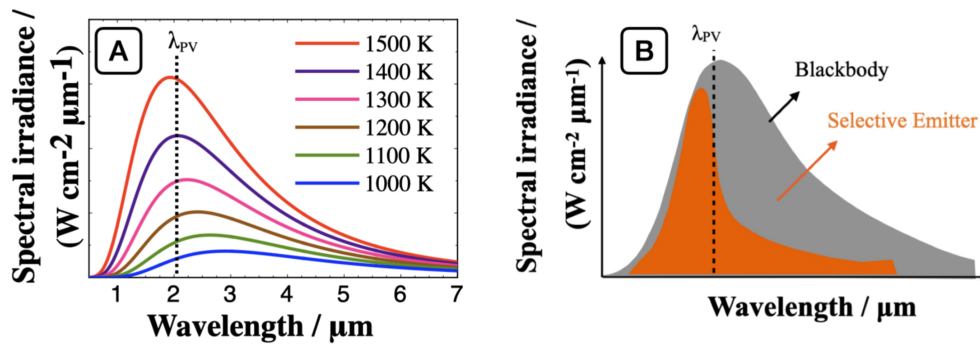

Figure 1.4: (A) Peak maximum shifts towards lower wavelengths for higher temperatures shown according to Wien's displacement law. (B) Suppression of longer wavelengths by a selective emitter to enhance the efficiency of the TPV system.

A typical emission spectrum of a blackbody is shown in Figure 1.4 A. The spectral maximum shifts to shorter wavelengths or higher frequency as

the temperature increases, which is known as Wien's displacement law, and it can be derived from Planck's law of radiation [23]. Therefore, one of the essential parameters for obtaining higher power and efficiency is to operate the emitter at high temperatures, as the radiative power of a blackbody is directly proportional to the T^4 according to Stefan Boltzmann law [24]. The vertical dotted line shown in Figure 1.4 A represents the cutoff wavelength of the PV cell used. Any emission above the cutoff wavelength unless not reflected back to the source is not used in electricity generation and is wasted as heat due to thermalization. However, by using a selective emitter [25], [26], [27], [28], [29], [30], [31], [32] shown in Figure 1.4 B, the efficiency of the system can be substantially improved. Selective emitters are designed to precisely emit spectrally tailored radiation that matches the bandgap of the PV cell and suppress long-wavelength radiation, i.e., they provide an emissivity ϵ close to 1 for E $>$E$_g$ and ϵ almost 0 for E $<$ E$_g$, where E is the thermal photon energy and E$_g$ is the bandgap energy which is equal to the cutoff wavelength of the PV cell (E$_g$= 1/ λ_{PV}). If the selected PV cells have a bandgap energy E$_g$ between 0.5 - 0.7 eV [33], [34] then the selective emitter should operate at a temperature of at least 900 °C. Therefore, the high-temperature stability of the selective emitter is the most critical parameter and is the primary focus of this thesis. Photonic crystals [35], [36], thin-film resonators [37], gratings and metasurface [38], [39], and multilayered metamaterials [40], [41] are examples of selective emitters. As the focus is on high-temperature operation, the ideal materials of interest are Mo, Ta, W,

Ir, Os, Nb, Al_2O_2, ZrO_2, and HfO_2 because of their high melting point [42], [43], [44].

1.1 Background

There exists no selective emitter in nature. One way of fabricating such a sub-wavelength structure to bring in artificial properties is termed metamaterials [45]. An example of a metamaterial, a nano structured multilayer with special optical properties is a hyperbolic metamaterial (HMM) [46]. These possess extreme anisotropy and have a large photonic density of states in certain wavelength ranges and directions. The most common realization of a hyperbolic metamaterial is a layered metal-dielectric combination and numerous combinations have been demonstrated e.g. Ag/Al_2O_3 [47], Ag/TiO_2 [45], Au/Al_2O_3 [48], SiO_2/SiC/SiO_2 [49], W/HfO_2 [40]. As the selective emitter is subjected to high operating temperatures, the primary structural failure is due to oxidation of the metal [50], [51], [52], surface diffusion [53], [54], [55], delamination and cracking [56] due to stress in the multilayers.

Based on the literature survey about failure mechanism on high temperature materials, open questions were defined for this thesis:

- How does metal in the multilayer oxidize? How does the oxygen reach the metal layer? Is it from the residual gas in the annealing chamber, or does it come from the adjacent dielectric oxide layer?
- What is the highest temperature and maximum pressure at which the

metamaterial is thermally stable? Is there a technologically suitable working range for a wide application of thin-film metamaterials?

- Can we find suitable combinations of materials that produce a metamaterial which can be used to validate long-term durability at high temperatures?

1.2 Outline of the thesis

Chapter 2 explains all the experimental procedures used to fabricate and characterize single layers, bilayers, 3-layer-systems, and multilayered metamaterials. The section starts with the possibility and conditions for thin-film preparation using magnetron sputtering, followed by thin-film characterization techniques like x-ray diffraction (XRD) which also includes a detailed temperature validation procedure for in-situ measurements using strip heaters, x-ray reflectivity (XRR), surface profilometer, Fourier transformation infrared spectroscopy (FTIR), and electron microscopy.

In chapter 3, the first part shows thin film properties of as-prepared W and HfO_2 layers, and annealing results from W/HfO_2 based metamaterials at different temperatures and vacuum pressure. The second part presents results from annealing W/HfO_2 metamaterial in an inert gas atmosphere. The last part focuses on the degradation mechanism of W in a 3-layer-system, morphological changes in the HfO_2 layers and analysis of W oxidation at high temperatures is discussed.

Chapter 4 shows the thin film properties of as-prepared Ir layers and later thermal stability of Ir is validated. In-situ annealing results from 3-layer-systems are initially presented to understand degradation mechanism in Ir layers, and later ex-situ annealing results on a Ir/HfO_2 3-layer-system at different temperatures and time are presented to check the oxidation resistance as a function of pressure. Finally, the durability of a Ir/HfO_2 metamaterial in comparison to a W/HfO_2 metamaterial is presented to validate long-term stability of selective emitters.

Chapter 5 summarizes the main findings of the current work and proposes suggestions for further research work.

The work presented here is funded by German research foundation (DFG) via **SFB 986** 'Tailor-Made Multi-Scale Material Systems: M3', **Project-ID 192346071**. All experimental results shown in this thesis were carried out at Helmholtz Zentrum Hereon and Hamburg University of Technology (TUHH). Besides my mentor Michael Störmer, esteemed colleagues Alexander Yu Petrov, Manohar Chirumamilla, Surya Snata Rout, Tobias Krekeler, Martin Ritter, Kaline P. Furlan and Prof. Manfred Eich from TUHH, Hans-Werner Becker from Ruhr-Universität Bochum, Ragle Raudsepp and Mauricio Schieda from Helmholtz-Zentrum Hereon, contributed to the work. Results from this thesis have already been published and the content of this thesis is copied from our current publications [41], [57], [58] and its supplemental information. As these publications are a part of the current work, citations from these papers will not be made visible via quotation marks.

Chapter 2

Experiments

2.1 Thin film Preparation

All the metal and dielectric coatings used to fabricate the metamaterial selective emitters were prepared by magnetron sputtering [59], [60]. The in-house designed sputtering facility and it's schematic is shown in Figure 2.1 A and B, is located in the sputtering lab present at Helmholtz-Zentrum Hereon. The sputtering facility with a diameter 60 cm is equipped with a load lock and can accommodate up to three sputtering targets. The schematic Figure 2.1 B, at the right shows the arrangement of the sputtering targets, the shutter between them, and the sample holder.

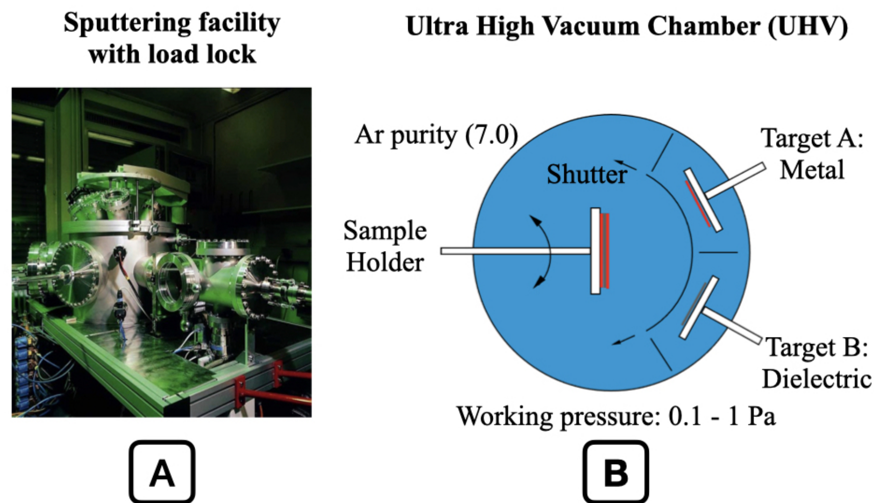

Figure 2.1: (A) Sputtering facility at Hereon. (B) Schematic of the sputtering chamber.

The distance between the targets and the sample holder is 14 cm. Metal films (W and Ir) are prepared by Direct Current (DC) sputtering, while the dielectric film (HfO_2) is prepared by Radio Frequency (RF) sputtering. The sample holder is custom-made along with cooling and heating facilities, and is rotated at 1 Hz to get a homogeneous coating on a substrate. All the sputtering targets are 3" in diameter and were procured from Sindlhauser Materials GmbH. The W and Ir sputtering targets have a purity of 99.95%, and two HfO_2 targets have a purity of 99.95% ($<$ 4000 ppm Zr impurity) and 99.98% ($<$ 2000 ppm Zr impurity). The sputtering chamber is evacuated to a base pressure below 1×10^{-7} mbar. During the sputtering process, Ar gas of purity 99.99999% was used, and the working pressure was maintained at 2×10^{-3} mbar. The validation of the individual deposition rate of W,

Ir, and HfO_2 was done separately by deposition of single layers on silicon substrates 20 mm × 60 mm × 0.7 mm having a (100) orientation parallel to the substrate normal. The bilayers, 3-layer-system, and metamaterial selective emitter used for annealing experiments were coated on sapphire substrates 10 mm × 10 mm × 0.5 mm having a (1-102) orientation and thermal expansion coefficients of 5.3×10^{-6} K^{-1} (parallel to c-axis) and 4.5×10^{-6} K^{-1} (perpendicular to c-axis). The thin film preparation of W and Ir were done using a DC sputtering power of 120 W and 100 W, which yielded a deposition rate of 0.07 nm s^{-1} and 0.12 nm s^{-1}, respectively. HfO_2 films were prepared using a RF sputtering power of 400 W and which had a deposition rate of 0.23 nm s^{-1}. However, a slight reduction is observed over time, due to usage, e.g. the same W target in it's initial experimental run had a sputtering rate of 0.08 nm s^{-1}

2.2 Annealing experiments

In order to validate the thermal stability of the prepared thin films, annealing experiments were performed from 25 °C up to 1800 °C and at different pressure range between 2×10^{-6} mbar - 1 bar. The annealing experiments are broadly divided into ex-situ and in-situ annealing. Different furnace and pumps were used to achieve a particular experimental condition. The details of the furnace and pumps are shown in the Table 2.1.

S.No.	Type	Furnace	Max.Temp. / °C	Pressure / mbar	Pump
1	Ex-situ	Linkam TS 1500	1400	2×10^{-2}	Diaphragm
2	Ex-situ	Linkam TS 1500	1400	2×10^{-3}	Rotary vane
3	Ex-situ	Linkam TS 1500	1400	2×10^{-5}	Turbo
4	Ex-situ	RD-G WEBB	1500	2×10^{-6}	Turbo
5	Ex-situ	HTF 1700	1700	1000	-
6	In-situ	HTK 2000N	2000	2×10^{-6}	Turbo

Table 2.1: Equipment details used for annealing experiments.

2.3 Characterization Methods

2.3.1 X-Ray diffraction (XRD)

X-rays were discovered by the German physicist Conrad Wilhelm Röntgen in the year 1895 at Würzburg [61]. X-rays are electromagnetic waves having energies ranging from 200 eV to 1 MeV and wavelengths (10 nm to 1 pm) in the region between ultraviolet rays and gamma rays. Later in the year 1912, the first x-ray diffraction experiment was performed on a crystalline sample by Max von Laue [62]. X-ray diffraction is a powerful non-destructive technique to investigate the structure of materials at the atomic level.

Diffraction is a phenomenon that explains the change of lightwave behavior when they react with an object. When an x-ray beam is incident on an individual atom, the electrons in the atom oscillate about their mean position. A series of events occur during the interaction of incoming x-rays and

the electrons in the atom. Scattering is referred to as a process of absorption and re-emission of electromagnetic radiation.

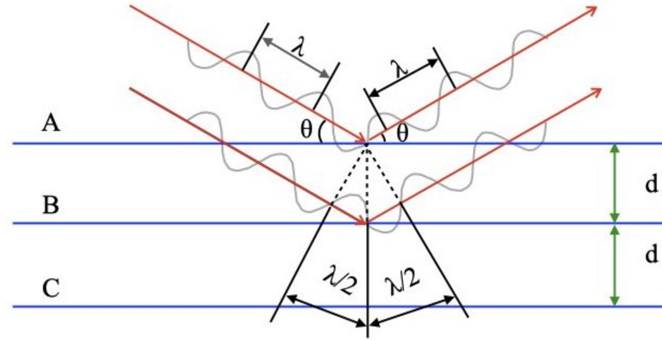

Figure 2.2: Bragg condition required for diffraction of X-rays.

A crystalline material contains long-range order of periodically arranged atoms. When x-rays are directed towards a crystalline material, the electrons in all the atoms coherently scatter the incoming x-rays. If the scattered waves are in phase, constructive interference of the scattered waves occurs in specific directions resulting in the formation of a diffraction pattern [63],[64]. Therefore, the obtained diffraction peaks provide us information about the internal atomic arrangement of matter. The condition for diffraction to occur is governed by Bragg's law (Figure 2.2),

$$2\,d\,\mathrm{Sin}\,\theta = n\,\lambda \tag{2.1}$$

where,

d = interplanar distance

θ = angle measured from the reflecting planes

n = integer multiple called the order of reflection

λ = wavelength of incident radiation

The law states that the intensity of the diffracted beam would be maximum at a certain angle when the path difference between the two reflected waves from different planes is an integral multiple of the wavelength of incident radiation. The diffraction pattern obtained is characteristic for each material and contains information about the atomic arrangement of matter. Once the Bragg angle 2θ is determined along with a known wavelength λ, the interplanar spacing d can be calculated, and when this is used for some Bragg peaks, the unit cell geometry can be determined.

All the diffractograms were measured in a Bruker D8 Advance diffractometer equipped with an Anton Paar - HTK 2000 N heating stage and a state-of-the-art position-sensitive Lynxeye XE-T detector having a resolution of 380 eV. The diffractometer source was operated at 40 kV and 40 mA. The first step in the process of measuring the coupled θ-2θ scan is to identify the peak position of the substrate 25.57° (012) sapphire and 69.13° (004) in the case of the silicon. A short scan from 24°- 27°(sapphire) is performed with an increment of 0.2° and a time of 0.1 s per step. The single crystalline peaks from the substrate dominate the diffraction pattern. In order to prevent the substrate peaks in the typical diffractograms, the long coupled θ-2θ scans are measured with an offset of -2°. In the case of in-situ annealing experiments, a temperature validation is performed prior to the actual ex-

periment, explained in Appendix A. Before annealing, the heating chamber was evacuated to a pressure less than 3×10^{-6} mbar. The heating stage can be adjusted in the z-direction and therefore the height of the z-stage was precisely adjusted to match peak positions of the sapphire substrate with Powder Diffraction File (PDF 01-082-1467) as the reference in order to minimize the height error. The height error can be an important source of error in the measured diffraction angles, hence the geometry of diffraction requires that the specimen should lie on the focusing circle and the center of the goniometer. If the sample is higher than the goniometer center, the detected 2θ will be positive, on the other hand if the sample is lower than the goniometer center, the detected 2θ will be negative. Typical diffractograms are recorded for example, from 20° to 90°, with an increment of 0.02° and a time step of 0.1 s per step, using Cu K_{α_1} radiation (λ = 0.15406 nm) as shown in the inset Figure 2.3. During analysis of the diffraction patterns, position, width, and integrated intensity (net area) of the diffraction peaks were determined to evaluate interplanar spacing, grain size, and volume fraction of a distinct phase. Grain size t in the out-of-plane direction is calculated using the Scherrer equation [63].

$$t = \frac{K\,\lambda}{B\ \mathrm{Cos}\ \theta_B} \tag{2.2}$$

Where,

t = is the grain size in nm

K = is a dimensionless shape factor (K = 0.9 for spherical particles with cubic symmetry) also known as Scherrer constant [65]. The value of K depends on definition of breadth, crystalline shape and the crystallite-size distribution.

λ = wavelength of x-rays (λ = 0.15406) in nm.

B = is the full width at half the maximum of the peak (FWHM) in radians.

θ_B = is the glancing angle, which is half of the Bragg angle

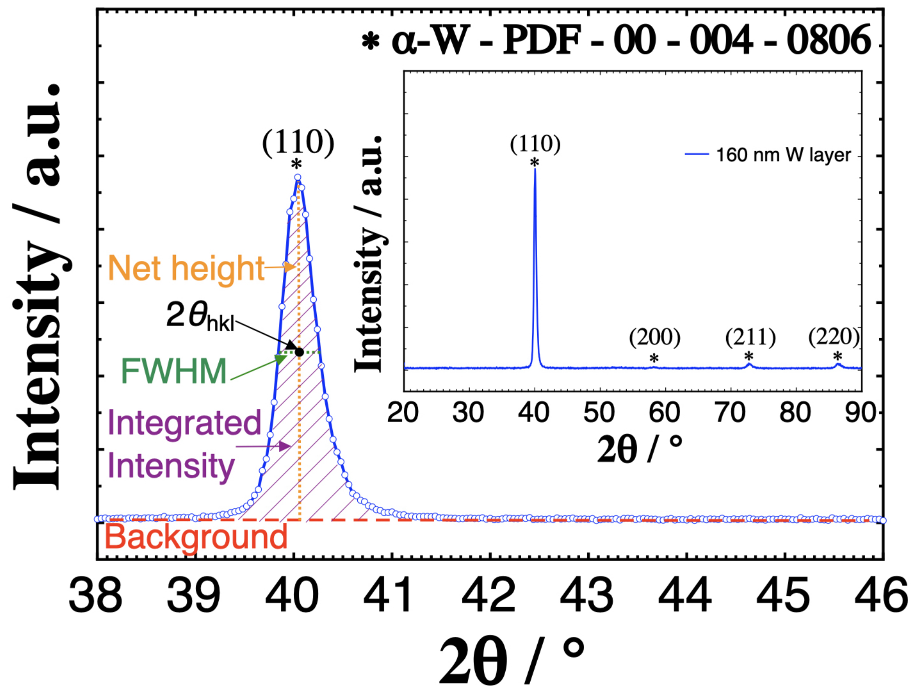

Figure 2.3: Important peak parameter in x-ray diffraction. Inset showing the longer range and all indexed peaks of a 160 nm thick W layer.

The interplanar spacing d_{hkl} is determined from the measured peak po-

sition $2\theta_{hkl}$ in the diffraction patterns using Bragg's condition, which results in the following equation:

$$d_{hkl} = \frac{\lambda}{2\,\mathrm{Sin}\,\theta_{\mathrm{hkl}}} \tag{2.3}$$

Additional information can be obtained from the diffraction peak in a diffractogram. The integrated intensity [66] of the diffraction peak represents the volume fraction of a phase is determined by the following equation,

$$I = \left(\frac{I_0 A \lambda^3}{32\pi r}\right) \times \left(\left(\frac{\mu_0}{4\pi}\right)^2 \frac{e^4}{m^2}\right) \frac{1}{v^2} \left(F^2 p \left(\frac{1 + \mathrm{Cos}^2\, 2\theta}{\mathrm{Sin}^2\,\theta\,\mathrm{Cos}\,\theta}\right)\right) \frac{e^{-2M}}{2\mu} \tag{2.4}$$

Where,

I = Integrated intensity of the diffraction peak

i_0 = Incident beam intensity

A = Incident beam cross section area

r = radius of the diffractometer circle

μ_0 = constant $4\pi \times 10^{-7}$ m kg C^{-2}

e = electron charge

m = electron mass

v = unit cell volume

F = structure factor

p = multiplicity factor

e^{-2M} = temperature factor

μ = linear absorption coefficient

The integrated intensity is a useful parameter to determine the volume fraction of phases in a material and gives us an insight about the kinetic reactions like oxidation of the metal in a selective emitter, which is explained in detail in section 3.4.

Temperature validation

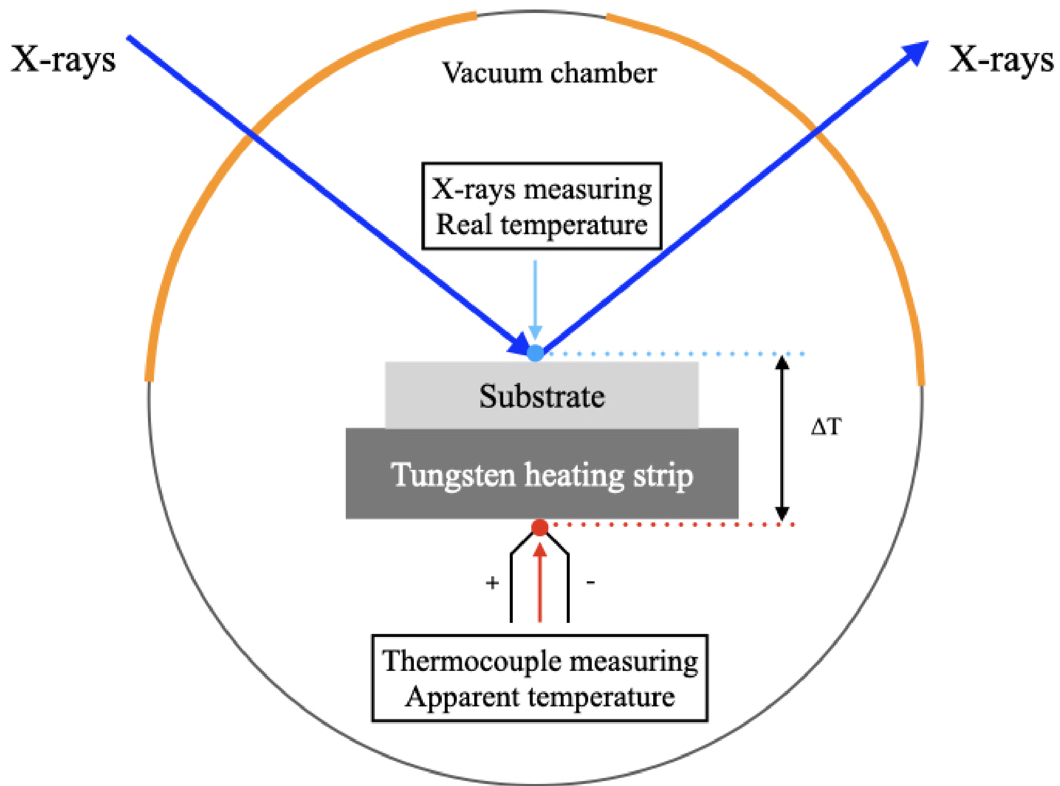

Figure 2.4: Cross section of an in-situ annealing chamber.

The fundamentals for x-ray diffraction were addressed in the start of section 2.2.1. However, most of the x-ray measurements are measured in ambient temperature and pressure conditions. In-situ XRD is an indispensable technique that allows us to understand material behavior at non-ambient conditions like variations in pressure, temperature, gas environment, electric field, magnetic field, and mechanical load [67], [68].

This characterization method is vital for understanding the thermal expansion, phase transformations and microstructural changes that occur at high temperatures in the thin films used in this study. A typical schematic of a high-temperature chamber (HTK 2000N) is shown in Figure 2.4. All in-situ measurements were done at a high vacuum pressure below 3×10^{-6} mbar. The sample to be investigated is directly placed on a W-strip heater, which works on the resistance heating principle. It is possible to reach a maximum temperature of 2000 °C using heating rates up to 900 °C min^{-1}.

The accuracy of the measured temperature has to be taken into consideration, as the temperature displayed in the controller is the temperature of the heating strip. The thermocouple W/Re is spot welded below the heating strip. Therefore, a temperature gradient exists between the spot weld and the top surface of the substrate (i.e. the thin film on the substrate) under investigation. Compared to environmental heaters, the temperature deviation is higher for strip heaters. The thermal properties of the sample, like heat conductivity, emissivity, sample thickness, and good contact between the sample and the heating strip, have a significant effect on the temperature

deviation.

There are two methods for temperature validation used in non-ambient XRD:

- Validation using phase transition
- Validation using thermal lattice expansion of materials with a well known thermal expansion of coefficient.

In the first method, temperature validation is done using phase transition. By definition, phase transition refers to change between different states of matter, solid, liquid, and gas. In addition, phase transition in non-ambient XRD uses materials with a known crystallographic transition (solid-solid), a reversible phase transition, and a known melting point, e.g., Indium 156.6 °C, Tin 231.9 °C, etc. The disadvantage of this method is that a single material has only a limited number of phase transitions. Numerous measurements from different materials should be performed to validate temperature for a given range of interest.

The second method, validation by thermal lattice expansion [69], [70], is used in this work to validate the temperature at the film surface. Thermal expansion is the tendency of the material to change shape, area, or volume due to an increase in kinetic energy of atoms and molecules inside a material in response to temperature change. The common perception is that materials expand on heating because atoms in a solid vibrate and have a higher amplitude of vibrations at a higher temperature. This fact alone is not enough

for thermal expansion. If the mean position of the vibration of atoms does not change, there will not be any thermal expansion no matter how high the amplitude of the atoms vibrates.

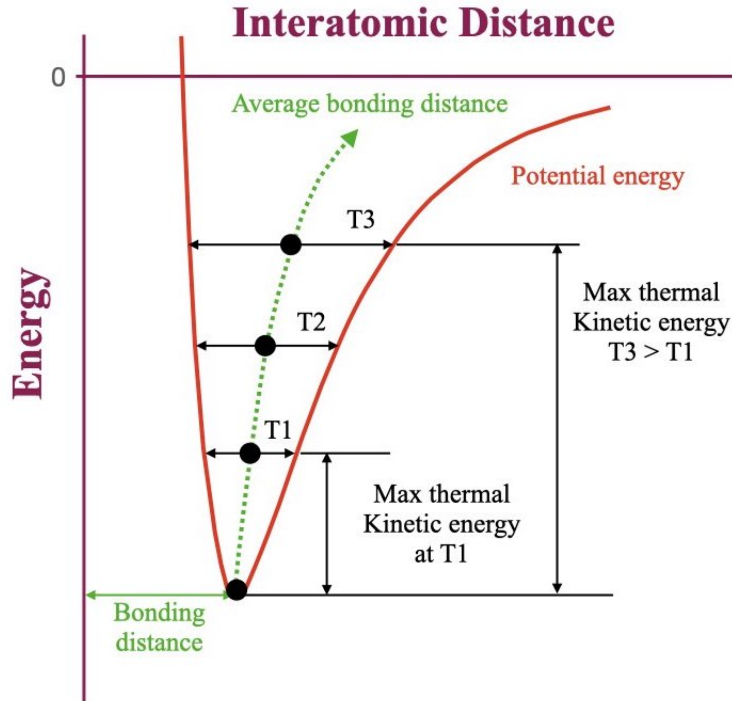

Figure 2.5: Total potential energy for interaction of pair of atoms as a function of interatomic distance.

This can be explained with the help of a potential well diagram in Figure 2.5. The minimum of the potential well has an asymmetrical shape with respect to the position of the energy minimum and has an interesting consequence. The distance between the potential energy minimum and the y-axis represents the bonding length between the atoms at 0 K. As the temperature is increased to T1, the atoms vibrate around their mean position with

increased amplitude, and an increase in bonding distance is observed. On increasing the temperature to T2 and T3, the interatomic distance increases further. This is a direct consequence of the asymmetry of the potential well. Hence it is straightforward that the average interatomic distance increases with temperature and results in the thermal expansion at higher temperatures. The increase in interatomic distance can be measured using x-ray diffraction mentioned in equation 2.5. The thermal expansion can be expressed using the following equation [71].

$$\frac{\Delta L}{L_0}(\%) = \frac{L - L_{293}}{L_{293}} \times 100 = a_0 + a_1 \times (T - T_R) + a_2 \times (T - T_R)^2 + a_2 \times (T - T_R)^3 \tag{2.5}$$

Where,

L = length at temperature T

T = temperature in K

L_{293} = length at 293 K

T_R = reference temperature in K

a_0, a_1, a_2, a_3= coefficient of thermal expansion

The lattice parameters are calculated by performing a full pattern fit using Rietveld refinement (TOPAS) [72], and from the lattice parameter, the actual temperature at the sample surface can be validated. Temperature validation of three materials has been performed in this work, a direct measurement of lattice parameters of the W heating strip used, MgO sub-

strates, and sapphire substrates (Appendix A). The goal is to obtain a plot of apparent temperature vs. actual temperature at the sample surface.

2.3.2 X-Ray reflectivity (XRR)

The thickness, roughness, and density of W, Ir and HfO_2 films under 100 nm were measured using X-ray reflectometry (XRR). In this technique, x-ray beam is incident at grazing angles towards the film and the reflected intensity is monitored. The reflection at the surface of the film, interface between the film and substrate causes interference. Oscillations called Kiessig fringes are formed in the reflected profile as a result of interference. The distance between consecutive fringes helps in determining the thickness of the film. The reflection analysis is based on Frensel reflection theory[73], [74]. The refractive index n of x-rays for normal materials is slightly less than 1. The refractive index n is usually expressed in complex form:

$$n = 1 - \delta + i\beta \tag{2.6}$$

Where the parameter δ considers the dispersion part and β the absorption part. These parameters are related to the linear absorption coefficient μ and the electron density ρ_e of the investigated material via :

$$\delta = \frac{2\pi}{k^2}\rho_e r_0 \tag{2.7}$$

$$\beta = \frac{\mu}{2k} \tag{2.8}$$

Where, $k = \frac{2\pi}{\lambda}$ is the wave vector of the incoming wave with the wavelength λ and r_0 the classical electron radius. When the incident angle equals to or less the critical angle θ_c, total external reflection occurs. Thus, the density of the film can be obtained using the critical angle. The critical angle for total external reflection is given by:

$$\theta_c = \sqrt{2\delta} \tag{2.9}$$

All measurements were performed in a Bruker D8 Advance equipped with a reflectometry stage, a knife-edge, and Göbel mirror [75] behind the source to shape parallel beams and monochromatize x-rays using Cu-K_{α_1} radiation (λ = 0.15406 nm). The distance between the knife edge and the sample surface is adjusted to about 9 μm and sometimes lifted off for longer scans. XRR scans were usually recorded between 0° and 6°, with an increment of 0.01° and a time of 10 s per step. Layer properties such as thickness, roughness and density were investigated using LEPTOS R software from Bruker.

2.3.3 Fourier Transform Infrared Spectroscopy (FTIR)

In infrared (IR) spectroscopy, IR radiation is made to pass through a sample. As a result, part of the radiation is transmitted through the sample, while the other part is absorbed. This results in a spectrum representing the

fingerprint of the sample containing absorption peaks which correspond to the frequencies of vibration between the bonds of the atoms in a material.

Reflectivity spectra of the multi-layered metamaterial were measured using a FTIR spectrometer in the wavelength range of 1 to 10 μm. An FTIR microscope (Bruker Hyperion 2000) coupled to an FTIR spectrometer (Bruker Vertex 70) is used to measure the reflectivity, where a Schwarzschild objective with a magnification of 15 times is used to collect light. The objective operates at $\sim 16^{\circ}$ off-normal to the substrate surface and has a collection cone apex angle of $\pm 7^{\circ}$ and an Au mirror is used for normalization.

2.3.4 Surface Profilometer

Topological information like surface morphology, step height and surface roughness can be extracted using a profilometer. In principle profilometry can be broadly classified into contact free optical profilometer and contacting stylus profilometer. In this thesis, a stylus profilometer is used to determine the step height of the prepared films. In a stylus profilometer, a stylus physically moves along the surface and traces the profile in order to acquire the step height. A mechanical force is applied to the stylus with a feedback loop that monitors the force from the sample pushing up against the stylus as it scans along the surface.

Single layer [76] of W and Ir having a thickness above 100 nm and HfO_2 films with thickness above 200 nm were measured using a Dektak XT surface profilometer. Initially during film preparation, part of the substrate was

covered with kapton tape, and the coating was done over it. After the coating was completed the kapton tape was removed, leaving behind a step between the film and the substrate. The measured step height gives the thickness of the film sputtered. The scan length was 3000 μm, and duration of each scan was 10 - 30 s. The force applied on the stylus was 3 mg. Each sample was scanned three times at different points, and the average value was used to estimate the film thickness.

2.3.5 Electron Microscopy

In transmission electron microscopy (TEM), a high energy electron beam is made to pass through a very thin sample. The interaction between the electron beam and the atom in the sample can be used to characterize crystal structure, dislocations, grain boundaries and perform chemical analysis. In this thesis, TEM analysis is performed on thin films to study chemical composition for instance oxidation of the metal, understand the defect mechanism and observe if any inter-layer diffusion or reaction occurs between the layers in the selective emitters.

The cross-sectional TEM samples, and cross-sections for scanning electron microscopy (SEM) imaging were prepared with a FEI Helios G3 UC focused ion beam scanning electron microscope (FIB-SEM). Both the cross-sectional TEM lamellae and cross-sections were prepared using 30 keV Ga+ ion beam and different beam currents (9 nA to 40 pA). Secondary electron (SE) images of the cross-sections were taken under low keV (2 keV) electron beam and

high-resolution immersion mode using a through lens detector (TLD). To prevent charging during the FIB-SEM study, the sample was coated with a thin layer of carbon using a carbon thread evaporator. A FEI Talos F200X TEM equipped with a four-quadrant silicon drift detector system for energy dispersive x-ray spectroscopy (Super-X(FEI)) system was used for taking high angle annular dark field (HAADF) images and to perform EDS analysis. Spectrum images (SI) were acquired using a 1 nA beam current and dwell time of 10 μs per pixel. Resolution was 512 $\times$ 512 pixels with a pixel size of 766 pm. To get a better signal-to-noise ratio, integrated intensities of over 1000 drift corrected SI were used.

Chapter 3

Tungsten - Hafnia selective emitter

3.1 Properties and morphology of tungsten thin films

An ideal selective emitter should have good thermal stability and sustain working temperatures above 900 °C for TPV applications that use a low bandgap PV cell whose cutoff wavelength lie in the near infrared wavelength Figure 1.4. Refractory materials are the suitable choice, as they have high melting points and recrystallization temperatures above the operating range of the TPV systems. W has the second-highest melting point of 3410 °C next to carbon (C) and the lowest vapor pressure 8.15×10^{-10} mbar at 2000 °C among metals [77]. It is essential for the material to have a low vapor

pressure to prevent direct sublimation of the material from the solid phase into the gaseous phase. The optical properties of W have been extensively researched and serve as a suitable candidate for TPV applications. The spectral emissivity ϵ_λ of W has a maximum in the wavelength range of 0.3 - 0.5 μm. The following empirical equation (3.1) can represent the experimental results of total emissivity e_t in the temperature range between 400 to 3600 K [78]:

$$e_t = (-2.6875 \times 10^{-4}) + (1.819696 \times 10^{-4})T - (2.1946163 \times 10^{-8})T^2 \quad (3.1)$$

3.1.1 Polymorphs of tungsten thin films

In this work, a metamaterial selective emitter containing alternative layers of W and HfO_2 films is heat-treated above 1000 °C to validate the thermal stability. Therefore, it is required to prepare the W films in their thermodynamically stable phase. W can exist in three different phases: α-phase, β-phase, and γ-phase. The phase obtained in the film depends on the sputtering conditions like sputtering power, Ar pressure, deposition rate, presence of residual oxygen in the chamber, the distance between the sputtering target and substrate coated. The α-phase is thermodynamically the most stable phase having bcc (A2) structure with lattice parameters values of $a = 0.3165$ nm. There is extensive literature [79], [80], [56], [81], [82], [83] available on the different sputtering conditions to be satisfied to grow W films with α-phase.

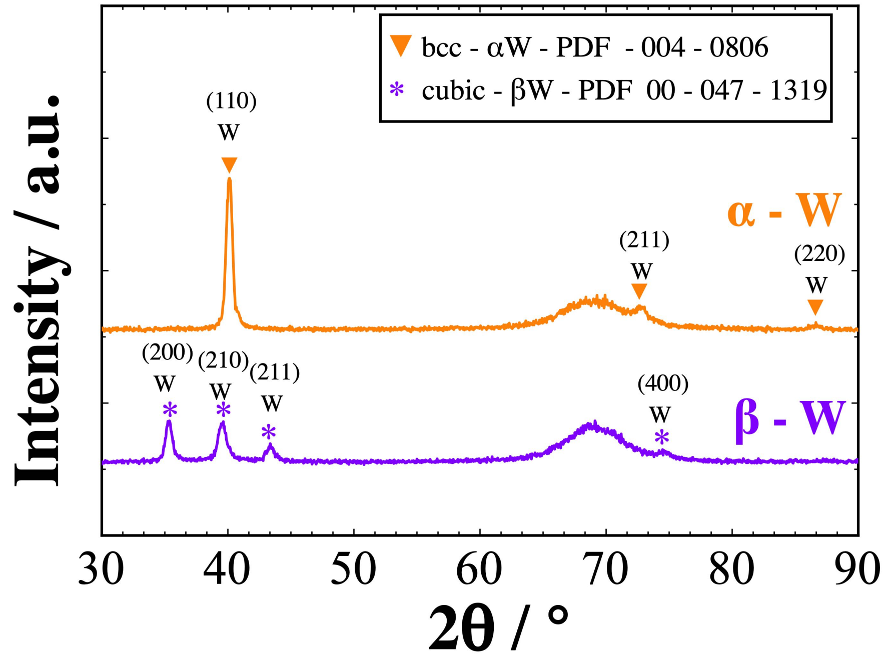

Figure 3.1: X-ray diffractograms showing α and β phase of two separate 20 nm W films. All scans are background normalized.

Figure. 3.1 shows the two diffractograms of 20 nm thick W film coated on silicon substrates. In both cases, argon pressure was maintained constant at 0.2 Pa throughout the sputtering process, and before coating the base pressure of the chamber was held at a pressure less than 2×10^{-7} mbar. The diffractogram in orange (Figure 3.1) represents the α-phase of 20 nm thick film of W. The peak (110) at 40.1°, (211) at 72.7°, and (220) at 86.6° match with the α-phase of W in the powder diffraction file [84] (PDF 00 - 004 - 0806). In this case, the sputtering power was set to 120 W, and had a deposition rate of 0.093 nm s^{-1}. The XRR plot in orange (Figure

3.2) represents the α-phase of the 20 nm W film with well-defined Kiessig fringes and no attenuation in the measured range, indicating smooth films with uniform thickness compared to β-phase. The critical angle θ_c shift to a higher angle and reveal that the α W films have a higher density.

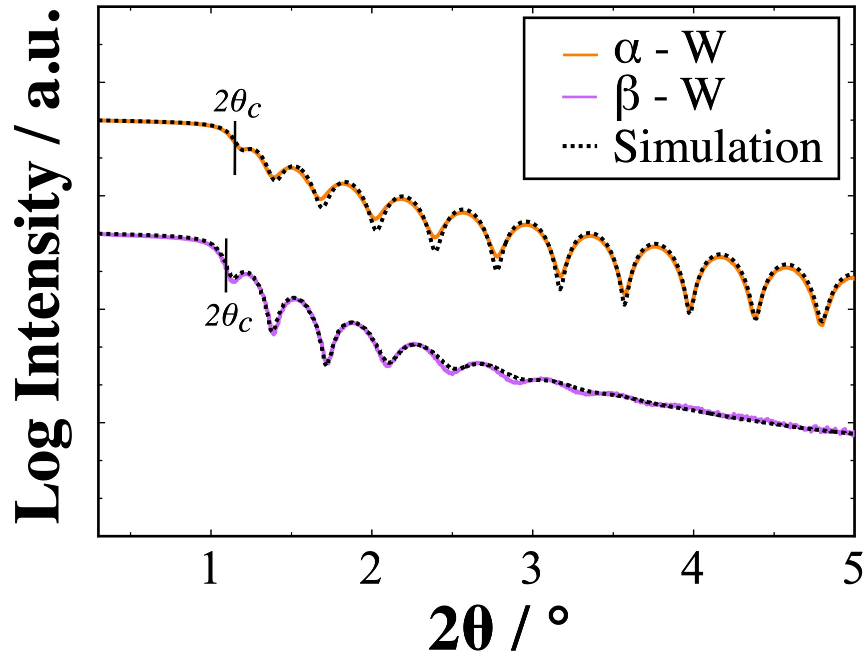

Figure 3.2: X-ray reflectivity measured and simulated scans of two 20 nm containing α and β W.

When the sputtering conditions are altered a bit, one may end obtaining the β phase having an A15 structure and a higher lattice parameter value of $a = 0.4150$ nm. The β phase is not preferred for high temperature application because above 635 °C which is 0.2 T_m (melting point), the β-W transforms into the stable α-phase and this phase transformation is irreversible. In

comparison to as-prepared α-W films, the films that are transformed from β-phase to α-phase have a higher roughness [83] and change in film density as the growth conditions are not similar. The transformation of β to α-phase requires an activation energy of 0.6 – 0.7 eV to 1.14 eV [85]. The diffractogram in violet Figure (3.1) shows 4 prominent peaks (200) at 35.3°,(210) at 39.6°,(211) at 43.4°, and the higher-order peak (400) at 74.7°, that match the β -phase of W (PDF 00 -047 -1319). In the case of β -phase W films, the sputtering power was 80 W, yielded a sputtering rate of 0.064 nm s^{-1}. At low sputtering power, the atoms arriving at the substrate do not have enough kinetic energy, which reduces surface mobility at the surface. As a result, the resultant film grown is not so dense and has a higher surface roughness. The simulated values are shown in Table 3.1. Figure 3.2 shows the XRR plot in violet of a 20 nm W film with the β -phase. There is a reduction in the number of Kiessig fringes due to the attenuation, indicating higher roughness of the film. The shift in the critical angle θ_c to the left shows the sputtered β-W films have a lesser density. The other factor influencing the β -phase was an increased distance of 20 cm between the sputtering target and the substrate. As the distance increases, the mean free path of the atoms arriving from the target to the substrate increases, therefore the number of collision between the gas atoms present in the chamber and the atoms that are to be deposited increases, thereby reducing the kinetic energy of the arriving atoms at the surface. Due to the latter effect mobility and the deposition rate is reduced favoring formation of β -phase. The presence of oxygen impurities in the

chamber also favors the growth of the β -phase [86].

Phase	Aim / nm	Thickness / nm	Roughness / nm	Density / g cm^{-3}
α W	20	20.4 (0.5)	0.43	18.8
β W	20	19.7 (0.5)	1.31	16.8

Table 3.1: Simulated XRR thickness and roughness of 20 nm W films. The experimental error of thickness determination is ± 0.5 nm.

The third phase of W is γ-phase, a metastable phase having a face-centered cubic (A1) structure, a lattice parameter value of a = 0.4150 nm [87], and a density of 15.8 g cm^{-3} [77]. The γ-phase is observed only in the case of thin films grown on rock salt (NaCl), glass, and mica by sputtering process [88] and depends on the deposition conditions and temperature range between 200 °C and 500 °C [89].

3.1.2 Structure and microstructure of tungsten thin films based on film thickness

Structure and grain size evolution in thin films plays a vital role in high-temperature applications. Figure 3.3 A and B, shows an x-ray diffractogram of various single layers of W having different thicknesses 5 nm, 10 nm, 20 nm, 40 nm, 80 nm, and 160 nm. Figure 3.3 A contains diffractograms of tungsten films having thickness 5 nm, 10 nm and 20 nm, normalized to the peak maximum. The diffractogram in pink represents the scan from the uncoated sapphire substrate. The expected (110) peak at 40° from the α-phase of W is not visible for the 5 nm film. However, the peak (110) at 40°,

(200) at 58°, and (211) at 72° are visible for the 10 nm film with almost the same intensity.

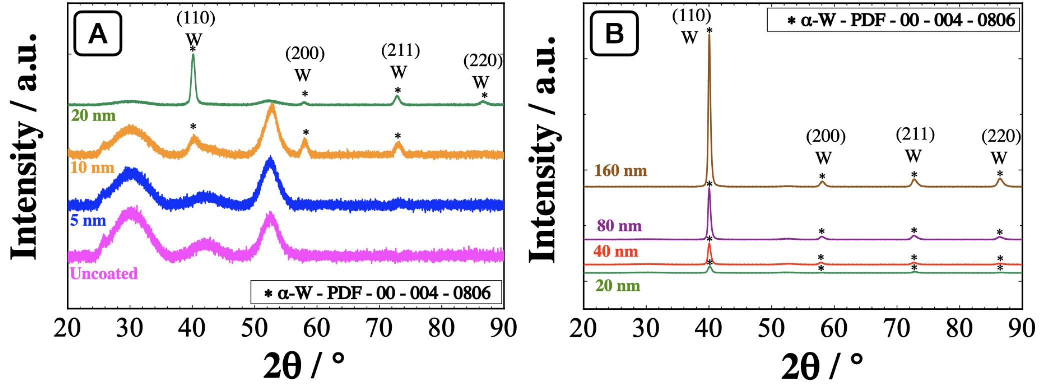

Figure 3.3: (A) X-ray diffractograms of tungsten thin films with thickness 5 nm, 10 nm and 20 nm, normalized to the peak maximum. Diffractogram in pink is the scan of the uncoated sapphire substrate. (B) X-ray diffractograms of tungsten thin films with thickness 20 nm, 40 nm, 80 nm and 160 nm, normalized to the background. For reference purpose diffractogram of the 20 nm tungsten film is added in both of the plots.

The diffractogram in green of the 20 nm thick film is shown in both Figure 3.3 A and B for reference purpose. Figure 3.3 B contains diffractograms of tungsten films having thickness 20 nm, 40 nm, 80 nm and 160 nm, normalized to the background. As the thickness of the film increases, e.g. 160 nm film, the (110) reflection is strong. For all other reflections such as (200) and (211), as the film thickness increases, the increase in intensity ratio is reduced in comparison to the (110) peak. Also the peaks get narrower, indicating bigger grain size calculated using the Scherrer formula shown in equation 2.2 . The grain sizes in the growth direction are 3 nm, 7 nm, 15 nm, 18 nm, 20 nm,

and 22 nm for 5 nm, 10 nm, 20 nm, 40 nm, 80 nm, and 160 nm thick W layers respectively after sputtering with no further thermal treatment.

3.1.3 Structure and microstructure of tungsten thin films based on Ar gas pressure

Based on the Ar pressure used during magnetron sputtering, (Figure 3.4) thin films can either be in a state of tensile or compressive stress [90], [91], [92], [92]. The compressive stress in the film arises due to the bombardment of energetic species having energies in the range of 2 - 10 eV and hence termed atomic peening [59], [93], [94].

Since the atoms arriving at the film surface have higher energy, it is possible to force atoms into tiny spots between the existing adatoms at ambient thermal conditions, resulting in the formation of dense films. The energy of the arriving atoms can be altered by changing the pressure of the sputtering gas used. Figure 3.5 shows the d-spacing of a 20 nm W film as a function of argon pressure. At low pressure 2×10^{-3}mbar, the film has a higher d-value of 0.2243 nm, and by increasing the pressure to 1×10^{-2} mbar, the d-value lands at 0.2234 nm. As the pressure in the sputtering chamber increases, the mean free path (minimum distance between two collisions) of the arriving W atoms is reduced. The increase in collisions reduces the kinetic energy of the arriving atoms and minimizes the compressive stress formed during sputtering.

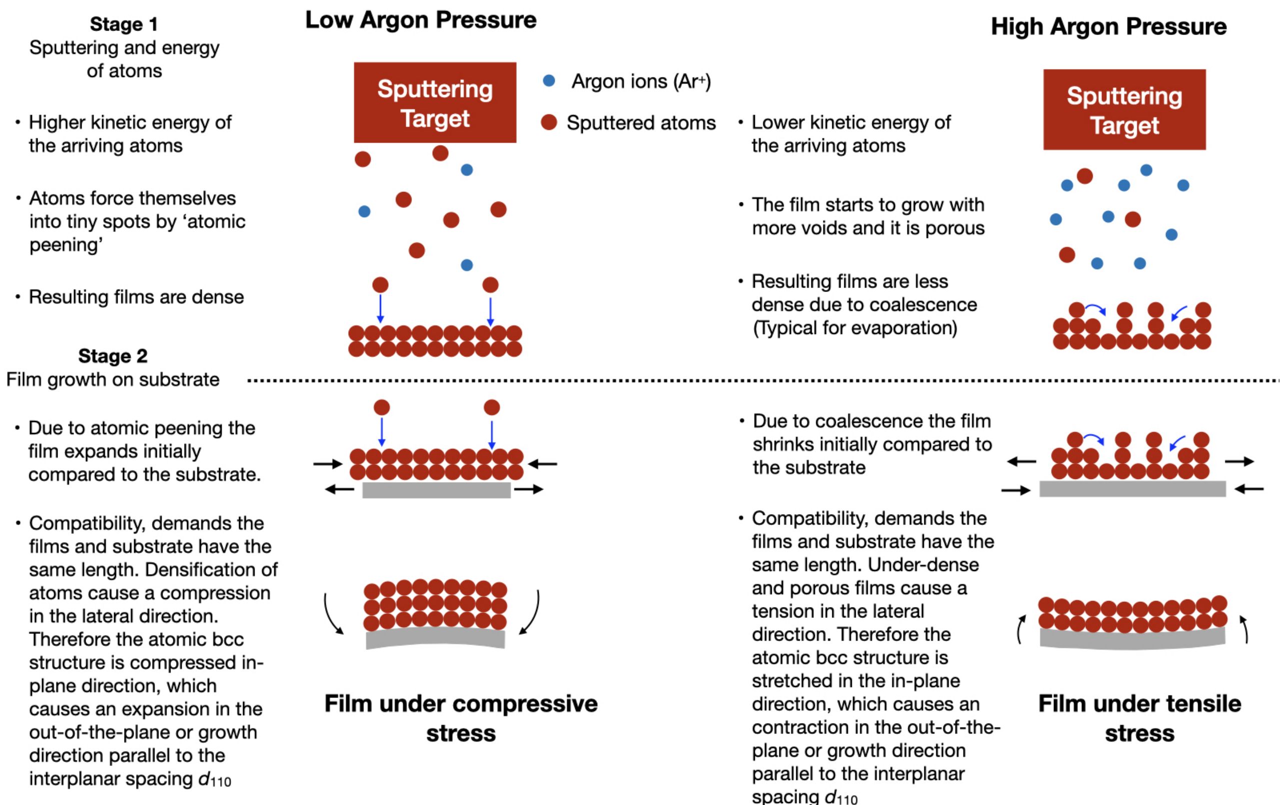

Figure 3.4: Schematic explaining the effect of sputtering gas on the morphology of the film growth during sputtering. (A) At lower sputtering pressure, there are less gas atoms, therefore the mean free path is higher (lesser collisions) resulting in higher kinetic energy of the arriving atoms. The films grown under such conditions are more densified having a higher d-value ($d_c > d_{bulk}$) and the films are under compressive stress.(B) At higher sputtering pressure, there are more gas atoms, therefore the mean free path is lesser (more collisions) resulting in lower kinetic energy of the arriving atoms. The films grown under such conditions are less densified having a lower d-value ($d_t < d_{bulk}$) and the films are under tensile stress.

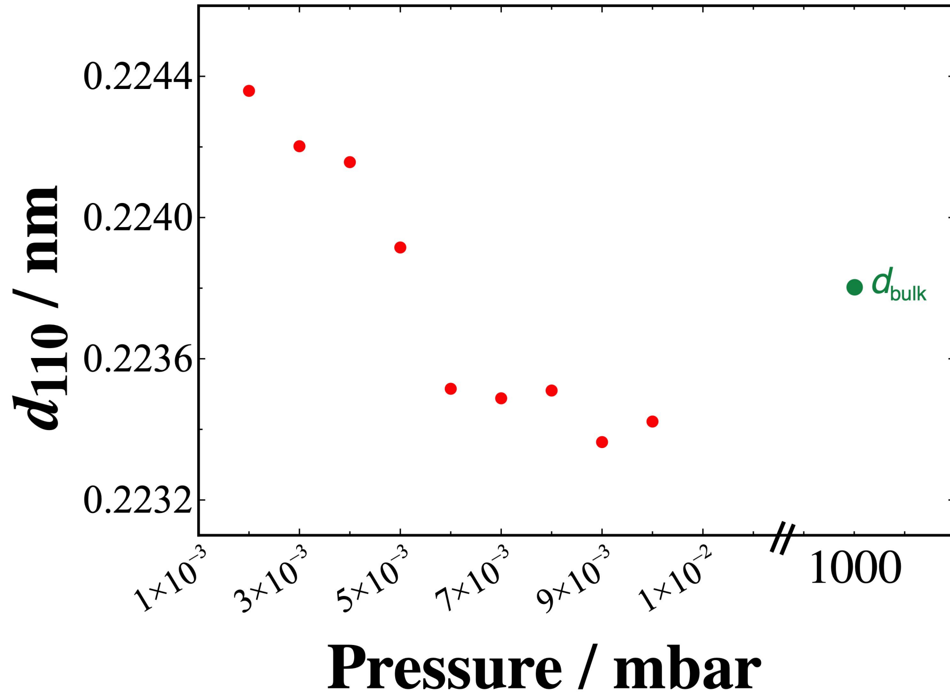

Figure 3.5: d-spacing versus Ar pressure in a 20 nm W layer. The data point shown in green is the bulk value of W at ambient pressure.

3.2 Hafnia - layer thickness, structure and phase formation

HfO_2 exists in three phases, which are monoclinic, tetragonal, and cubic phase [44], [95] and has a melting point of 2800 °C and a vapor pressure of 1×10^{-13} mbar at 1732 °C [96]. At room temperature bulk hafnia exist in the monoclinic phase, above 1600 °C the monoclinic phase transforms into tetragonal phase and above 2200 °C the tetragonal phase transforms into

the cubic phase (Figure 3.6) Single-layer HfO_2 with different thicknesses was fabricated using RF sputtering (power 400 W), as shown in Figure 3.8 A. Film thickness starting from 60 nm to 120 nm was measured using XRR. The black dotted curve in all the measurements is the simulation curve used to evaluate the thickness and roughness of the sputtered layers that are shown in Table 3.2. As the thickness increases from 60 nm to 120 nm, there is an increase in the number of Kiessig oscillations. No attenuation is observed in the measured range until 100 nm thickness, indicating smooth films. However, the oscillation starts to attenuate in the 120 nm film above 4° incident angle, due to x-ray transmission of Cu-K_{α_1} wavelength having an energy of 8048 eV. Films with higher thicknesses 200 nm and 500 nm were measured using a stylus profilometer. For comparison purpose some thickness measurements of XRR and stylus profilometry are shown in Figure 3.7.

S.No.	Aim / nm	Thickness / nm	Roughness / nm	Density / g cm^{-3}
1	60	59.6 (0.5)	0.21	9.4
2	80	80.2 (0.5)	0.25	9.4
3	100	100.1 (0.5)	0.24	9.4
4	120	120.3 (0.5)	0.28	9.4

Table 3.2: Simulated XRR thickness and roughness of HfO_2 films. The experimental error of thickness determination is ± 0.5 nm.

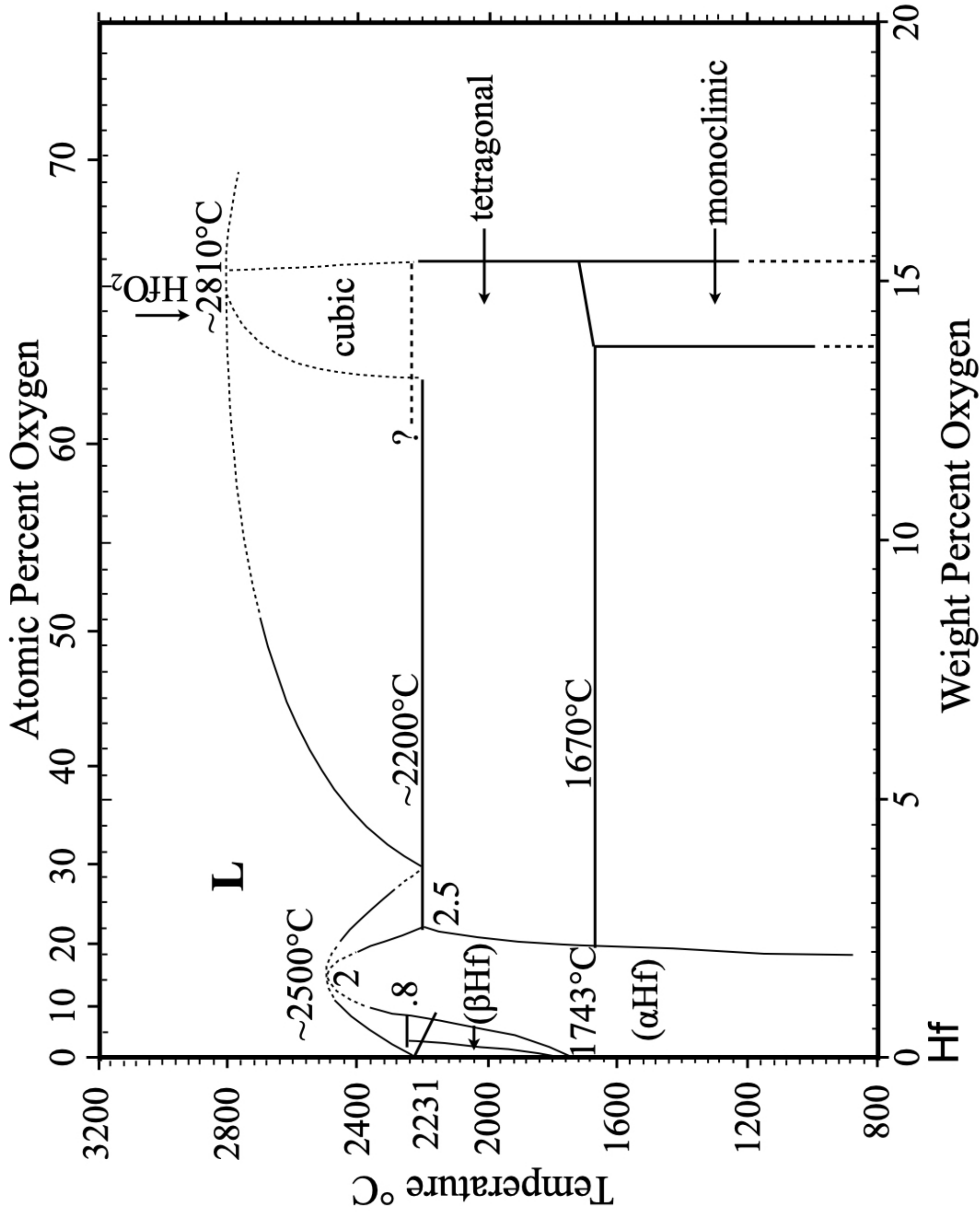

Figure 3.6: Phase diagram of hafnium-oxygen system showing the monoclinic phase at room temperature and the high temperature tetragonal and cubic phases [97].

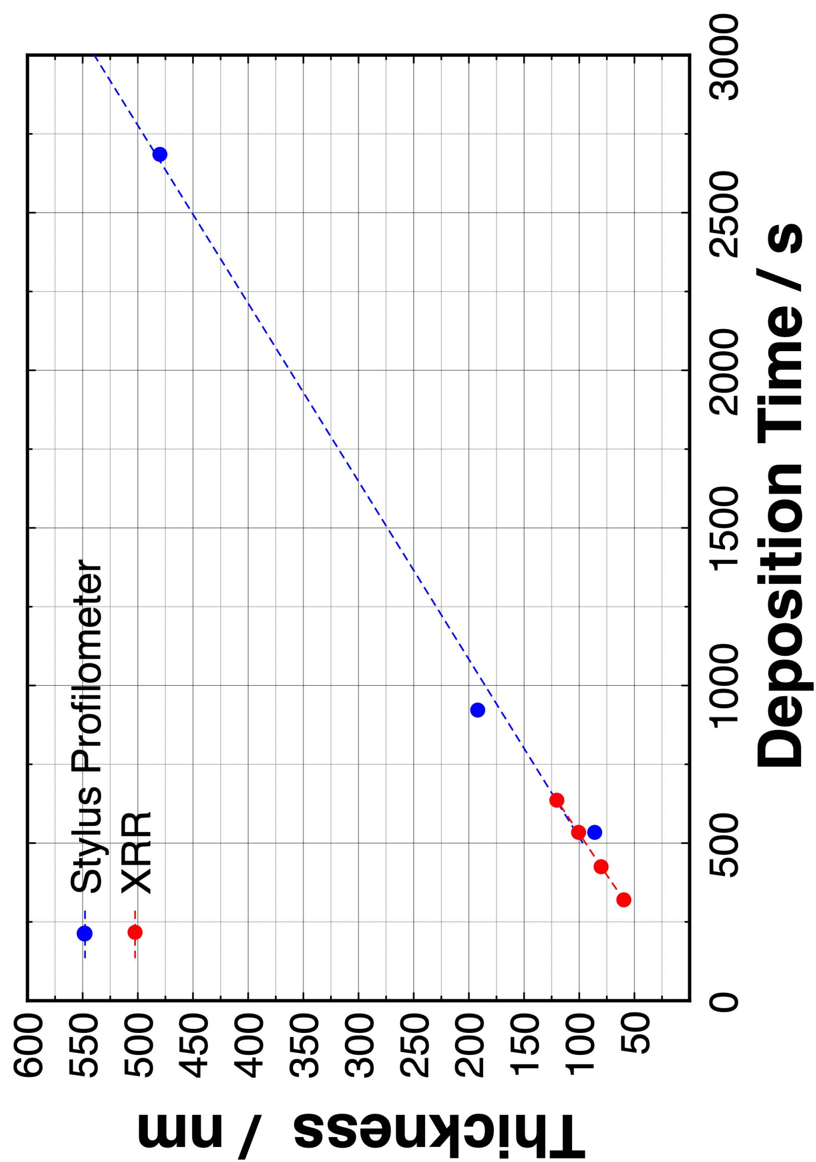

Figure 3.7: Layer thickness comparison between characterization methods - XRR and stylus profilometer for a single layer HfO_2.

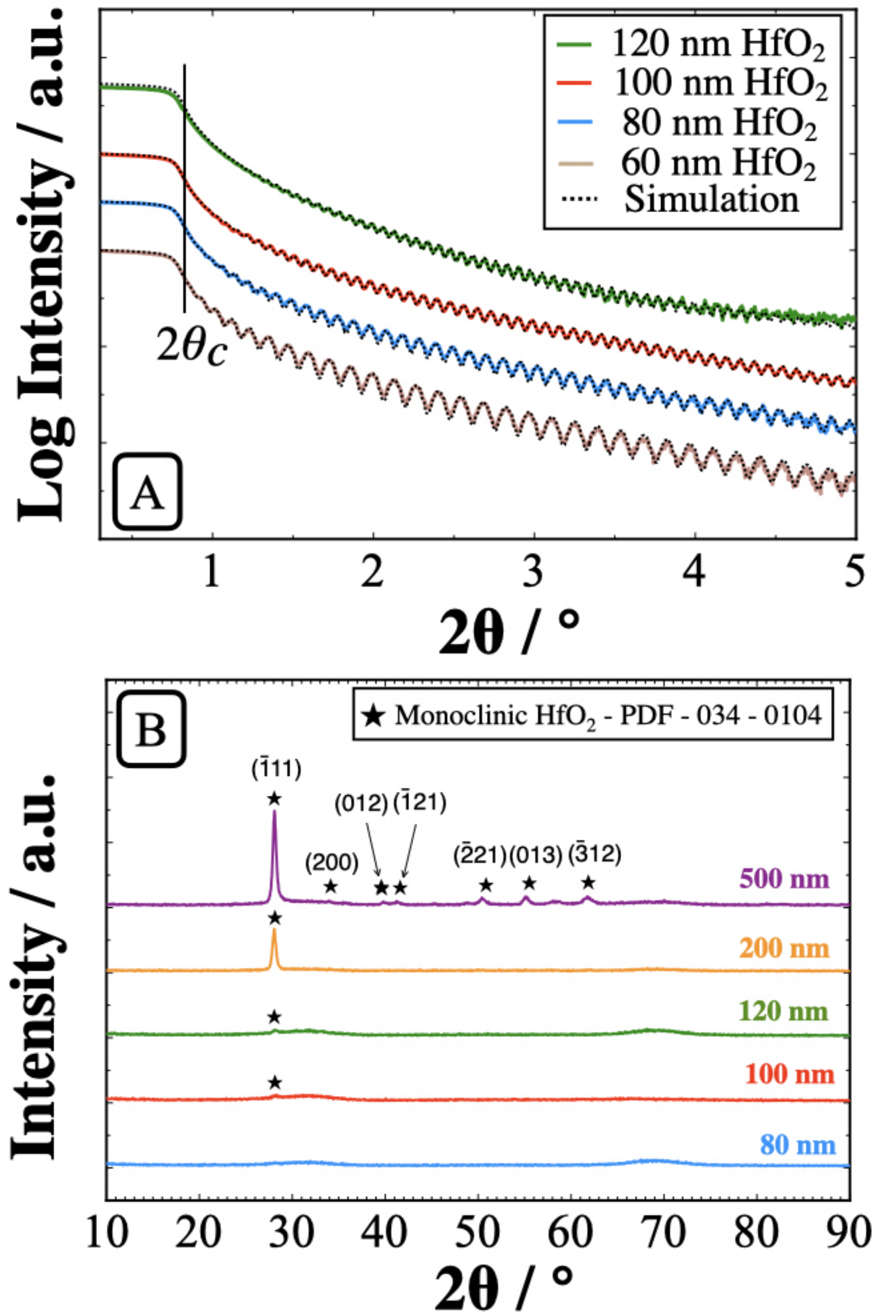

Figure 3.8: XRR scans and XRD diffractograms of single layer HfO_2 having different film thickness.

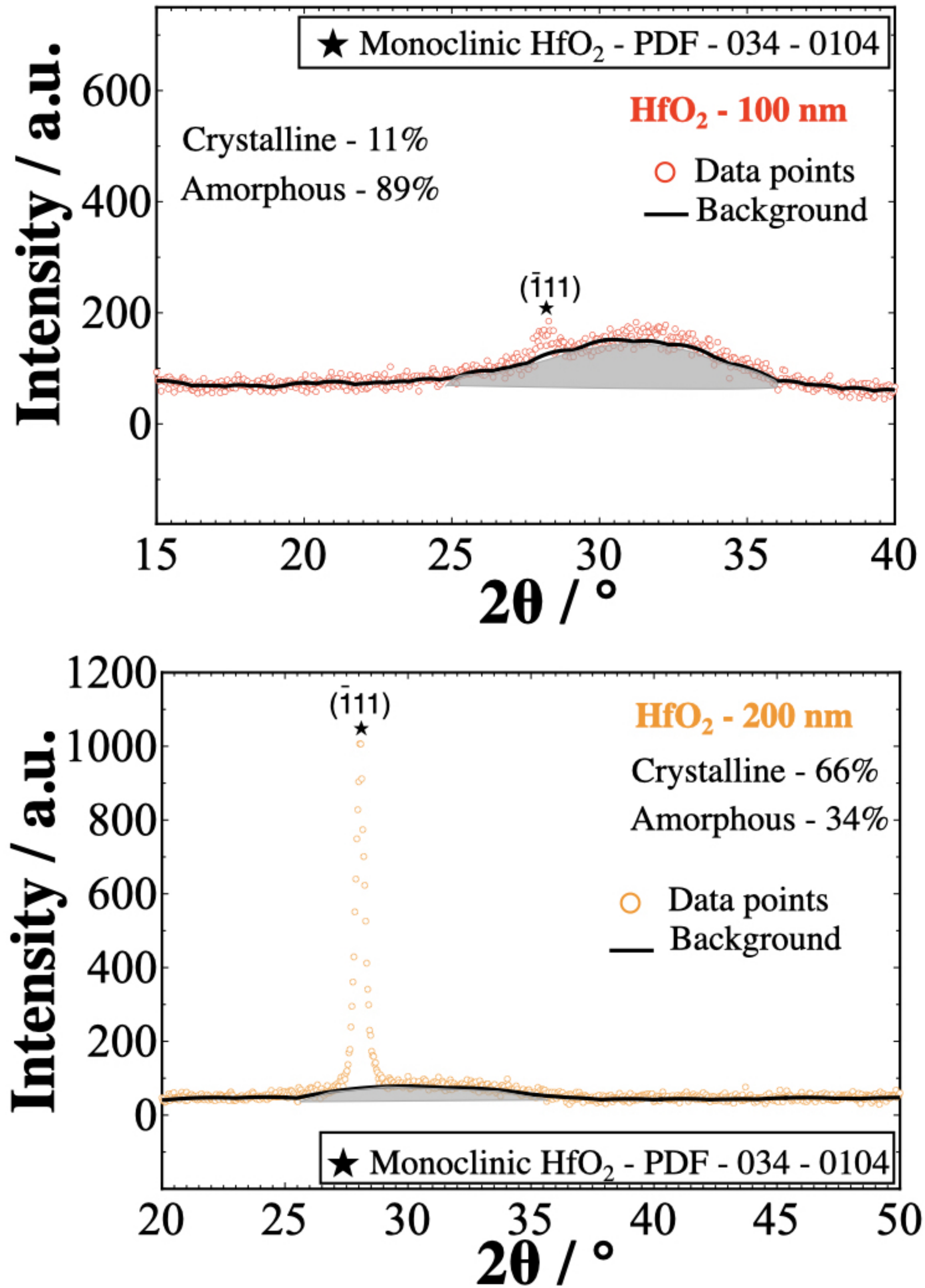

Figure 3.9: Quantitative analysis of amorphous and nanocrystalline phase of a single layer HfO_2.

Figure 3.8 B, shows x-ray diffractograms with different thicknesses starting from 80 to 500 nm. HfO$_2$ films below 60 nm do not have any diffraction peak and are most likely amorphous. Both amorphous (89%)and crystalline (11%) phases coexist in the 100 nm thick HfO$_2$ film (Figure 3.9).The quantitative phase analysis is done using Bruker Eva software, which works on the principle of integral index method that utilizes x-ray diffraction data to determine the crystallinity between experimental sample and a crystalline /amorphous standard [98], [99]. As the thickness of the film increases above 100 nm , a small crystalline peak appears at 28.1°. As the thickness of the film further increases to 200 nm there is a further increase in crystallinity (crystalline 66% and amorphous 34%), which can be verified by the increased intensity of the peak at 28.1°. Higher crystallinity and more peaks are visible for the 500 nm film (Figure 3.8 B). The peaks (-111) at 28.1°, (200) at 34.3°, (012) at 39.6°, (-121) at 40.9°, (-221) at 50.8°, (013) at 57.5° and (-312) at 62.3° match with the monoclinic phase of hafnia in the PDF pattern (00-034-0104). Therefore, the general trend observed shows increased crystallinity for thicker hafnia films.

3.3 W/HfO$_2$ - Metamaterial

This part of the thesis examines the thermal stability of W/HfO$_2$ -based multilayered metamaterial selective emitters at different vacuum conditions. The schematic of a typical metamaterial is shown in Figure 3.10; in this

case, it consists of a bottom layer of W 100 nm in thickness that is used to suppress any optical contribution from the underlying sapphire substrate, followed by six bilayers of W (20 nm) and HfO_2 (100 nm), and a top protective HfO_2 layer (100 nm). A selective emitter provides emissivity ϵ close to 1 for E > E_g ,and ϵ almost 0 for E < E_g, where E is the thermal photon energy. The multilayered metamaterial is designed to effectively function as a thermal emitter in a TPV system that uses a GaSb PV cell with a bandgap of E_g = 0.72 eV (cutoff wavelength λ_c = 1.72 μm). Before we move to the experimental results, it is vital to understand the oxidation process in metals.

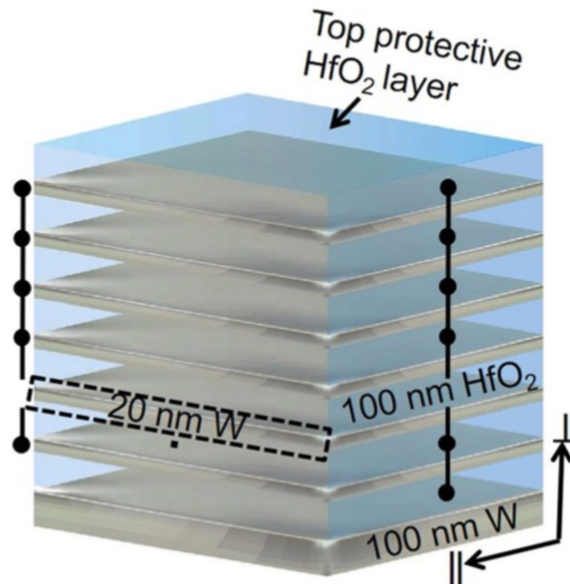

Figure 3.10: Schematic representation of a W-Metamatrial with HfO_2 dielectric interlayers and a top protective layer of HfO_2.

3.3.1 Mechanism of oxidation in W

Oxidation of metals is a straight forward chemical reaction, where the metal and O_2 gas react to form the metal oxide as shown in the following reaction:

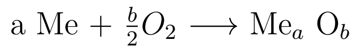

a Me + $\frac{b}{2}O_2 \longrightarrow$ Me$_a$ O$_b$

However, the oxidation mechanism may be complex and depends on various factors like surface orientation, crystal defects on the surface, surface preparation, gas pressure, elapsed time of reaction, and impurities in both the metal surface and gas. The initial step of the oxidation reaction involves the adsorption of O_2 molecules on the clean metal surface. Molecular O_2 dissociates into atomic oxygen. Oxygen atoms migrate to low-energy sites on the metal surface. Finally, oxygen ionizes and forms bonds with the metal atoms of the surface. The formed oxide separates the gas from the metal. If the oxide layer is continuous throughout the metal surface, a further reaction may proceed only through a solid-state diffusion of the reactants across the film. In some metals, the oxide layer formed may be porous, and in such cases, the reaction may be limited by processes occurring at phase boundaries. At high temperatures, oxides may also be liquid or form volatile oxides.

From a thermodynamic point of view, the overall driving force of metal-oxygen reactions is the change in the free energy associated with the oxide formation from the reactants. The latter condition of oxide formation is favorable only if the ambient O_2 partial pressure is larger than the dissociation pressure of the oxide in equilibrium with its metal. It is essential to note

that oxides are defective and they manifest deviations from stoichiometry. The partial pressure of O_2 above an oxide surface is a function of the non-stoichiometry and its defect structure [100]. Even though free energy is the driving force, it is independent of the rate of the reactions, which is a kinetic problem. The reaction rate depends on the reaction mechanism and the rate governing part of the oxidation process.

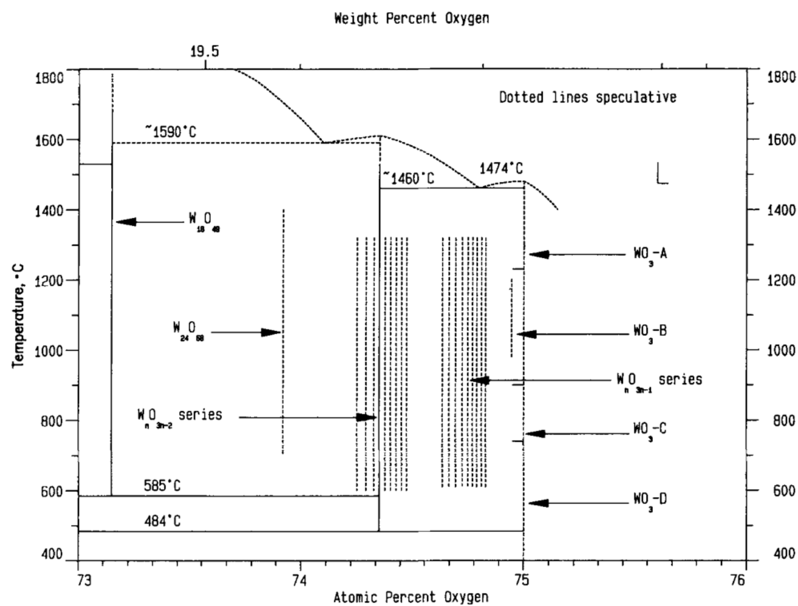

Figure 3.11: Phase diagram of W-O system. WO_3 has been identified by several names like tungsten oxide , tungsten(VI) oxide, tungstic oxide, tungsten trioxide, tungstic anhydride, tungstic acid, tungstite and α tungsten oxide. Most or all of these names were used before its polymorphism and non-symmetry transitions were known. Therefore the author [101] decided to arbitrarily denote the solid WO_3 variety occurring in equilibrium with liquid WO_3 by WO_3-A, WO_3-B, WO_3-C, and WO_3-D, each successive variety formed with falling temperature for which a report of evidence was found in literature.

Figure 3.11 shows the equilibrium phase diagram of W-O system [101], invaluable information like feasible reaction products, sequential formation of different oxides can be predicted. One should remember that these reactions signify dynamic systems with a higher probability of forming metastable phases that may not be stable at higher temperatures.

3.3.2 Ex-situ annealing in different vacuum pressure

The thermal stability of the selective emitter was tested by annealing it at different temperatures 1100 °C, 1150 °C, and 1200 °C at 2×10^{-2} mbar vacuum pressure in a Linkam chamber pumped by diaphragm pumps. Ex-situ x-ray diffractograms of the metamaterial, as-prepared and after annealing it at different temperatures are shown in Figure 3.12. The as-prepared sample contains four expected peaks from bcc -W (110) 39.8° , (200) 58° , (211) 72.5°, and the higher-order peak (220) 86°. Preferred orientation of (110) peak is typical for bcc metals after thin film preparation [90], as there is a preference for orientation that place the most densely populated atomic planes parallel to the substrate in films grown by magnetron sputtering. The FWHM of the strongest tungsten peak (110) is 0.56°, and the calculated grain size using the Scherrer's formula is 15 nm. The other prominent peaks 28° (-111), 46° (-202), 48° (-212), 61.7° (-312) are visible in the scan that belong to the monoclinic HfO$_2$ phase. The FWHM of the strongest HfO$_2$ peak (-111) is 0.49°, and then the calculated grain size is 17 nm. The desired spectral emissivity is around 1.5 μm for the as-prepared metamaterial (black

curve) as shown in Figure 3.13.

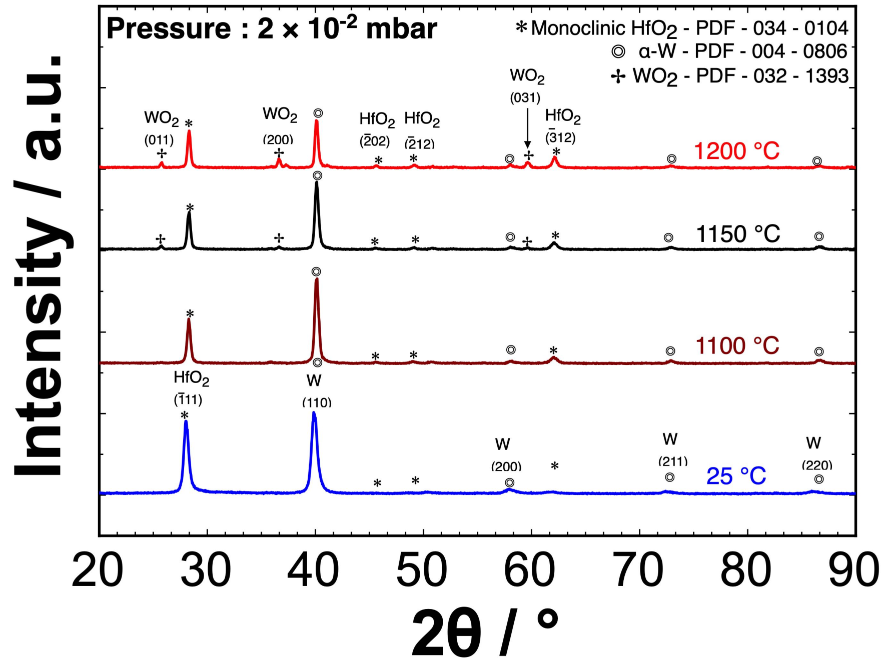

Figure 3.12: Ex-situ diffractograms of W-metamaterial annealed in vacuum pressure of 2×10^{-2} mbar. The heating rate was 10 °C /min, holding time during isothermal annealing was 6 h and the cooling rate was 10 °C /min. All scans are normalized to the background.

The next sample in the waterfall plot (Figure 3.12) was annealed at 1100 °C for 6 h. No new peaks are found in the diffractograms compared to the as-prepared sample. Nevertheless, due to annealing at 2×10^{-2} mbar and the influence of oxygen partial pressure, there is a irreversible change (red shift) (blue curve, Figure 3.13) in the spectral selectivity of the emitter compared to the as-prepared sample. However, this is changed for samples annealed at 1150 °C and 1200 °C and they show additional peaks at 25.8° (011), 36.8°

(200), and 59.7° (031) that corresponds to the monoclinic WO_2 phase (Figure 3.12), confirming the oxidation of the W layer present in the metamaterial. The oxidation effect is also visible in FTIR meaurements (Figure 3.13), where a complete degradation of spectral features for the sample annealed at 1150 °C and 1200 °C is clearly visible.

To confirm the oxidation of W observed in XRD scans, STEM-EDS analysis (Figure 3.14) was performed on the multilayered samples. The W elemental map shows distinct layer structure in the as-prepared sample, whereas interruptions are found in the W layer annealed at 1100 °C and 1200 °C.

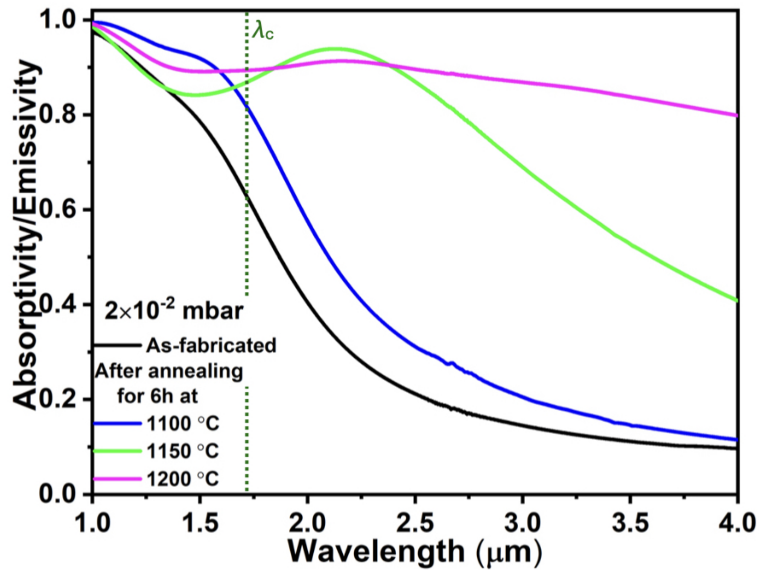

Figure 3.13: Experimental spectral aborptivity/emissivity of the layered metamaterial emitter structures. Comparison of structures as-fabricated and after 6 h annealing at various temperatures at 2 $\times 10^{-2}$ mbar vacuum pressure.

The O-K_α elemental mapping confirms the presence of oxygen in the first W layer for the 1100 °C sample and almost in all layers for the sample annealed at 1200 °C, along with the presence of some voids.

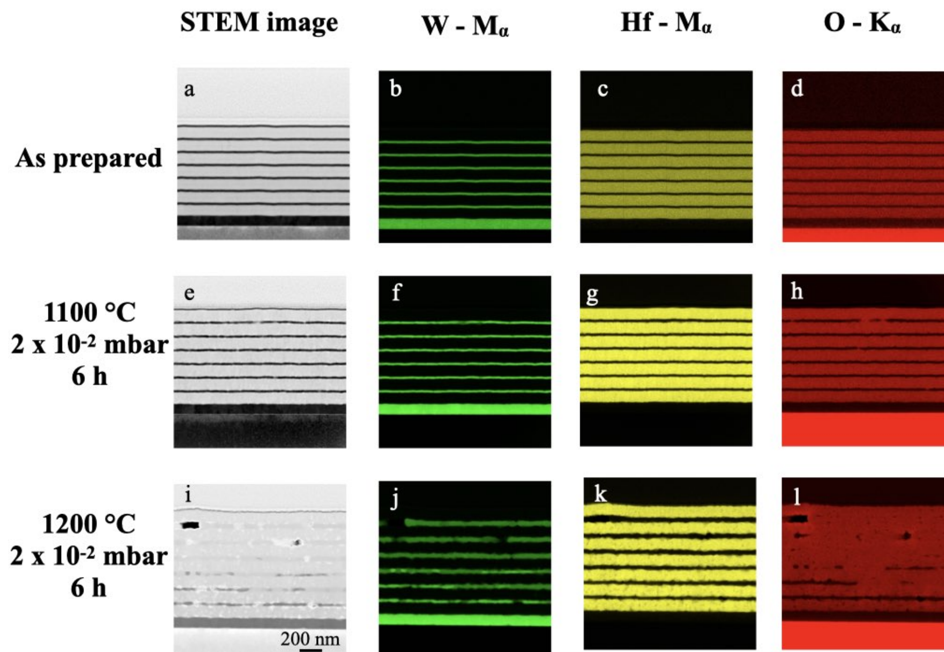

Figure 3.14: A cross section STEM-EDS analysis to validate oxidation of W in a W-metamaterial after annealing at 1100 °C and 1200 °C. For comparison purpose an as-prepared metamaterial is also shown. STEM-HAADF images (a,e and i), W-M_α elemental mapping (b,f and j), Hf-M_α elemental mapping(c,g and k) and O-K_α elemental mapping(d,k and l). Presence of oxygen in the W layers are visible in (h and l) due to oxidation of W layers.

There are at least two possible ways by which the oxygen reaches the W for oxidation to occur. Oxygen of the HfO_2 can reach the W layer by inter

diffusion and the second way is the diffusion of residual oxygen present in the chamber. Considering the first case, the Gibbs energy of formation ΔG_f of HfO_2 at 1126 °C is -892 kJ mol^{-1} which is much less than the enthalpy of formation of WO_2, -339 kJ mol^{-1} [102]. According to thermodynamics, when $\Delta G < 0$, the reaction occurs spontaneously, and in the latter case, the formation of HfO_2 is more favorable than, in other words, oxygen prefers to stay with HfO_2 rather than forming WO_2 in this case.

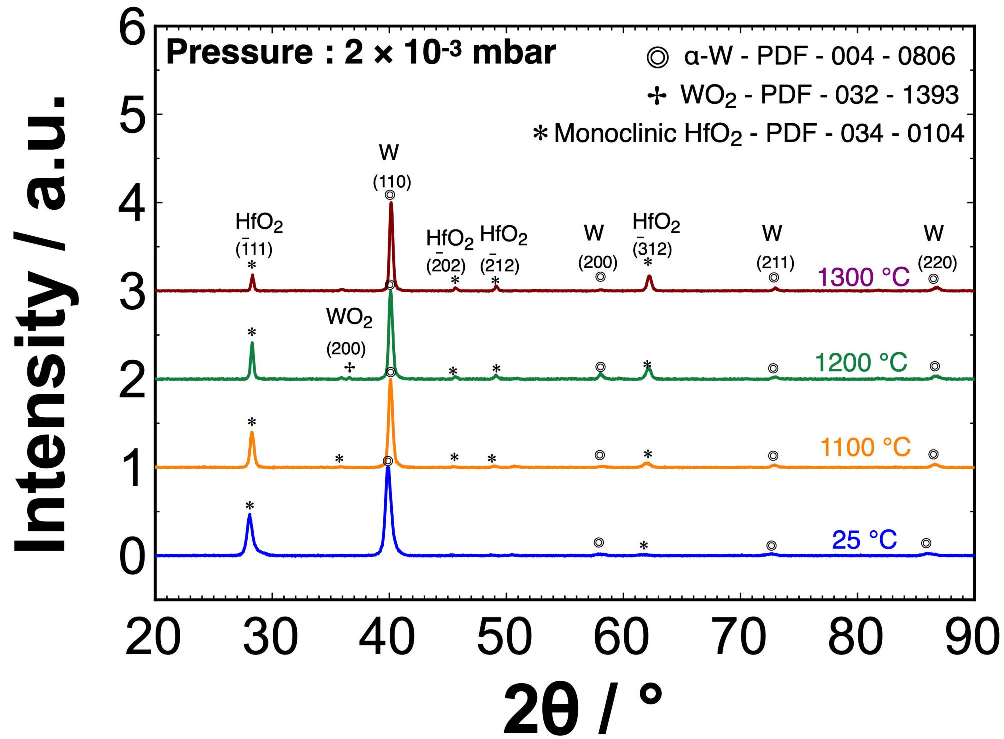

Figure 3.15: Ex-situ diffractograms of W-metamaterial annealed in vacuum pressure of 2×10^{-3} mbar. The heating rate was 10 °C /min, holding time during isothermal annealing was 6 h and the cooling rate was 10 °C /min. All scans are normalized to the background.

Hence the inter diffusion of O_2 from HfO_2 can be seen as very unlikely. Therefore the very likely possibility for the oxygen to approach W is from the residual oxygen present in the annealing chamber that diffuses through the HfO_2 layer by grain boundary diffusion or bulk diffusion. The detailed mechanism of oxygen transport to the W layers is elaborated in Section 3.4.

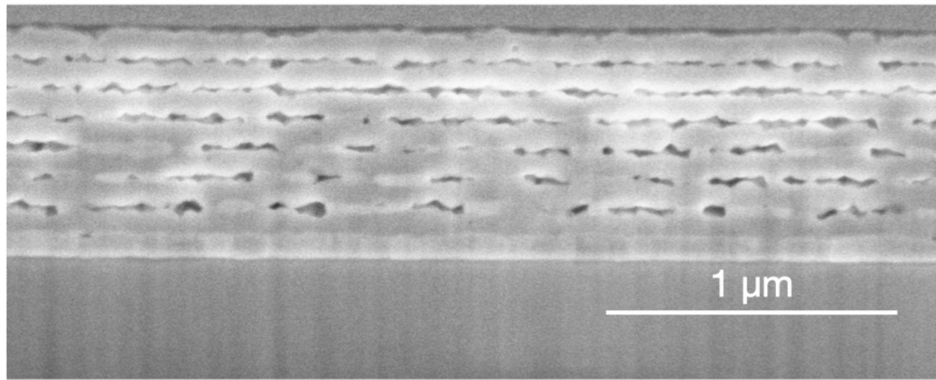

Figure 3.16: Cross section of a FIB- SEM image showing W metamaterial after annealing it at 1300 °C for 6 h at 2×10^{-3} mbar vacuum pressure. Absence of W or presence of holes in the W layer is seen due to sublimation of volatile tungsten oxide.

Further annealing experiments were performed by reducing the vacuum pressure by one order to 2×10^{-3} mbar to validate the oxidation behavior of W at elevated temperatures. Figure 3.15 shows ex-situ x-ray diffractograms of the metamaterial selective emitter annealed at 1100 °C, 1200 °C, and 1300 °C. Only one peak (200) from the monoclinic phase of WO_2 is visible for the 1200 °C annealed sample. The WO_2 peaks' intensity is less than the one of the previous case at one order lower pressure because less WO_2 is

formed. However, on further increasing the temperature to 1300 °C, absence of WO_2 is observed because the WO_2 transforms to volatile $WO_{2.9}$ and at temperatures above 1200 °C the rate of sublimation is quicker than the rate of oxide formation. The absence of tungsten can be seen in the cross section SEM images in Figure 3.16. The oxidation and later sublimation of volatile oxides is a complex mechanism as it depends on the temperature and the partial pressure of oxygen available. The oxidation mechanism is discussed in details into different zones in Section 3.4.

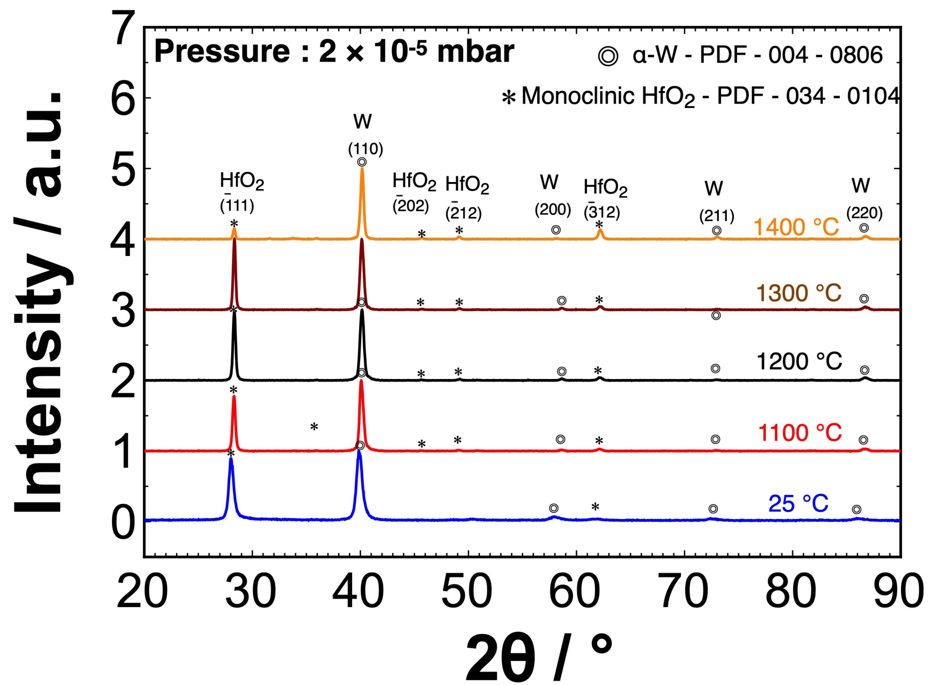

Figure 3.17: Ex-situ diffractograms of W-metamaterial annealed in vacuum pressure of 2×10^{-5} mbar. The heating rate was 10 °C /min, holding time during isothermal annealing was 6 h and the cooling rate was 10 °C /min. All scans are normalized to the background.

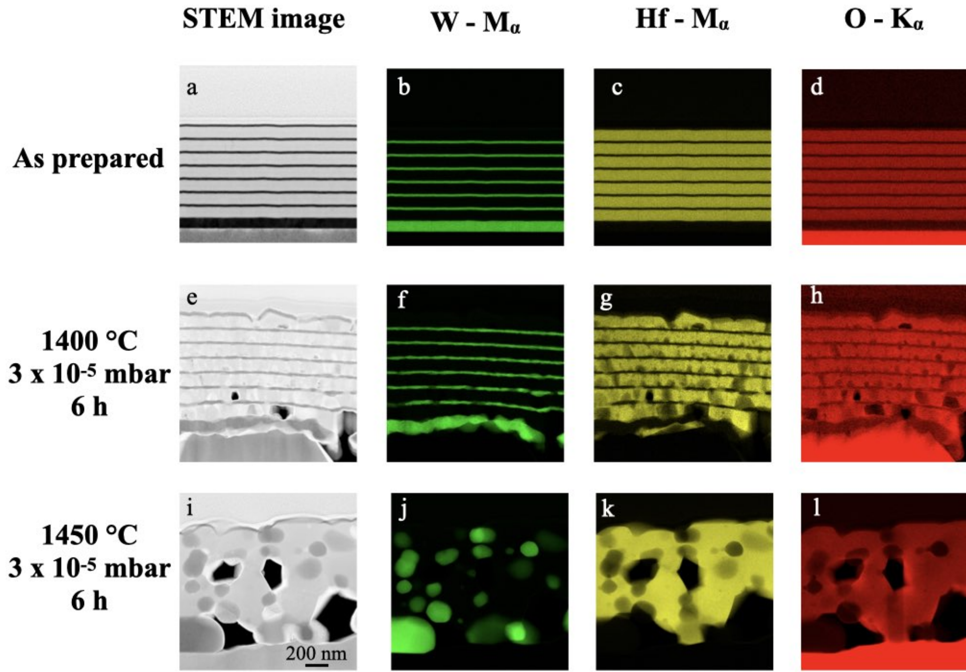

Figure 3.18: A cross section STEM-EDS showing degradation of W above 1450 °C . For comparison purpose an as-prepared metamaterial is also shown. STEM-HAADF images(a,e and i),W-M$_\alpha$ elemental mapping(b,f and j), Hf-M$_\alpha$ elemental mapping (c,g and k) and O-K$_\alpha$ elemental mapping (d,k and l). None of the tungsten layers are oxidized. Above 1400 °C the layered structure is lost, as W tries to form spheres in order to reduce interface free energy.

The last ex-situ annealing experiments were performed at a high vacuum of 2×10^{-5} mbar at different temperatures between 1100 °C and 1450 °C. Figure 3.17 shows the ex-situ x-ray diffractograms of the annealed samples. All the scans are normalized to the background. There are no reflections of WO_2 in any of the scans. This is a clear indication that none of the W

layers are oxidized. The intensity of the (110) bcc W peak increases as the annealing temperature increases. The (-111) peak of HfO_2 starts to grow in intensity as the temperature rises to 1350 °C, and later a drop in intensity is observed at a higher temperature. It is also essential to monitor the increase in (-312) peak intensity which signifies anisotropy of thermal expansion in the HfO_2 layers.

The STEM-EDS analysis is shown in Figure 3.18. After annealing the metamaterial at 1400 °C for 6 h, the layer structure is still preserved without any oxidation of W layer. The W-M_α and O-K_α elemental mapping shows no presence of oxygen in the W layer. However, in the metamaterial annealed at 1450 °C, the layer structure is not preserved anymore. The W layer reduces its surface energy by self-diffusion, grain growth dominates and spheres are formed to minimize the surface-to-volume ratio.

3.3.3 Ex-situ annealing in inert gas atmosphere

The degradation mechanism of the metamaterial selective emitter based on ex-situ XRD analysis and STEM-EDS shows the failure at vacuum pressure above 2×10^{-3} mbar is due to oxidation, and at high vacuum pressure below 2×10^{-5} mbar the layer structure is not preserved anymore as tungsten forms spheres to minimize the interface energy. However, selective emitter in TPV systems working at high vacuum conditions below 2×10^{-5} mbar requires turbo molecular pumps for practical applications.

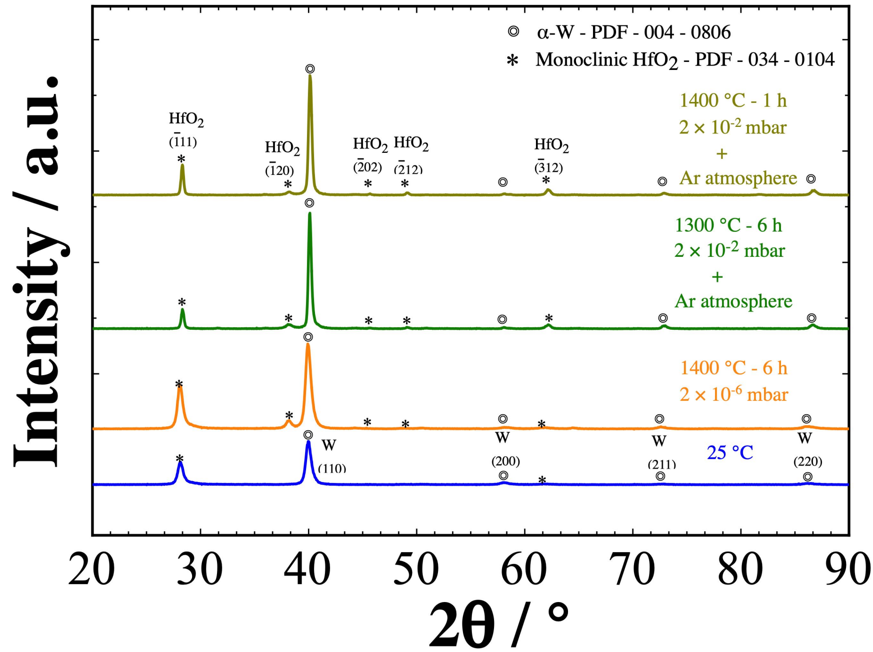

Figure 3.19: Ex-situ diffractograms of W-metamaterial (100 nm HfO_2 - Top layer /(30 nm -W / 100 nm - HfO_2)×6/ 200 nm - W bottom layer) annealed in Ar gas atmosphere. All scans are normalized to the background. The scan in orange is the W metamaterial (100 nm HfO_2 - Top layer /(20 nm -W / 100 nm - HfO_2)×6/ 200 nm - W bottom layer) annealed in a vacuum pressure of 2×10^{-6} mbar without any argon atmosphere, as for comparison purpose. Absence of WO_2 peaks is observed in all the scans.

By using a rotary vane pump, vacuum pressure up to 2×10^{-2} mbar can be achieved. At this pressure, the thermal stability of the selective emitter tested so far is 1000 °C. The thermal stability of the selective emitters was further tested in a vacuum chamber having a pressure of 2×10^{-2} mbar enclosed in an Ar gas atmosphere. The purity of the Ar gas used is 99.999%. The residual oxygen partial pressure in the vacuum chamber is in the order

of 4×10^{-8} mbar.

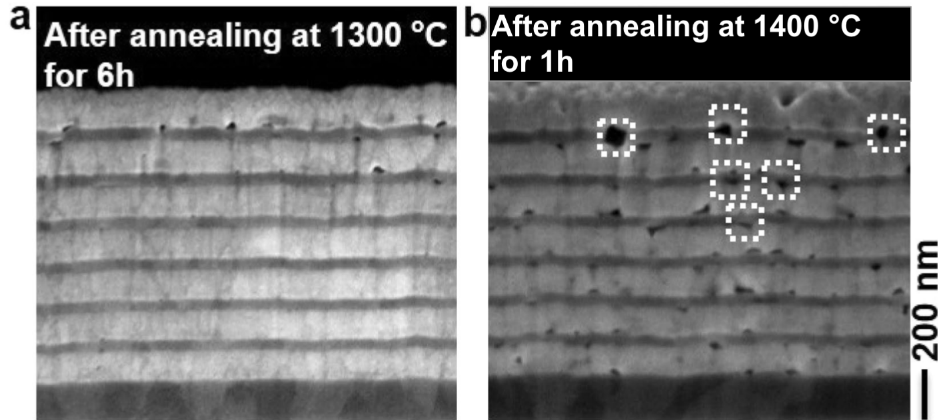

Figure 3.20: SEM image of W-metamaterial annealed in Ar gas atmosphere at (a) 1300 °C for 6 h and (b) 1400 °C for 1 h [57].

The thickness of the W-layer in the 6 bilayers is **30 nm** compared to **20 nm** in the previous experiments. An increase of 10 nm in the W-layer shows a decrease in mid-infrared absorptivity/emissivity by a factor of two (not shown) [57]. Figure 3.19 shows the ex-situ diffractogram of selective emitters, as-prepared, post-annealed at 1300 °C, and 1400 °C at 2×10^{-2} mbar for 6 h. For comparison purposes, another selective emitter annealed for 1 h at 1400 °C, and a vacuum pressure of 2×10^{-6} mbar is added to the plot.

Neither of the diffractograms contains any peaks from the monoclinic WO_2 phase. Therefore, it is attractive for TPV applications to use the selective emitter in an inert Ar gas atmosphere. The SEM pictures in Figure 3.20(a) show no voids in any of the W layers annealed at 1300 °C for 6 h.

However, despite no WO_2 peaks in the diffractogram, some voids (Figure 3.20(b))are found in the W layer annealed at 1400 °C already at 1 h. The former experiments show that a W based metamateral is stable at 1300 °C in an environment having vacuum pressure 2×10^{-2} mbar, enclosed by Ar gas atmosphere.

3.4 Determination of the thermal stability of $HfO_2/W/HfO_2$ system by in-situ XRD

This section focuses on in-situ x-ray diffraction (XRD) experiments of a simplified 3-layer-system of 100 nm HfO_2 / 20 nm W / 100 nm HfO_2 shown in Figure 3.21, to investigate the time-dependence of the structural and microstructural changes of the layer materials at high temperatures. The 3-layer-system represents a small sub-unit extracted from the metamaterial.

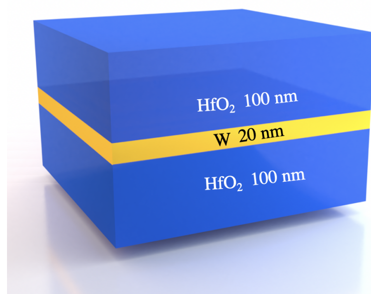

Figure 3.21: Schematic of the 3-layer-system used in the annealing experiment. A 3-layer-system is a sub-unit extracted from a multilayered metamaterial containing only a single metal layer sandwiched between two dielectric layers.

The primary goal of using a 3-layer-system is to understand the mechanism of oxidation in a single W layer sandwiched between two HfO_2 layers, that leads to initial structural changes, followed by degradation at various annealing temperatures and duration's. In-situ annealing experiments also provide information on the changes observed in the 3-layer-system due to high operating temperatures such as phase formation, interplanar spacings and grain size evolution, and alterations of the volume fractions of the observed phases. The chapter focuses on understanding the phase changes that occur in the dielectric layer leading the pathway for the degradation in the metal layer by oxidation process above 1000 °C in high-vacuum conditions below 3×10^{-6} mbar.

Two samples of 3-layer-systems prepared from the same batch are first annealed at 650 °C and 1520 °C for 6 h, and these experiments allow us to investigate the changes of crystal structure and phase formation. Diffractograms were recorded at regular intervals during the temperature ramp. The diffraction patterns of a 3-layer-system recorded at different temperatures during the temperature ramp are shown in Figure 3.22, from room temperature up to 1520 °C.

The first diffractogram in black shows the measurement performed at room temperature, peak (110) at 39.9° correspond to the body-centered cubic (bcc) phase of $\alpha - \mathrm{W}$. Whereas, in HfO_2, a monoclinic and amorphous phase coexist together in the as-prepared state. It is worthwhile to mention that the phase formation in HfO_2 layers is influenced by the major impurity element

Zr that has a concentration below 4000 ppm. The (-111) peaks at 28.3° belongs to the monoclinic phase of HfO_2, whereas the broad bump around 30.4° represents the amorphous phase (as mentioned earlier in Figure 3.9). Performing a peak fit shows the FWHM of the monoclinic phase is 0.48° and one of the amorphous phase is 5.2°. Using Bruker EVA software, it is estimated that the volume fraction of the monoclinic and amorphous phase is 56% and 44% in the 3-layer-system after preparation.

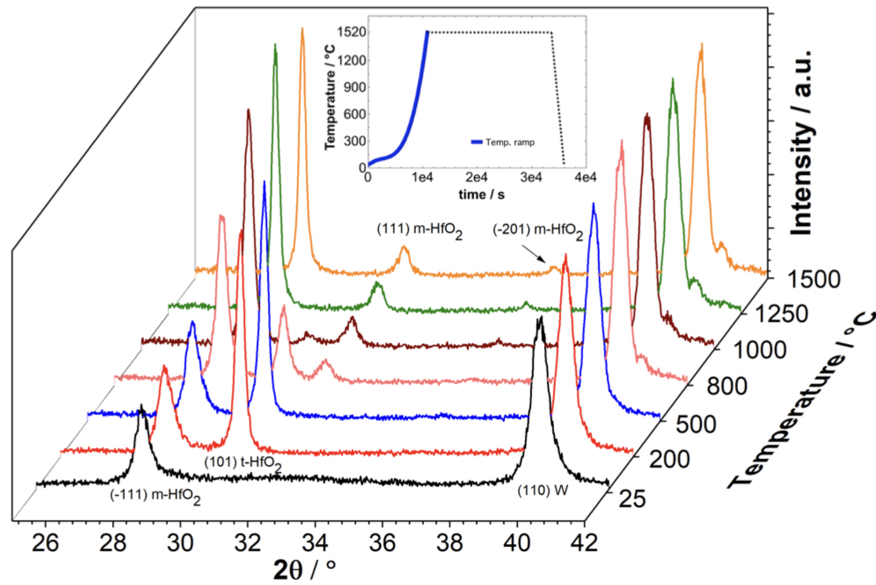

Figure 3.22: In-situ XRD diffractograms of a 3-layer-system from room temperature until 1520 °C at 3×10^{-6} mbar vacuum conditions. During this temperature increase (represented by thick blue line in the inset, which shows the whole annealing experiment) a tetragonal phase of HfO_2 appears around 200 °C and later slowly disappears above 800 °C.

The peaks get sharper and shift to higher angles as the temperature ramp increases approaching equilibrium bulk value of the corresponding material. The broad, amorphous bump of HfO_2 at room temperature starts to disappear. Literature reveals, that HfO_2 exhibits polymorphic behavior [44]. As the temperature reaches 200 °C, a new peak (101) representing the tetragonal phase of HfO_2 emerges at 30.3°. The (101) peak intensity continues to become more pronounced until 550 °C, and above 750 °C a decline in intensity is observed. The calculated d values of the tetragonal phase are d_{101} = 0.2951 nm at 200 °C and d_{101} = 0.2968 nm at 750 °C. No thermal expansion data for tetragonal hafnia is found at this temperature range. The small difference and increase in d values, is due to thermal expansion.

Meanwhile, the intensity of the monoclinic peak (-111) of HfO_2 grows, at 500 °C the intensity is twice, and at 1250 °C the intensity is thrice compared to the intensity at room temperature. The reason for the increase in intensity is due to the transformation of the tetragonal phase into the more stable monoclinic phase at high temperature. These results are in good agreement to the experiments carried out by Ushakov et al. [103] and Zhao et al. [104] as they observed amorphous HfO_2 phases that crystallize into tetragonal phase first and later transform into the stable monoclinic phase in thin films, which were prepared by sol-gel, pulsed laser deposition (PLD) and atomic layer chemical vapor deposition (ALCVD). As the temperature increases above 1000 °C, more new peaks corresponding to the monoclinic phase of HfO_2 start to appear, such as (111) and (-201) due to anisotropy. In the case of

tungsten no phase transformations are observed, however the FWHM of the (110) peak reduces slightly indicating grain coarsening in the W layer.

The second crucial part of the in-situ annealing measurements is the isothermal heating. Here the diffractograms are recorded at constant temperature as a function of time, which provide important information regarding kinetic changes in the 3-layer-system. Figure 3.23 shows diffractograms in the range of 26° - 43° at 1520 °C spanning over 6 h.

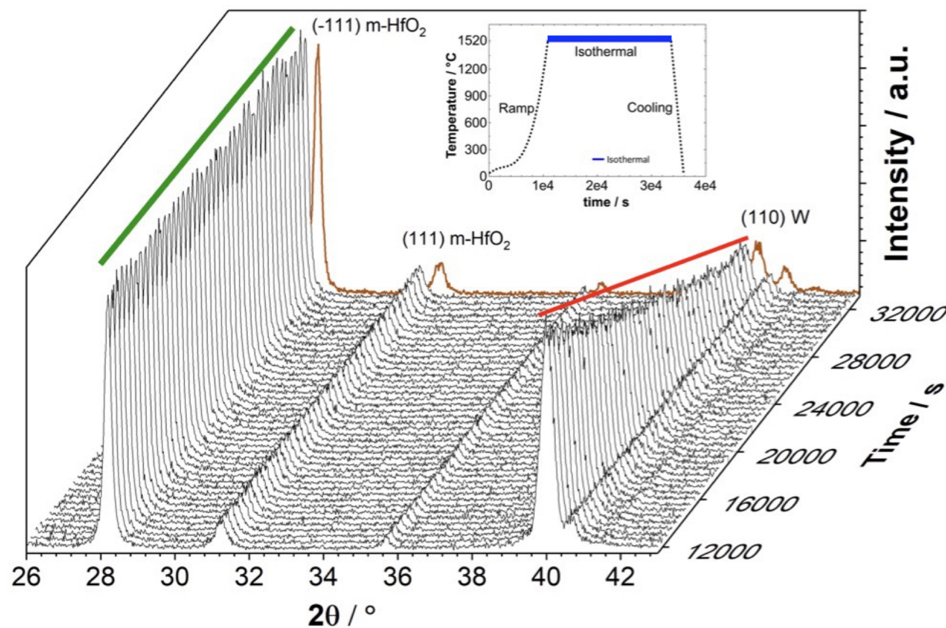

Figure 3.23: In-situ X-ray diffraction measurements of a 3-layer-system performed during isothermal annealing at 1520 °C for 6 h at 3×10^{-6} mbar. The inset shows the whole annealing experiment with the isothermal part marked by a thick blue line. The (-111) peak of the monoclinic HfO_2 phase is unchanged, however, the (110) peak of the bcc W phase is decreased successively. The last diffractogram colored in brown is measured at room temperature, at the end of the annealing experiment.

A slow increase in 2θ values is seen for both the (-111) monoclinic HfO_2 and (110) bcc W peaks. Over a period of time the peaks get sharper and the FWHM of both the peaks shrink due to grain coarsening. During the entire isothermal annealing no new phase or composition change noticed, which is ideal for the application as high-temperature stable materials. The most eye catching feature observed is the drop in intensity of the (110) bcc W peak over time, whereas the (-111) monoclinic HfO_2 remains constant during the 6 h annealing period.

On cooling back the sample to room temperature after 6 h, no additional phase of HfO_2 or any reverse tranformation into the tetragonal phase is observed and it persists in the monoclinic phase. This is represented in the last scan (brown color, Figure 3.23) of the sequence of diffraction patterns, in which a shift in 2θ value to a higher angle is observed due to thermal contraction. It is worthwhile to mention that the in-situ scans give us the tools to reveal information about internal and as well irreversible changes of structure, phase and microstructure.

The time-dependent changes of the interplanar spacing d_{110} of bcc W, indicates the first sign of modifications in the 3-layer-system. Figure 3.24, A and B, shows the influence at two annealing temperatures 650 °C (red markers) and 1520 °C (blue markers). Both the samples were prepared in the same batch and hence the d-values measured at room temperature are nearly the same, $d_{110} = 0.2255$ nm for the sample 650 °C and $d_{110} = 0.2256$ nm for sample 1520 °C. The small difference of 0.0001 nm is a systematic

error caused initially during adjusting the z-stage of the diffractometer.

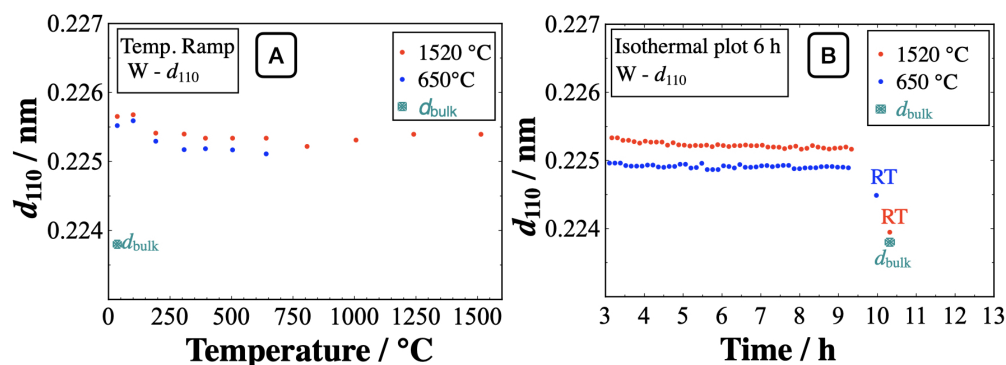

Figure 3.24: Interplanar spacing d_{110} of bcc W in the 3-layer-system (A) as a function of temperature during annealing ramp and (B) as a function of time during isothermal annealing. Blue markers represent 650 °C and red markers represent 1520 °C. The duration of the isothermal part is 6 h.

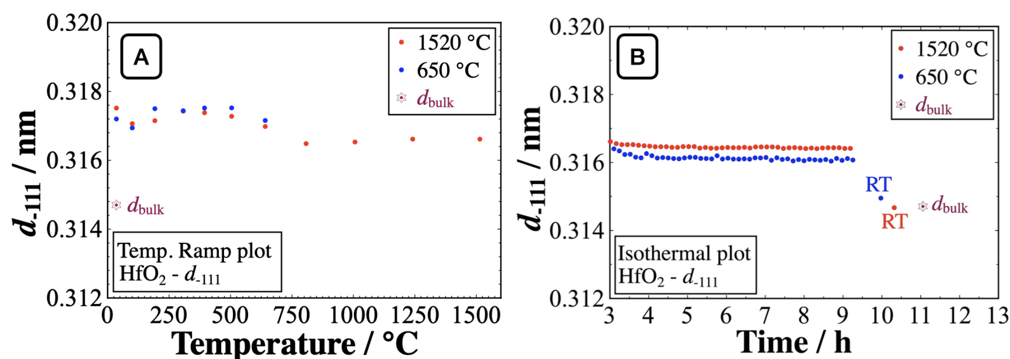

Figure 3.25: Interplanar spacing d_{-111} of monoclinic HfO_2 in the 3-layer-system (A) as a function of temperature during annealing ramp and (B) as a function of time during isothermal annealing. Blue markers represent 650 °C and red markers represent 1520 °C. The duration of the isothermal part is 6 h.

It is important to compare the d-values at two temperatures to under-

stand the significance of grain growth, stress relaxation and recrystallization in particular in regards to high-temperature stability. The small increase in d-values at 200 °C initially, is due to thermal expansion. This is still too small for stress relaxation. The observed thermal expansion is 4×10^{-6} K^{-1} and it is in good agreement with bulk W, i.e. 4.12×10^{-6} K^{-1}[105]. As a result of atomic peening during magnetron sputtering at low Ar pressure of 2×10^{-3} mbar, the prepared films are most likely in a state of compressive stress. Thus, the growing film is densified by later arriving atoms having mean kinetic energy in the order of 2 - 10 eV [106]. Above 200 °C, there is sufficient energy for atomic mobility and hence a drop of the d-values is observed. Later during isothermal annealing, there is initially a drop in d-values due to stress release, but later it is gradually counter-reacted by the thermal expansion and the d-values stabilize at 0.2248 nm for 650 °C sample and 0.2252 nm for 1520 °C sample.

After the completion of the isothermal annealing and on cooling the sample back to room temperature the d-value of the sample annealed at 1520 °C almost reaches the tabled equilibrium value of bulk W $d_{110} = 0.2238$ nm (PDF card 00-004-0806). The d-values are 0.2239 nm (1520 °C) and 0.2244 nm (650 °C). The d-value of the sample annealed at 1520 °C is lower and closer to the bulk equilibrium values due to complete stress removal, whereas the sample annealed at 650 °C ends up with a comparatively higher d-value due to partial release of stress. The above measurements demonstrate that there is a significant alteration of the interplanar spacing d_{110} of bcc W when

annealed at 1520 °C.

For monoclinic HfO_2 (Figure 3.25), the thermal changes are in general more moderate, the interplanar spacing d_{-111} measured at room temperature is 0.3167 nm for 650 °C (blue markers) and 0.3165 nm for 1520 °C (red markers). Initially, both specimens follow a similar behavior, there is again an increase in the interplanar spacing due to thermal expansion. Later the d values relax and stabilize during the isothermal stage. On cooling the 3-layer-system at the end of the isothermal stage, interplanar spacings are close to the equilibrium value $d_{-111} = 0.3147$ nm (PDF card 00-034-0104) of bulk monoclinic HfO_2 at room temperature. The changes of the d-values for the sample after annealing at 1520 °C, $d_{-111} = 0.3142$ nm are again more pronounced than the one after 650 °C, $d_{-111} = 0.3149$ nm. The structural stability of the monoclinic HfO_2 phase is overall sufficient for a refractory dielectric layer in a metamaterial.

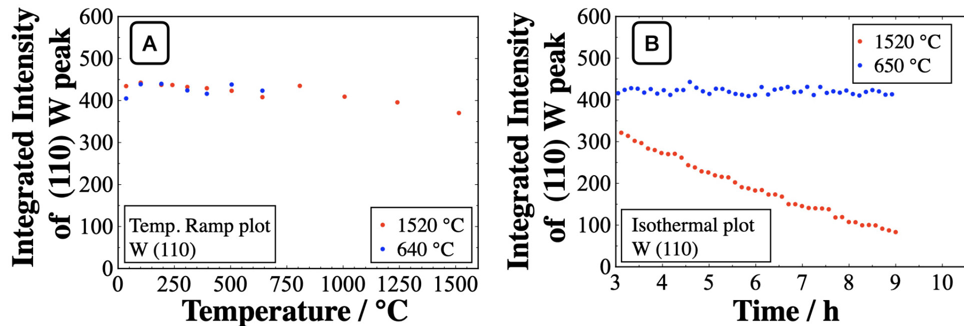

Figure 3.26: Integrated intensity of (110) bcc W in 3-layer-systems annealed for 6 h at temperatures 650 °C (blue markers) and 1520 °C (red markers) (A) as a function of temperature during annealing ramp and (B) as a function of time during isothermal annealing.

From the quantitative analysis of powder mixtures, it is known that the integrated intensity of a diffracted peak for a particular phase depends on the concentration of the phase. Therefore, to quantify the changes undergone by W during the heat treatment, the integrated intensity, i.e, the area under the diffraction peak (110) annealed at 650 °C (blue markers) and 1520 °C (red markers), are shown in Figure 3.26. The background subtracted integrated intensity is directly proportional to the volume fraction of the W present in the 3-layer-system. The integrated intensity is constant for the sample annealed at 650 °C during the ramp and the isothermal annealing. But for the sample annealed at 1520 °C, the integrated intensity is relatively constant during temperature ramp, followed by a substantial drop in intensity during the isothermal annealing. The loss in intensity of (110) W peak can be related to a loss in volume fraction of W in the 3-layer-system. Another possibility of intensity reduction can be due to roughness, but if there is increase of roughness in the 3-layer-system, the impact should be visible in the HfO_2 peaks as well. It is worthwhile to mention that there is no change noticed in the HfO_2 peak intensities . The calculated volume fraction of the W disappearing in the 20 nm thick W layer sandwiched between two HfO_2 layers is estimated to be 79% at the end of the 6 h isothermal stage at 1520 °C, which means most of the metallic layer is gone.

Important microstructural information like grain size is as well contained in the broadening of x-ray diffraction peaks [107]. The grain size values in growth direction are calculated using the Scherrer formula. Figure 3.27 (A

and B) shows the grain size value of bcc W during the heating ramp and isothermal stage at 650 °C (blue markers) and 1520 °C (red markers). The average grain size of W in the 3-layer-system before annealing is 14 nm.

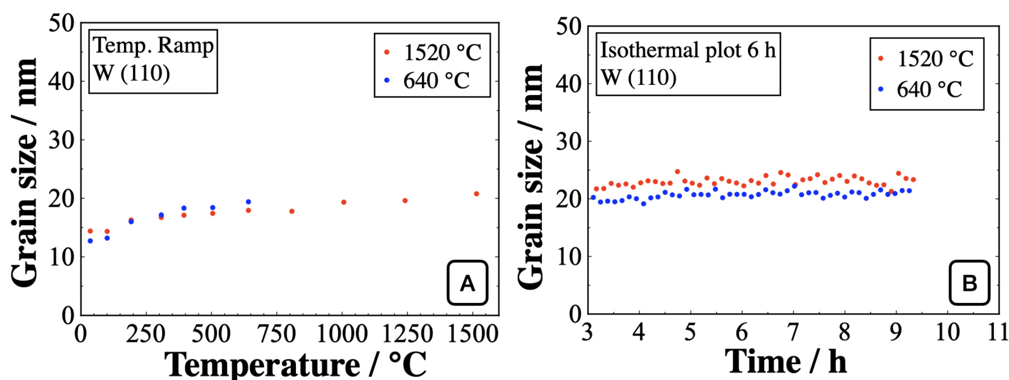

Figure 3.27: Determined grain size values using the (110) bcc W peak (A) as a function of temperature during annealing ramp, and (B) as a function of time during isothermal annealing of the 3-layer-systems annealed for 6 h at 650 °C (blue markers) and 1520 °C (red markers) at 3×10^{-6} mbar.

Gradual grain growth behavior is observed for both the 3-layer-system during the annealing ramp. On reaching the isothermal regime, the grain size stabilizes close to the layer thickness. The grain size measured by x-ray diffraction is in the out of the plane direction. The grain size at the end of the annealing experiment for the sample annealed at 650 °C is 21 nm and 1520 °C is 23 nm.

The grain size information of monoclinic HfO_2 during heating ramp and isothermal stages at 650 °C (blue markers) and 1520 °C (red markers) are shown in Figure 3.28 A and B. Before the annealing process the calculated grain size value is about 18 nm. During annealing at 650 °C, the grain size

gradually increases over the time of 6 h and reaches a maximum value of 22 nm. In the sample annealed at 1520 °C for 6 h, two stages of grain growth are seen.

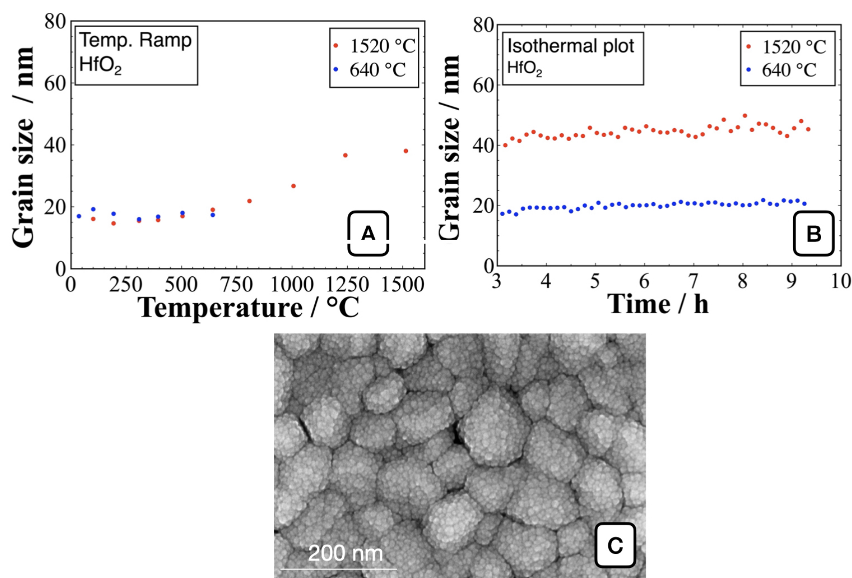

Figure 3.28: Determined grain size values of (-111) monoclinic HfO_2 peak (A) as a function of temperature during annealing ramp, and (B) as a function of time during isothermal annealing of the 3-layer-systems annealed for 6 h at 650 °C (blue markers) and 1520 °C (red markers) at 3×10^{-6} mbar.(C) A SEM picture of the top HfO_2 layer of a 3-layer-system after annealing it at 1520 °C for 6 h, shows the grain size in the in-plane direction having an average grain size value of 75 nm.

During the ramp part of the annealing, a distinct increase in the grain sizes of the monoclinic phase by a factor of two is visible, finally reaching a value up to 40 nm. The temperature dependent process of grain growth is driven by the annealing temperature, but reaches a plateau during the isothermal part of the experiment . During the 6 h at 1520 °C, the HfO_2

grains grow further slightly to reach a maximum value of about 45 nm. Figure 3.28 (C) shows a SEM image of the grain size of the top HfO_2 layer in a 3-layer-system after annealing it at 1520 °C for 6 h. The grains reach an average value of 75 nm in the in-plane direction.

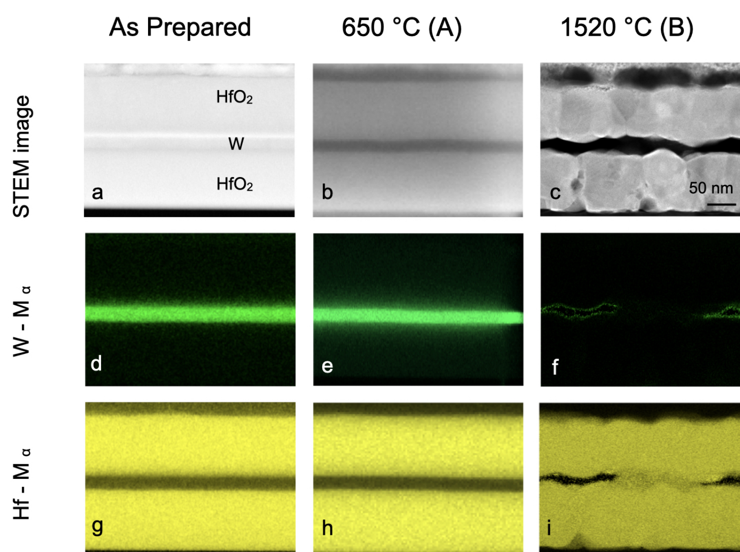

Figure 3.29: STEM-EDS analysis of the 3-layer-system, as-prepared, annealed at 650 °C and 1520 °C for 6 h at 2 × 10^{-6} mbar. STEM-HAADF images (a-c), W-M_α elemental mapping (d-f), Hf-M_α elemental mapping (g-i). These images have the same scale as indicated in image (c).

In order to obtain a deeper understanding on the structural changes in W and HfO_2 layers during the annealing experiments, TEM-EDS characterizations on the as-prepared and annealed samples were performed. The STEM-high-angle annular dark-field (STEM-HAADF) image and the elemental mapping (Figure 3.29 a, d, and g) of the as-prepared sample show a clearly distinguishable 3-layer-system. After 650 °C, there are no noticeable

changes in the layer stack (Figure 3.29 b, e, and h), the interface between W and HfO_2 layers appears to be unaltered. No grain boundaries were seen in the studied TEM lamella.

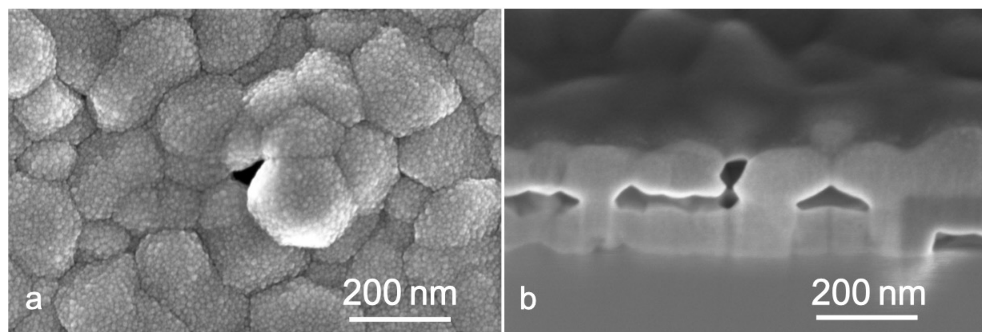

Figure 3.30: (a) Morphology of the top HfO_2 layer with a void in the middle and (b) Cross section view along the interfaces across the same void (FIB section) after annealing it at 1520 °C for 40 h, at 3×10^{-6} mbar vacuum pressure.

On the contrary, after annealing the sample at 1520 °C for 6 h, drastic changes in morphology occur (Figure 3.29 c). An increase in the interface roughness of the HfO_2 layers is clearly visible and the interface becomes wavy in contrast to the sharp interfaces prior to annealing. Individual grains are clearly seen with distinct grain boundaries due to the increase in grain size. The EDS mapping of W (Figure 3.29 f) shows a very weak presence of W in the layer, which corroborates the XRD results indicating the reduction of W volume fraction (Figure.3.26 b) after annealing at 1520 °C. In addition, the EDS mapping of Hf (Figure 3.29 i) after annealing at 1520 °C for 6 h confirms the presence of Hf in the HfO_2 layer and no intermixing of W and

Hf.

In order to investigate the disappearance of W in the 3-layer-system, a further annealing experiments was performed for 40 h at 1520 °C. The idea behind the experiment was to calculate the time required for all the W in the 3-layer-system to totally vanish and later study the remaining morphology. Figure 3.30 (a,b) shows the top view and cross section SEM images of the 3-layer-system annealed at 1520 °C for 40 h. The top HfO_2 layer contains voids between the grains. In the 3-layer-system, the voids extend throughout the first HfO_2 layer, this is confirmed in the cross section view Figure 3.30 b done by FIB. The picture clearly demonstrated the complete loss of W in the 3-layer-system. The residual oxygen present in the chamber approach the W through the voids, resulting in oxidation and the formation of volatile WO_x [108] .Therefore the voids act as an effective transport channel. From the in-situ measurement, the calculated time required for complete disappearance of W is estimated to be 20 h. It is also important to note that the volatile WO_x sublimates rapidly at 1520 °C, and leaves the 3-layer-system through the same transport channels. As a consequence, no WO_x peaks are visible in the diffractograms. To cross check the sublimation of WO_x, a plain sapphire "witness" substrate was therefore placed on the wall of the heating chamber close to the outlet of the vacuum pump. The chamber wall is circulated by cooling water and therefore the sapphire substrate is comparatively at a very low temperature compared to the 3-layer-system. The distance between both is approximately 10 mm. The sublimated WO_x was redeposited on the

witness substrate. A diffractogram (Figure 3.31) of the witness sample shows presence of WO_2 and small quantities of $WO_{2.7}$ and W. A quantitative phase analysis results in a ratio of 90%: 5%: 5%. A reduction of the volatile WO_2 and $WO_{2.7}$ to W is also observed by Lou et al.[109] in their nonstructural fabrication of WO_x by hot filament chemical vapor deposition.

A diffractogram of the witness sample shows presence of WO_2.

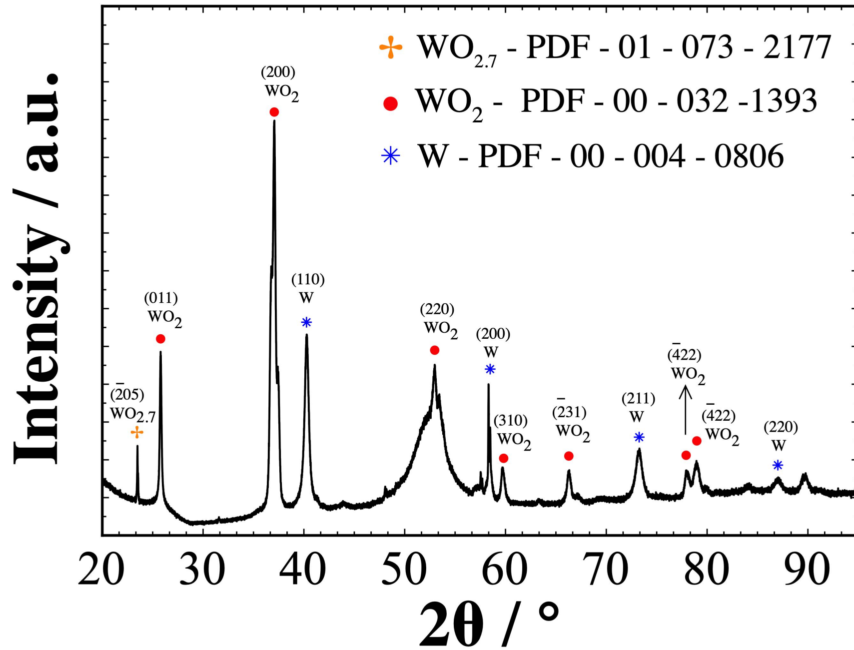

Figure 3.31: XRD diffractogram of the vaporized constituents collected on a sapphire substrate in the chamber during the 40 h annealing experiment at 1520 °C, 3 × 10^{-6} mbar.

The possibility of W obtaining O_2 from HfO_2 can be excluded, as this reduction reaction would either result in pure Hf formation or sub-stoichiometric HfO_2. No Hf peaks are observed in any of our in-situ X-ray diffraction ex-

periments. In addition, the 3-layer-systems were investigated by means of Rutherford Backscattering (RBS) (Figure 3.32) after preparation and after annealing at 650 °C (blue markers) and 1520 °C (red markers).

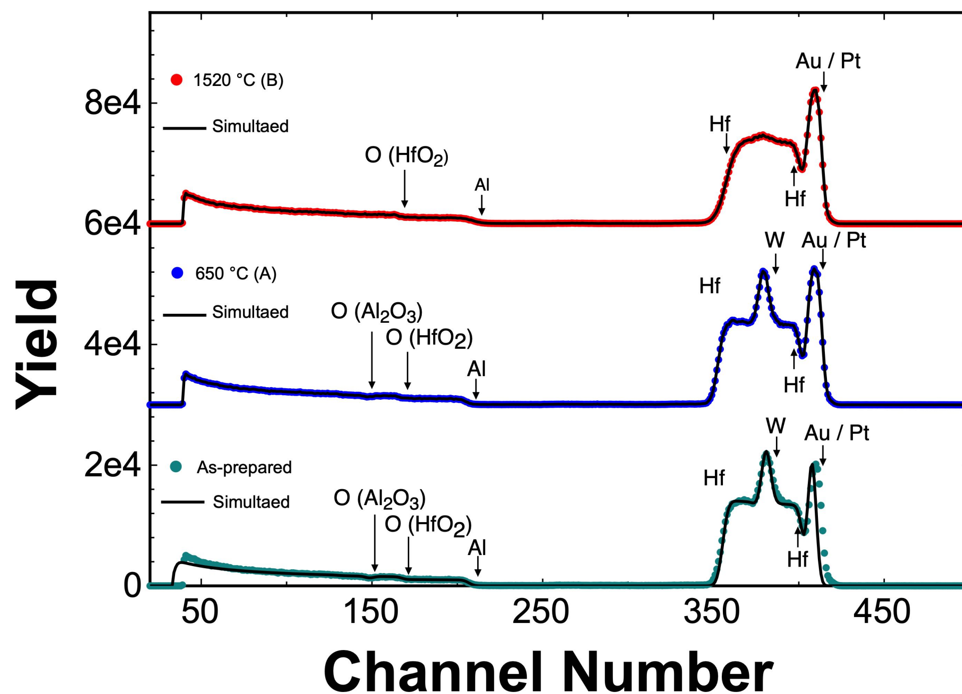

Figure 3.32: RBS spectra of the 3-layer-system as-prepared (green markers), annealed at 650 °C (blue markers), and 1520 °C (red markers).

All samples were covered with Au and Pt for latter TEM investigations. For the chemical analysis, a 2 MeV He-ion beam with a beam current of 20 nA and a detector back scattering angle of 160° was employed. The sensitivity of depth profiling was improved by changing the incidence angle from 7° to 45° (not shown here) in order to determine if the signals originate from surface or underlying layers. At high energies, right side of the figure,

the heavy elements are well separated. First, the Au/Pt signal from the additional layers for TEM preparation. Then, the Hf edge from the top layer, W from the second layer and again Hf from the third layer are clearly visible. After a large gap of no signal, the signals of the light elements like Al and O are detected at low energies. It is important to notice the sharp edge at channel 385 for the as-prepared sample that indicates the presence of W in the film. There is no modification due to annealing at 650 °C after 6 h. But, after 1520 °C, the shoulder at channel 385 vanishes, which confirms the strong loss of W. About 75% of the HfO_2-sandwiched W layer is gone. Additionally, the stoichiometry of HfO_2 was estimated to be slightly over-stochiometric ($HfO_{2.4}$) for the sample annealed at 1520 °C using simulations. This result is of importance, as it validates that there is no reduction of oxygen in the HfO_2 layer, therefore most likely W does not get the O_2 from HfO_2 layer, but from the residual oxygen in the annealing chamber.

A vast source of literature is available on the oxidation process of W [110], [111], [112], [113], [114], [115], [116], [117],[118]. W is the only metal for which oxidation rates have been measured above 2000 °C. The stable oxides of W found in literature are WO_2, $W_{18}O_{49}$, $W_{20}O_{58}$, $WO_{2.96}$ and WO_3. In general, based on the partial pressure of O_2 and temperature according to published data, the oxidation process can be subdivided into four zones as shown in Figure 3.33.

Zone 1: In the first zone, the temperature range is between 25 °C - 500 °C, and the partial pressure of O_2 was kept higher than 100 mbar [110]. On

annealing W in this setup, an increase in mass of the sample was recorded. The increase in mass is due to formation of an oxide layer on the top surface of the sample and follows a parabolic rate. As the initially formed oxide layer acts as a passivating layer, the rate of oxidation reduces as time proceeds. It is important to note that oxidation of W to form WO_x is an exothermic process followed by the liberation of heat. The reaction has a negative enthalpy of formation [102], is diffusion controlled and has an activation energy of 1.92 eV .

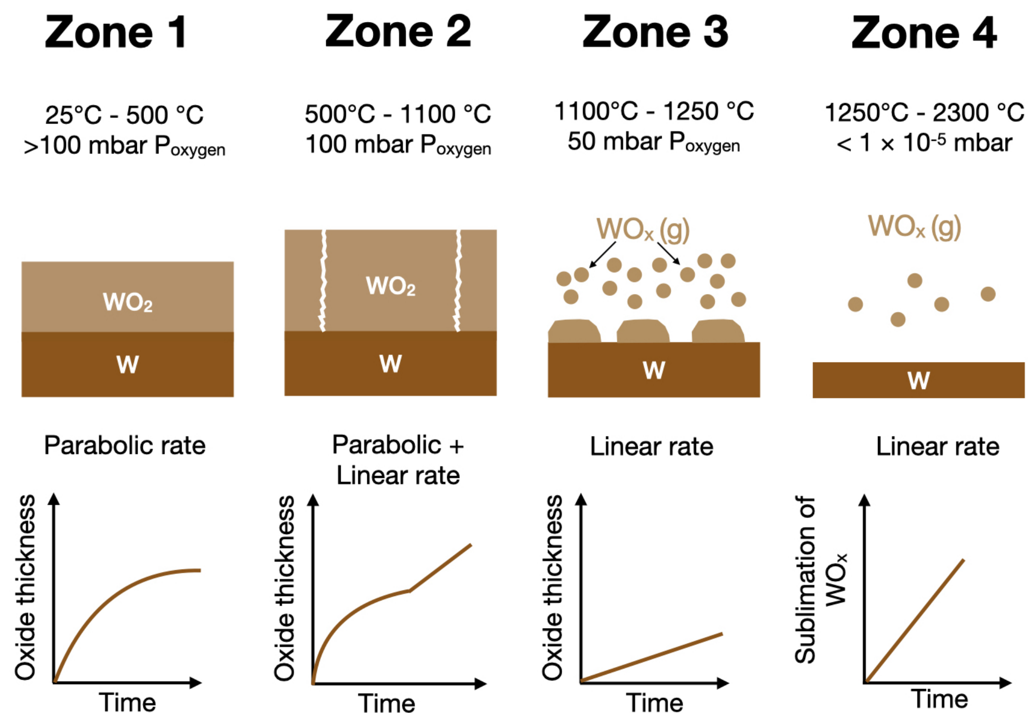

Figure 3.33: Schematic explaining the oxidation mechanism of W at various temperature and pressure ranges.

Zone 2: In the second zone, the temperature range is between 500 °C -

1100 °C, and the partial pressure of O_2 was maintained at 100 mbar [111]. Complete oxidation of W occurs at the experimental conditions. Two different kinetics are observed, initially oxidation proceeds by diffusion of oxygen through the already existing oxide layer and has parabolic rate behavior. Later, the parabolic rate transforms to a linear rate, as the oxide layer cracks under the influence of stress and exposes a fresh metal surface below. The activation energy required for oxidation in the second zone is 1.4 eV [111].

Zone 3: In the third zone, the temperature range is between 1100 °C - 1250 °C, and the partial pressure of O_2 was maintained at 50 mbar. In this case, all the available O_2 reacts with W to form volatile WO_3. As the rate of sublimation is faster than the rate of oxide layer formation, no oxide layer on the top of the surface is visible. In our annealing experiments [41] discussed in Section 3.3.2, annealing of a metamaterial at 1200 °C and in a vacuum of 2×10^{-2} mbar, WO_2 peak is clearly visible in the diffractograms shown in Figure 3.12, above this temperature and at a still lower pressure no oxide peaks are found.

Zone 4: In the third zone, the temperature range is between 1250 °C - 2300 °C, and the vacuum pressure is less than 1×10^{-5} mbar. At these annealing conditions, only weight loss is recorded in the W sample. As the number of O_2 atoms present is small, the formation of an oxide layer is not witnessed. The activation energy for oxidation of W in the fourth zone lies between 0.6 eV to 0.86 eV [113].

In all the in-situ annealing experiments performed on 3-layer-system, the

pressure was maintained below 2×10^{-6} mbar. Therefore no WO_x peaks were recorded in any of the diffractograms during the entire annealing cycle. Figure 3.30 reveals the presence of voids on the top HfO_2 layer. In order to determine the temperature range at which the voids are formed, further annealing experiments were done for a duration of 20 h at different temperatures between 650 °C and 1520 °C.

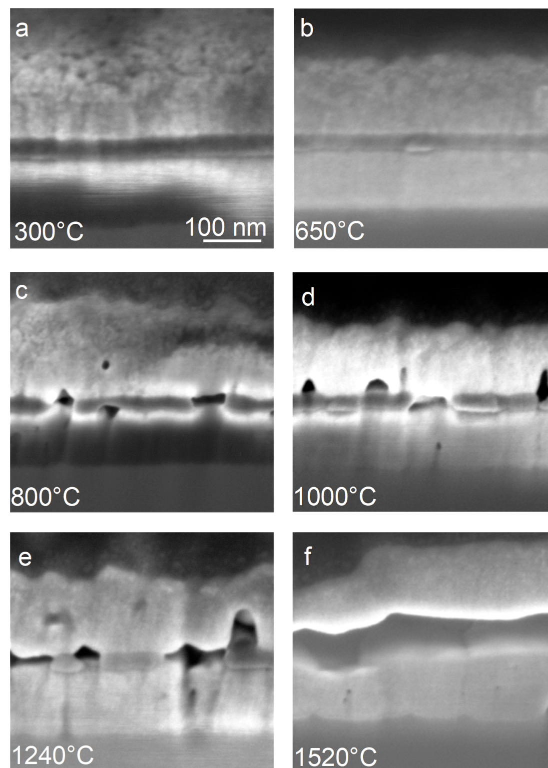

Figure 3.34: SEM cross section of the 3-layer-system annealed at different temperatures for a period of 20 h. a) 300 °C, b) 650 °C, c) 800 °C, d) 1000 °C, e) 1240 °C, and f) 1520 °C. All the images have the same scale as indicated in image (a).

It is visible in the SEM images (Figure 3.34) that voids are present in all samples annealed above 800 °C. This is exactly the temperature at which the tetragonal phase of HfO_2 completely transforms into the monoclinic phase. A change in structure from tetragonal to monoclinic results in a volume increase accompanied by shear strain Wang et al. [44]. It is also to be noted that the symmetry of the structure is reduced from tetragonal ($a = b \neq c$, $\beta = 90°$) to monoclinic ($a \neq b \neq c$, $\beta \neq 90°$). This results in anisotropic behavior of thermal expansion, where the minimum and maximum thermal expansion values do not lie in the lattice directions for a monoclinic structure. The coefficient of thermal expansion for the monoclinic phase of HfO_2 ranges between 8×10^{-6} K^{-1} at room temperature to 32×10^{-6} K^{-1} at 1750 °C [119]. Therefore, the tetragonal-to-monoclinic phase transformation in HfO_2 and the anisotropic nature of the monoclinic phase results in the formation of voids between the HfO_2 grains in the top HfO_2 layer.

In order to access the temporal changes in the W layer during the in-situ annealing experiments, the integrated intensity of (110) W peak, for all the 3-layer-systems annealed for 20 h at 800 °C, 1000 °C, 1240 °C and 1520 °C is shown in Figure 3.35 (A). For the sample annealed at 800 °C there is a slight decrease in intensity after 18 h. A noticeable drop in intensity is visible for the sample annealed at 1000 °C and 1240 °C. In the case of 1520 °C, initially there is a drastic drop in intensity for the first 3 h and later the rate of intensity drop is reduced. It also to be noted that the for the sample annealed at 1520 °C, grain size increase and volume loss already starts during

the temperature ramp above 1240 °C and coupled with a higher temperature ramp of 120 °C/min causes a earlier change in the volume fraction.

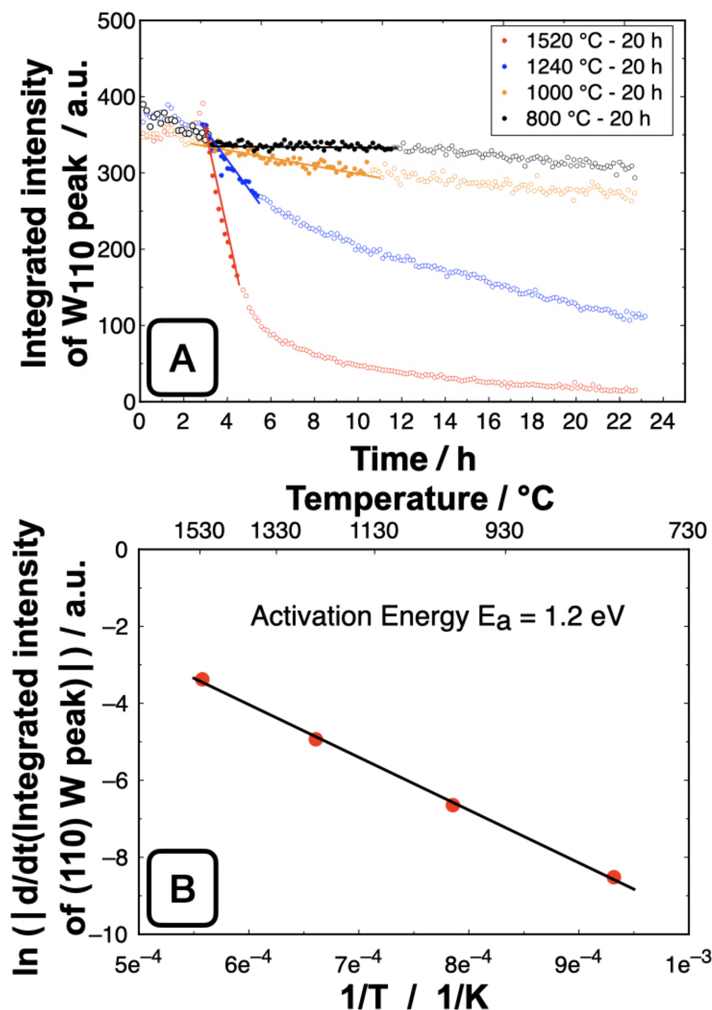

Figure 3.35: (A) Integrated intenstiy of (110)W peak in the 3-layer-system during isothermal annealing at 800 °C, 1000 °C, 1240 °C and 1520 °C for 20 h at 3×10^{-6} mbar vacuum pressure. The data point represented in filled dots are used for linear regression, the hollow dots are the remaining data points. (B) The change in volume fraction of W is represented as an Arrhenius plot used to calculate an activation energy of 1.2 eV for the oxidation process.

For each temperature, a linear fit is performed for the first segment (filled circles) and the respective slopes are calculated. The filled circles represent the volume fraction of W directly under the transport channels in the HfO_2 layer. The unfilled circles represent the volume fraction of W not present directly under the transport channels. Therefore, the oxygen molecules have to traverse in a lateral direction to reach the W atoms, which cause a change in sublimation rate. Distinctly, the change of volume fraction in the W layer, in the 3-layer-system can be estimated from the calculated slopes. The change in volume fraction is a thermally activated process and it can be represented by an Arrhenius plot (Figure 3.35(B)). An activation energy of 1.2 eV is calculated for O_2 to penetrate through the transport channels, oxidize the W and sublimate as volatile WO_x. Similar activation energy of 1.1 eV was calculated by Becker et al. [114]. The rate of W disappearing from the 3-layer-system can also depend on the number and size of voids present in the top HfO_2 layer. Increasing the temperature further can produce wider transport channels and further accelerate the sublimation of volatile WO_x. Therefore, the obtained activation energy can be alternatively linked to surface diffusion of HfO_2 that leads to grain growth and void formation.

To summarize the important results of the 3-layer-system a schematic is presented in Figure 3.36. In the as-prepared 3-layer-system (20 nm W layer, sandwiched between two 100 nm HfO_2 layers) the HfO_2 layers shown in Figure 3.36(a) contain 56 % monoclinic phase and 44% amophous phase. (b) On heating the sample between 160 °C and 200 °C, the amorphous phase

first transforms into the tetragonal phase. (c) On further heating above 800 °C, the tetragonal phase transforms into the stable monoclinic phase. This phase transformation results in a volume increase of the unit cell by 3.5%. As a result, voids are generated in the HfO_2 layers. (d) On further reaching higher temperatures above 1000 °C, the voids in the HfO_2 layer grow and form transport channels paving way for the oxygen in the annealing chamber to reach the W layer. As a consequence the W layer gets oxidized and forms volatile oxides that sublimate rapidly.

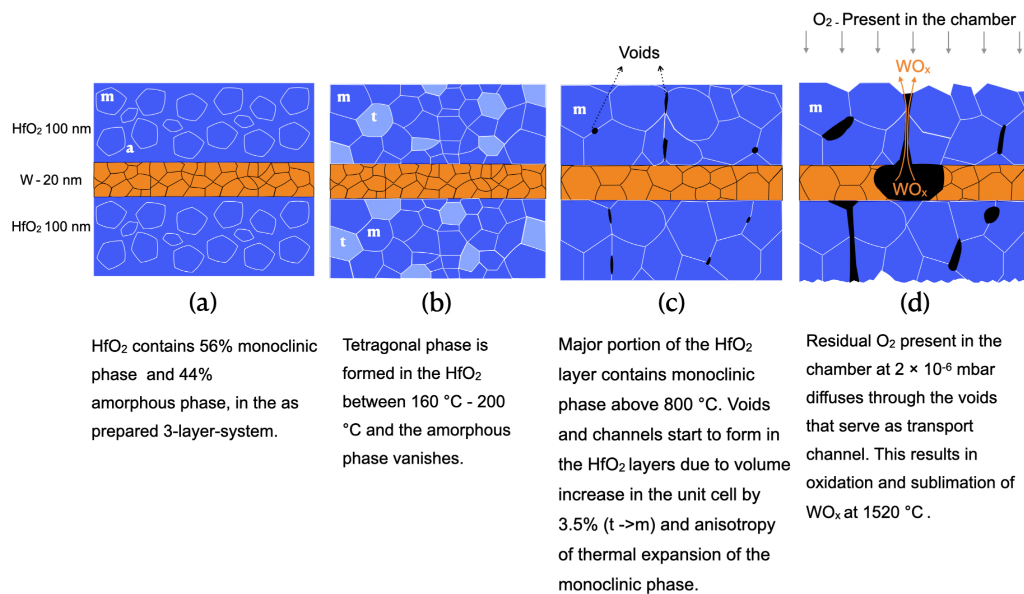

Figure 3.36: Mechanisms during annealing of a 3-layer-system up to 1520 °C: phase transformation and channel formation in the HfO_2 layers and the loss of W due to oxidation through the transport channels.

Chapter 4

Iridium - Hafnia selective emitter

4.1 Properties and morphology of iridium thin films

Iridium (Ir) is a noble metal and has the atomic number 77. It belongs to transition metals, lies in group 6 of the periodic table, and is a member of the platinum group. Ir has a melting point of 2443 °C [120], a low vapor pressure of 1×10^{-8} mbar at 1763 °C [121], and is the second most dense element 22.56 g cm^{-3}, after Os. The electronic configuration of Ir is [Xe] $4f^{14}5d^{7}6s^{2}$. The shape of the d-orbitals influences the properties of Ir. In the d-subshell, azimuthal quantum number $l = 2$ and magnetic quantum number m has five values -2,-1, 0, 1, 2, indicating the d-orbitals have five

orientations, that are named as $d_{xy}, d_{yz}, d_{zx}, d_{z^2}$ and $d_{x^2y^2}$, as shown in the Figure 4.1 . The d_{xy}, d_{yz}, and d_{zx}orbitals have cloverleaf shapes. The $d_{x^2y^2}$, is also cloverleaf shaped, but its leaves are directed along the x and y-axis. The d_{z^2} orbital is symmetrical about the z-axis and has a dumbbell shape with a doughnut electron cloud in the center. The lobes of two d-orbitals on the same atom occupy different regions. Therefore electrons in different d-orbitals are relatively far apart and repel one another only weakly. The total number of nodes present in the d-orbital is 4. At a node, the probability of finding an electron is zero. Hence the electron density in d-orbitals is low near the nucleus and is not very effective in shielding the valence electrons in the f-orbitals. As a consequence, the valence electrons are tightly bound and are not easily available for reaction [122].

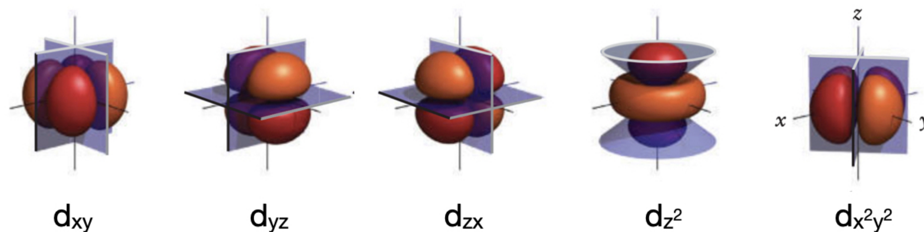

Figure 4.1: Shape of d-orbitals showing the presence of nodes [122].

Ir also has a very low O_2 permeability 10^{-14}g cm^{-1} s^{-1}[123] and good oxidation resistance. The Gibbs energy of formation [102] ΔG_f, for the formation of IrO_2 is ΔG_f= -18.8 kJ mol $^{-1}$ compared to the formation of $WO_{2.7}$

is ΔG_f= -477.9 kJ mol $^{-1}$ at 1000 °C and 1 bar pressure, is shown in Figure 4.2, as IrO_3 exists only in gas phase it is not shown in the latter figure. The comparison shows the ΔG_f is more negative for $WO_{2.7}$ for the entire range shown. The more negative the ΔG_f is the more stable will be the formed oxide. It is also observed as the temperature increases ΔG_f of IrO_2 approaches zero, in other words the formation of IrO_2 will not be thermodynamically favorable.

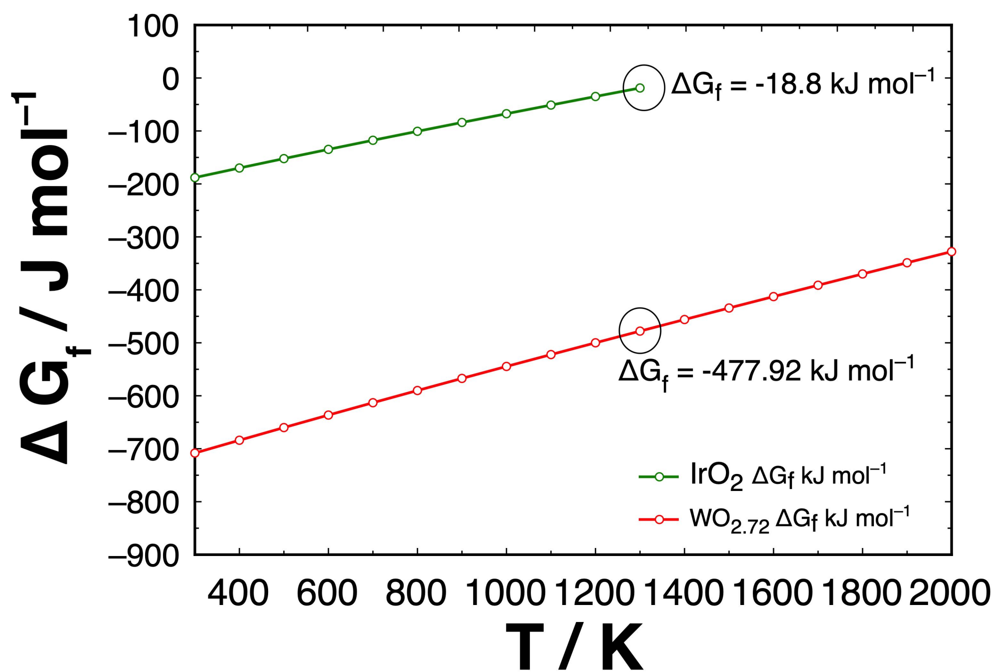

Figure 4.2: Comparison of ΔG_f as a function of temperature between IrO_2 and $WO_{2.7}$.

The stable solid oxide of Ir is IrO_2, whereas IrO_3 is gaseous [124]. The

oxidation rate of Ir also depends on the partial pressure of O_2 present in the chamber. There exists literature [125], [126], [127], [128], [129], [123] on various annealing experiments performed on Ir at different pressures and temperature ranges between 1000 °C - 2000 °C, and most of the experiments were performed on bulk Ir material. Annealing studies performed on thin films above 600 °C, 1 bar show the formation of IrO_2 on the surface [130], [131], [132]. On further heating it to 700 °C in O_2 rich environment, IrO_2 transforms to IrO_3, which is a gas that sublimates immediately leaving behind a clean metal surface as shown in Figure 4.3.

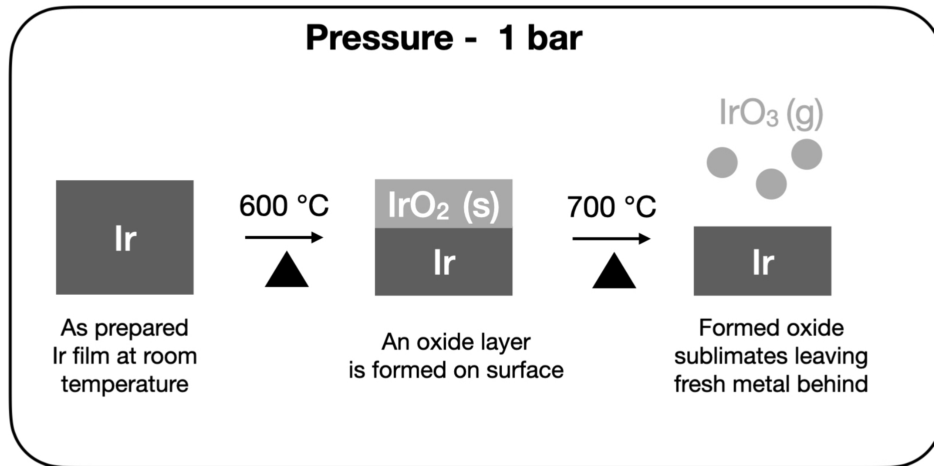

Figure 4.3: As prepared Ir films first forms an oxide (IrO_2 (s))layer above 600 °C, on further heating above 700 ° C the formed oxide sublimates (IrO_3 (g)) leaving fresh metal behind at 1 bar pressure.

In this chapter, in-situ x-ray diffraction experiments are initially performed on a 3-layer-system (HfO_2 100 nm / Ir 30 nm / HfO_2 100 nm/ sapphire) (Figure 4.4) to investigate structural and microstructural changes of

a single Ir layer. The primary goal of these experiments are to determine the temperature at which the 3-layer-system remains thermally stable without undergoing any structural changes and chemical reactions between layers or with the residual gas present in the vacuum chamber. Annealing experiments were also performed on a bilayer (Ir 30 nm / HfO_2 100 nm / sapphire)(Figure 4.4) to study the leaving out of a top protective HfO_2 layer. Later, a multi-layered metamaterial selective emitter (capping layer - HfO_2 100 nm / 6 $\times$ (Ir 30 nm / HfO_2 100 nm) / sapphire) is fabricated and tested at 1000 °C for 100 h at 2×10^{-6} mbar to validate the durability for TPV applications. Even though, experiments were performed at temperatures close to 1520 °C in the previous chapter, the following are the reasons to validate durability at 1000 °C:

- Tungsten based selective emitters show thermal stability up to 1400 °C for 6 h, but when subjected to durability test at 1000 °C for 20 h in a 3-layer-system, sublimation of tungsten is observed.
- A good selective emitter should work effectively in a practical environment (approximately 2×10^{-2} mbar vacuum pressure) for a longer duration (test conditions approximately 100 h) at an acceptable temperature of atleast 1000 °C.

The 3-layer-system, bilayer, and multilayered metamaterial are prepared by magnetron sputtering. The chemical composition of the multilayered metamaterial before and after annealing are determined by Scanning Trans-

mission Electron Microscopy- combined with Energy Dispersive X-ray Spectroscopy (STEM-EDS).

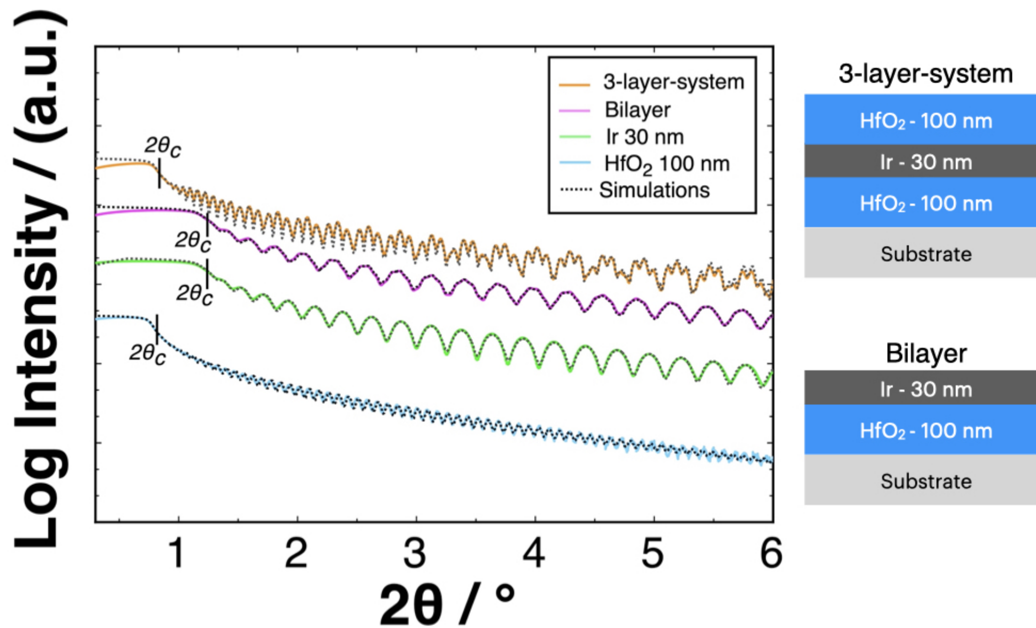

Figure 4.4: Measured and simulated x-ray reflectivity (XRR) as a function of the scattering angle 2θ of as-prepared single 100 nm thick HfO_2 layer (blue), single 30 nm thick Ir layer (green), bilayer (30 nm Ir/100 nm HfO_2) (magenta), a 3-layer-system (100 nm HfO_2 / 30 nm Ir/100 nm HfO_2) (orange) prepared on a silicon substrate and each combination is simulated (dotted lines). On the right to the scans, schematics of a bilayer and 3-layer-system are shown.

In thin films prepared by magnetron sputtering, the surface and interface of a single layer and the multilayer have a variation in surface morphologies related to the growth mechanisms [60]. The thickness, roughness and density of two single layers metallic Ir and dielectric HfO_2, a bilayer (30 nm Ir / 100 nm HfO_2), and a 3-layer-system (100 nm HfO_2/ 30 nm Ir / 100 nm HfO_2)

were determined using XRR (Figure 4.4). All four scans were investigated with Cu radiation ($\lambda = 0.15406$ nm) and measured with a grazing incidence angle of 2θ between 0 ° and 6 °.

The shift in double critical angle $2\theta_c$ is a direct indication of variations in the mean overall density of the sputtered films. In the case of a single HfO_2 layer 100 nm thick, $2\theta_c$ is below 1 °, whereas in the single Ir layer 30 nm, the $2\theta_c$ is greater than 1 ° indicating a higher density . Adding Ir over HfO_2 in the bilayer does not have an impact on the double critical angle $2\theta_c$. However, when a HfO_2 layer is deposited over Ir in the 3-layer-system, the critical angle $2\theta_c$ is shifted to lower values. The simulated thickness, roughness and density of a single Ir and HfO_2 layer is shown in the Table 4.1.

Layer	Aim / nm	Thickness / nm	Roughness / nm	Density / g cm^{-3}
Ir	30	30.4 (0.5)	0.25	22.3
HfO_2	100	100.1 (0.5)	0.27	9.4

Table 4.1: Simulated XRR thickness and roughness of 30 nm Ir and 100 nm HfO_2 films. The experimental error of thickness determination is ± 0.5 nm.

4.2 Thermal stability of Ir as a function of temperature and time

In high-temperature materials research, basic phenomena like phase transformation, reaction kinetics, and mass transport are of primary interests.

Therefore, it is essential to determine the crystal structure, investigate the phase transition, and to verify the chemical reactions of the thin-film material in a 3-layer-system. Based on the latter acquired knowledge, improving a multilayered metamaterial for long-term TPV applications is an achievable goal. In-situ x-ray diffraction serves as an appropriate characterization technique by recording sequential diffraction patterns under controlled heating rates and at distinct vacuum pressures as a function of time and temperature, which helps us to investigate the thermal and temporal modification in the samples.

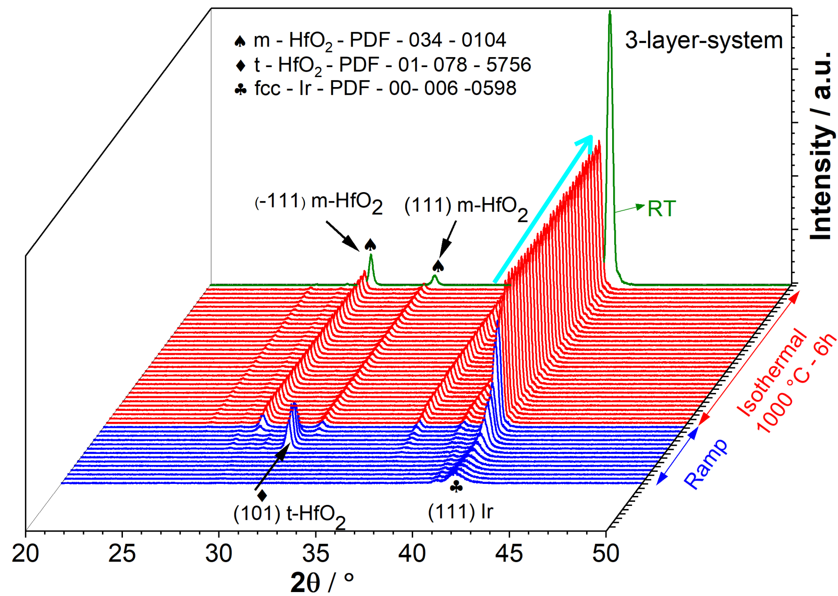

Figure 4.5: In-situ XRD diffractograms of a 3-layer-system from room temperature up to 1000 °C represented in blue. Diffractograms in red represent isothermal annealing at 1000 °C for 6 h. The last scans in green is measured at room temperature at the end of the annealing experiment. The annealing experiment is performed in a vacuum pressure of 2 × 10^{-6} mbar.

A waterfall plot of a 3-layer-system annealed at 1000 °C for 6 h at 3×10^{-6} mbar is shown in Figure 4.5. The reason for not investigating thermal stability above 1000 °C is discussed in detail under grain size analysis of Ir. The diffractograms in blue shows the temperature ramp at the beginning from room temperature until 1000 °C. In the as-prepared 3-layer-system, no dominant peaks are visible from the HfO_2 layer measured at room temperature (first blue scan). For clarification the relevant angular range (20° - 38°) is enlarged in Figure 4.6. The HfO_2 layer consist of two phases: 90 % is amorphous and 10 % is monoclinic phase. The crystallinity is altered compared to W/HfO_2 3-layer-system (see previous Section 3.4), since the impurity level of Zr in this case is lower (< 2000 ppm), therefore the formation of the amorphous phase is favored [133], [134]. The prominent (111) peak at 40.3° belongs to the fcc phase of Ir. On further ramping up the temperature, HfO_2 undergoes polymorphic phase transformation [58]. The amorphous phase initially transforms at 200 °C to a metastable tetragonal phase indicated by (101) reflection at 30.3° in Figure 4.5. Above 800 °C, the tetragonal phase of HfO_2 transforms into the thermodynamically stable monoclinic phase of HfO_2 with some new x-ray peaks, which are indexed by (-111), (111), and (-210). Compared to HfO_2, no phase changes are visible in the Ir layer. The peak at 36.6° is due to Cu-K_β radiation from the (111) Ir peak. However, there is a gradual increase in the intensity of the (111) peak during the temperature ramp.

Later, in the isothermal part (red scans) of the annealing experiment at

1000 °C for 6 h, the peak intensity of HfO_2 is constant, which confirms the good condition of this refractory thin-film material. The (111) peak intensity of fcc Ir in the 3-layer-system is also stable and indicated by a turquoise arrow.

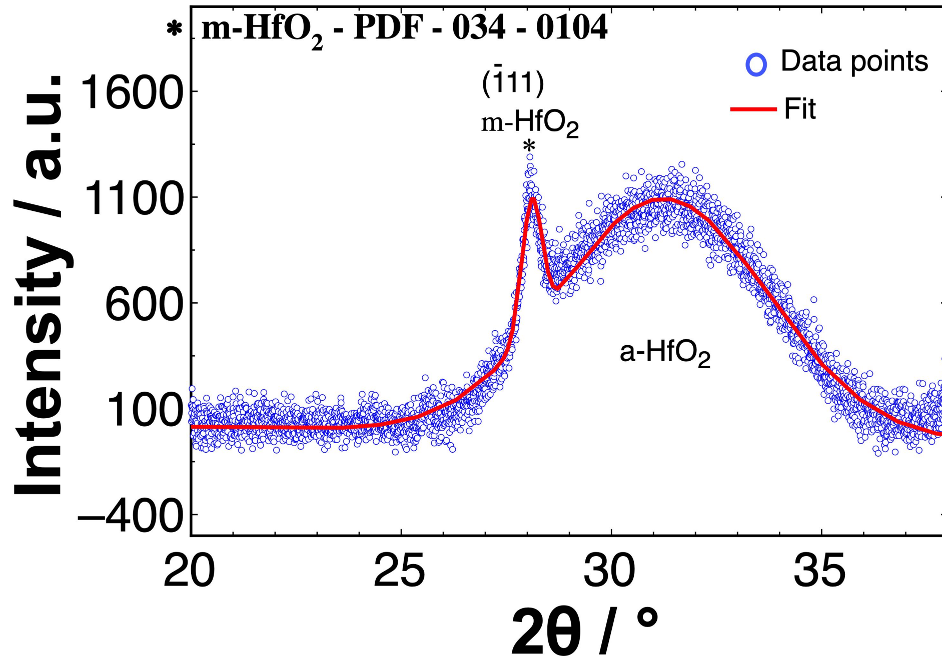

Figure 4.6: X-ray diffractogram of a 3-layer-system between 20° - 38° after preparation. The (-111) peak at 28° belongs to the monoclinic phase and the broad bump at 31° belongs to the amorphous phase of HfO_2.

No new peaks emerge in the isothermal annealing, confirming neither oxidation of the Ir layer, nor any possible reactions between Ir and HfO_2, and absence of any chemical reaction between the bottom HfO_2 layers and the sapphire substrate. It is also worthwhile to compare the peak integral of (111) fcc Ir before and after annealing at room temperature. The area under the peak before annealing is small as a result of reduced grain size around 12

nm, higher grain boundary volume and higher defect concentration due to sputtering, whereas after annealing the area is increased due to higher grain size, reduced grain boundary volume and reduced defect density that results in a more defect-free microstructure within the Ir layer.

The last scan in the waterfall plot, in the sample highlighted in green for the 3-layer-system, is recorded at room temperature after the cooling cycle. The shift in peak position to higher angles is due to thermal contraction. After closer examination, the peak height increase of 54% of the last scan at room temperature is understood. It is well known that atoms undergo thermal vibration from their mean position, and the amplitude of vibration is enhanced with the increase in temperature [63]. The average displacement is in the order of the separation between electrons within an atom and should have the same effect as scattering, namely, destructive interference increases with increasing scattering angle 2θ and temperature-diffused scattering will increase the background and decrease the Bragg peaks. The loss in intensity [63] can be calculated using the temperature factor e^{-2M} in the atomic scattering factor f,

$$f^2 = f_0^2 \, e^{-2M} \tag{4.1}$$

Where,

M = temperature factor

f_0 = atomic scattering factor

The value of M can be theoretically determined using Debye's expression

$$M = \frac{6\,h^2\,T}{m\,k\,\Theta^2}\left[\phi(x) + \frac{x}{4}\right]\left(\frac{\mathrm{Sin}\theta}{\lambda}\right) \tag{4.2}$$

Where,

h = Planck's constant

T = absolute temperature

m= mass of Ir atom

k = Boltzmann constant

Θ = Debye characteristic temperature, for Ir 285 K

$x = \frac{\Theta}{T}$

$\phi(x)$ = 0.951 (tabulated value)

θ = Bragg angle

λ = wavelength of X-ray used

Substituting the above values in equation 4.1 and 4.2, the calculated atomic scattering factor results in 55%, which is in good agreement with the experimental results.

The impact of annealing on the interplanar spacing d_{111} of Ir in the 3-layer-system annealed at four different temperatures as a function of temperature during temperature ramp and time during isothermal annealing is

shown in Figure 4.7. The room temperature d-values of the 3-layer-system is 0.2233 nm.

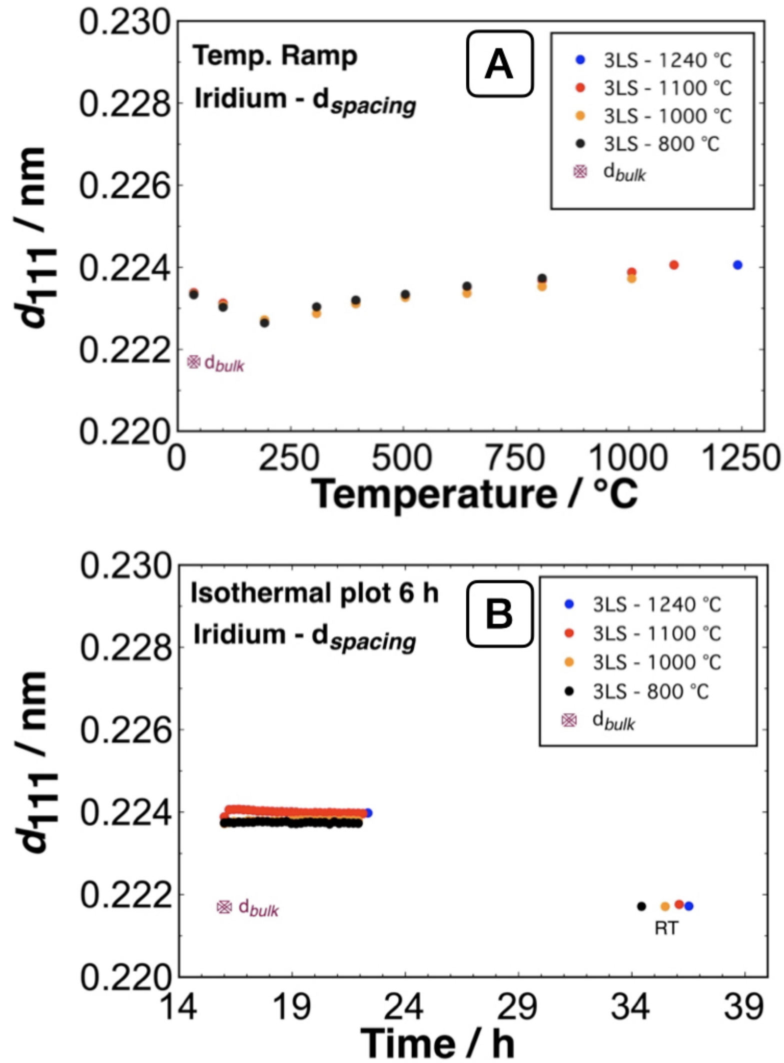

Figure 4.7: Measured interplanar spacings d_{111} fcc Ir as a function of temperature during annealing ramp (A) and as a function of time during isothermal annealing (B) in the 3-layer-system. After 24 h, slow cool-down transfers the samples back to room temperature (RT).

At the start of the annealing process during the temperature ramp, initially, there is a drop in the d-value (first 3 points) that is a result of the relaxation of stress generated during the sputtering process by atomic peening. On further increasing the temperature, there is a gradual rise in the d-spacing due to thermal expansion. Later during the isothermal annealing, the interplanar spacing reaches an equilibrium value at the respective temperature and remains mostly unaltered.

On cooling back to room temperature, after a total of more than 30 h the *d*-spacing reach the tabled equilibrium value of bulk Ir that is 0.2217 nm. The magnetron sputtered Ir layer in the 3-layer-system is nanocrystalline in nature. A reduction to nanometer regime leads to more interfaces such as grain boundaries, this means that a relevant fraction of atoms is at the interfaces. One of the important attribute of a nanocrystalline materials is, the major portion of their atoms residing in the grain boundaries, for e.g. in a nanophase material with 5 nm average grain size will have from about 40% of its atoms residing in the grain boundaries. The percentage falls 20% for a 10 nm grain size, but is as low as 2% for a 100 nm grain size [135].

Nanocrystalline materials are virtually always different in their physical, chemical or mechanical properties in comparison to coarse-grained bulk materials. Several preparation methods, especially physical vapor deposition of thin films, are available for the controlled synthesis of nanocrystalline materials, and it is worthwhile to mention that outstanding and new properties are accessible with high quenching rates [136], [137] of the order of 10^{12} K

s^{-1} and high kinetic energies of the deposited atoms in the range of about 10 eV such as magnetron sputtering. In the present work, we investigate the nanocrystalline properties of magnetron sputtered Ir-layers sandwiched between HfO_2 during thermal treatment at different temperatures to enhance the selective emitter's thermal stability and optical properties.

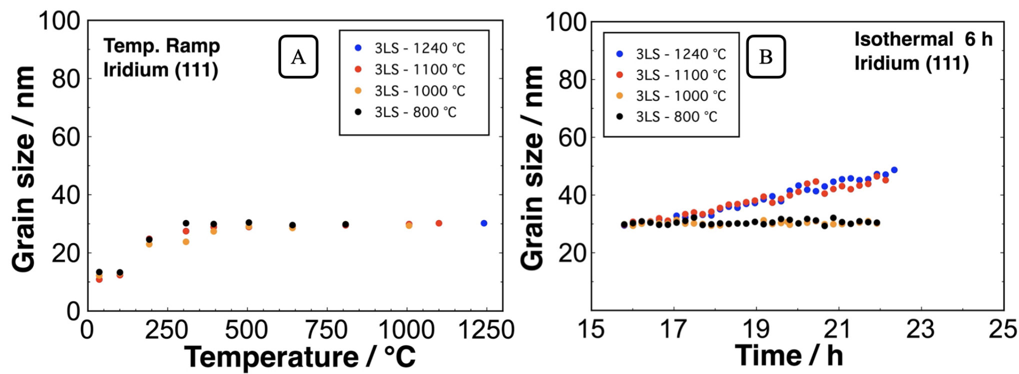

Figure 4.8: Measured grain size of fcc Iridium as a function of temperature during annealing ramp (A) and as a function of time during isothermal annealing (B) in the 3-layer-system; calculated from the FWHM of the (111) peak of the fcc Ir phase.

The evolution of the grain size in the out-of-the-plane direction in the 30 nm Ir layer of the annealed 3-layer-system as a function of time and temperature are shown in Figure 4.8. At the beginning, the grain size of Ir in the as-prepared 3-layer-system is around 12 nm indicating they are nanocrystalline. Grain growth is observed in all the 3-layer-system uniformly during the annealing ramp. Above 250 °C, the grain size approaches a value of 30 nm and remains constant throughout the whole annealing ramp for all applied annealing temperatures up to 1240 °C (Figure 4.8 A). In the

isothermal part of the annealing, distinct changes in grain growth become apparent up to 1000 °C for 6 h.The grain size of Ir saturated at 30 nm. However, further grain growth is observed in the 3-layer-system annealed at 1100 °C and 1240 °C, reaching values close to 50 nm linearly after 6 h (Figure 4.8 B), which is significantly higher than the layer thickness.

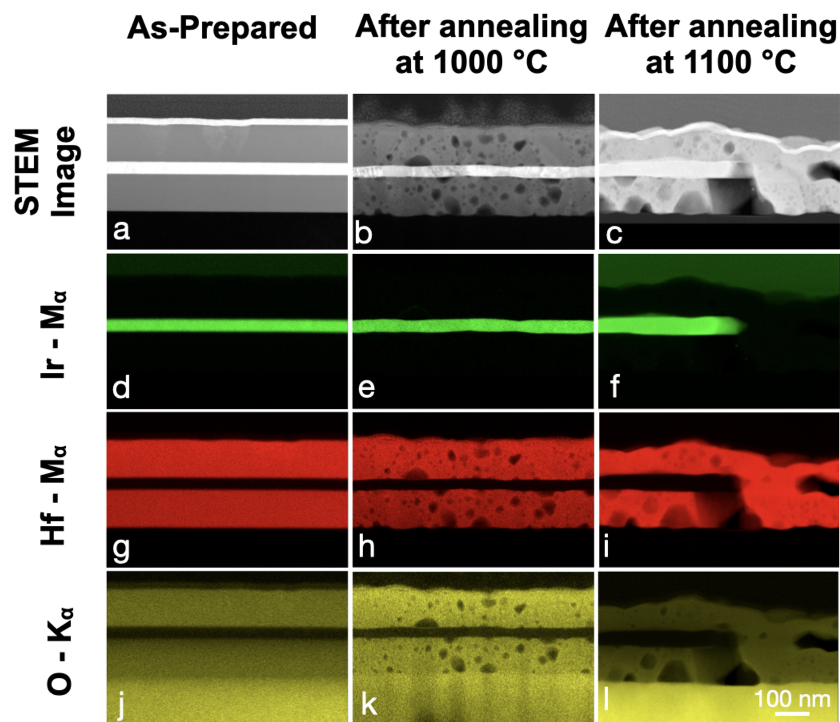

Figure 4.9: STEM-EDS analysis of the 3-layer-system, as-prepared, annealed at 1000 °C and 1100 °C for 6 h at 2×10^{-6} mbar. STEM-HAADF images (a-c), Ir-M_α elemental mapping (d-f), Hf-M_α elemental mapping (g-i), O-K_α elemental mapping (j-l).These images have the same scale as indicated in image (l). The top of the 3-layer-system is coated with Au in order to circumvent the effect of charging.

In order to understand the increase of Ir grain size in the 3-layer-system above 1000 °C, TEM-EDS characterizations on the as-prepared and annealed samples were performed. The STEM-high-angle annular dark-field (STEM-HAADF) image and the elemental mapping (Figure 4.9 a, d, g, and j) of the as-prepared sample show a 3-layer-system with a smooth interface between layers. The top layer is coated with a layer of Au in order to circumvent the effect of charging. After annealing at 1000 °C for 6 h, there is no noticeable change in the Ir layer, but some voids are generated in the HfO_2 layers (Figure 4.9 b, e, h and k), the interface between Ir and HfO_2 layers appears to be unaltered. No grain boundaries were seen in the studied TEM lamella.

After annealing the sample at 1100 °C for 6 h, drastic changes in morphology occur (Figure 4.9 c). An increase in the interface roughness of the HfO_2 layers is clearly visible. The Ir layer is discontinuous and thicker compared to the sample annealed at 1000 °C. The EDS mapping of Ir (Figure 4.9 f) shows a strong signal from Ir and no presence of oxygen (Figure 4.9 l), which is a clear indication of no oxidation in the Ir layer. Likewise, the HfO_2 layer (Figure 4.9 i and l) contains only signal from Hf-M_α and O-K_α, that confirms no evidence of inter diffusion between Ir and HfO_2.

Similar in-situ annealing experiments were performed on a bilayer (without a top HfO_2 layer) between 800 °C and 1100 °C, in order to interpret the mechanism that triggers grain growth exceeding the layer thickness in a 3-layer-system. During the temperature ramp, the grain size reaches a maximum value of 30 nm in all the samples. However, grain size reaches 40 nm

during isothermal annealing, exceeding the layer thickness starting from 900 °C.

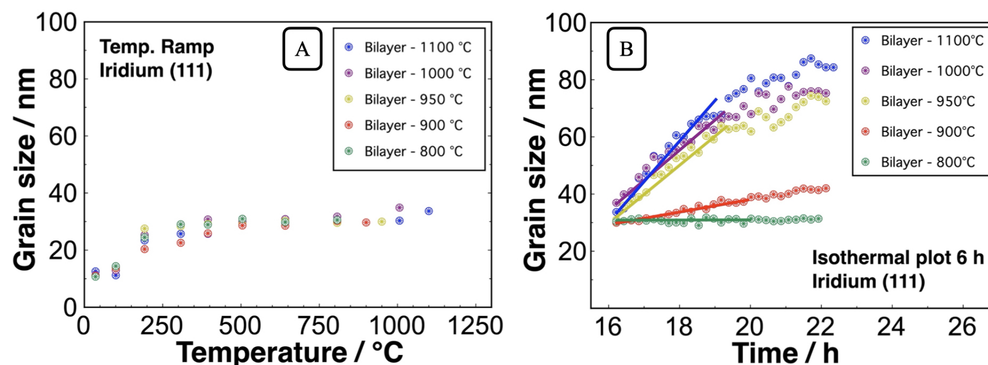

Figure 4.10: Measured grain size of fcc Iridium as a function of temperature during annealing ramp (A) and as a function of time during isothermal annealing (B) in the bilayer system; calculated from the FWHM of the (111) peak of the fcc Ir phase.

At higher temperatures between 900 °C and 1100 °C, the grain size rapidly increases to 60 nm (Figure 4.10). Later due to a change in kinetics, the growth rate is slowed down, reaching a final value of 80 nm.

As a means to realize the just described alteration of bilayer above 900 °C better, further characterization of their morphology was performed using conductive Atomic Force Microscopy (c-AFM). Figure 4.11 A shows the smooth morphology of the as-prepared bilayer system with a roughness in the sub-nanometer range as seen before by XRR. The green line (Figure 4.11 D), is a typical very flat height profile before annealing. The morphology of the annealed bilayer at 1000 °C (Figure 4.11 B) shows no more continuous Ir layer, but rather an agglomeration of Ir to form net-like structures. The

cross-section (pink) shown in Figure 4.11 D exhibits two plate-like islands with a width of 300 – 900 nm. The surface roughness on the top of the Ir islands is low, whereas between the islands the surface roughness of HfO_2 is about 15 - 20 nm. The step height of the Ir islands is in the range of 60 - 100 nm, which is in good agreement with the calculated grain size from the measured XRD patterns for an annealing temperature of 1000 °C.

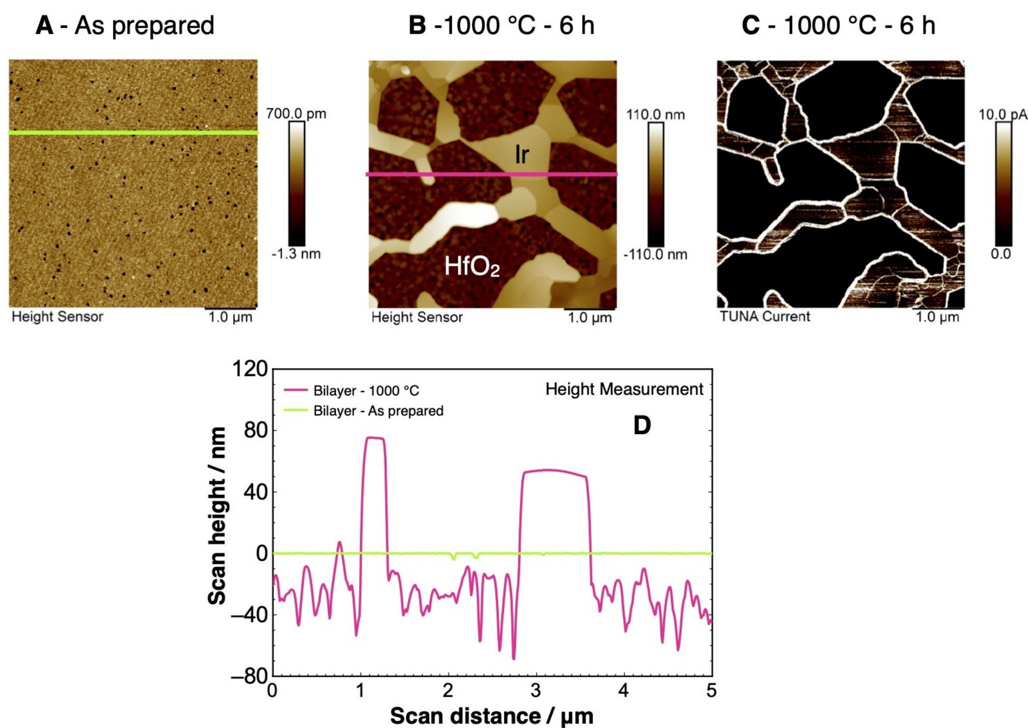

Figure 4.11: AFM images of (A) as-prepared morphology of Ir top layer (Bilayer- Ir/ HfO_2), (B) morphology of the same bilayer showing agglomeration of Ir into net like structures after annealing at 1000 °C for 6 h, (C) conductive AFM- showing flow of current from Ir areas and non-conducting parts from the HfO_2 layer (D) height profile of the bilayer before and after annealing.

Figure 4.11 C shows the current measurements over the net-like structures. High currents up to (10 pA) can be measured on the agglomerated structures, which is another indication that it is metallic Ir, no current can be measured on the exposed dielectric HfO_2.

The loss of cohesion of the uppermost layer of the bilayer is due to the agglomeration of Ir from 900 °C. Here, the driving force for agglomeration [138] is to minimize the total energy of the free surfaces of Ir and the Ir-HfO_2 interface. In general, thin metal films deposited on an oxide surface are metastable and dewet to form islands by surface diffusion at 0.5 T_m, called Tammann temperature [139]. The first step in agglomeration proceeds by hole formation, due to stress arising from different thermal expansion coefficients between Ir [105] is 8.4×10^{-6} K^{-1} and HfO_2 [119] is 20×10^{-6} K^{-1} at 1000 °C. The formed holes then grow to form dewetted regions that overlap, resulting in dewetting of the entire film. Nevertheless, in the 3-layer-system, HfO_2 acts as an excellent top layer, and the additional interface restricts the agglomeration in the Ir layer up to 1000 °C (as seen in Figure 4.8). The above experiments validate the thermal stability of Ir sandwiched between two HfO_2 layers and served as a foundation for developing a advanced multilayered metamaterial selective emitter.

4.3 Thermal stability of Ir as a function of O_2 partial pressure

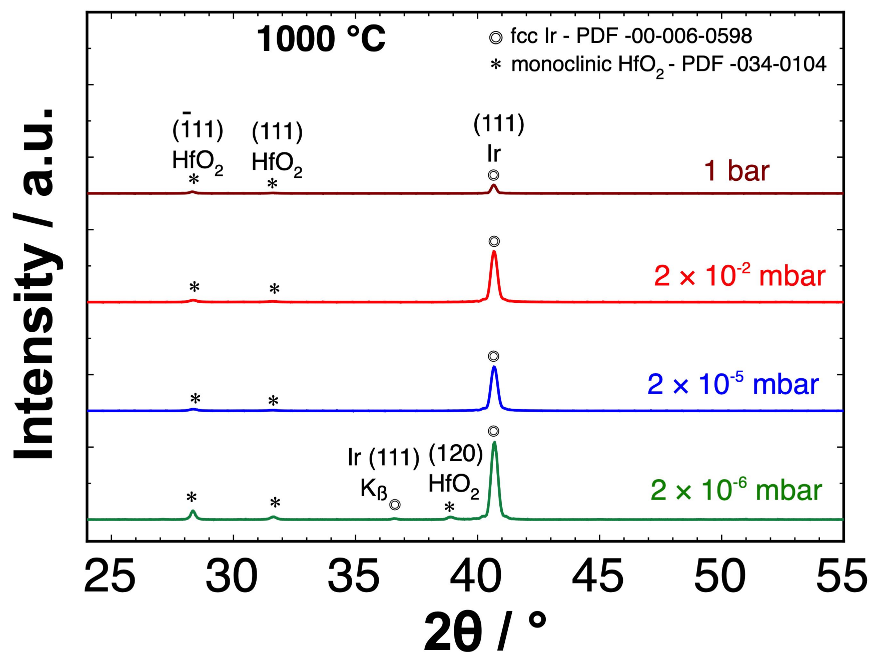

Figure 4.12: Normalized diffraction patterns of a 3-layer-system measured at room temperature, after annealing it at 1000 °C for 6 h at different pressures. All scans in the plot are background normalized for comparison.

In this section, the 3-layer-system was ex-situ annealed at four different vacuum pressures to verify thermal stability and the oxidation resistance of Ir. The annealing was performed at 1000 °C for 6 h at 1 bar, 2×10^{-2} mbar, 2×10^{-5} mbar, and 2×10^{-6} mbar. Figure 4.12 shows a waterfall plot containing four diffractograms of a 3-layer-system measured at room temperature after annealing. The prominent peaks are (-111) and (111) from monoclinic HfO_2,

and the (111) fcc peak from Ir. There is no hint of Ir oxidation or peaks from IrO_2 present in the diffractograms that were actually recorded between 20° - 100°. Nevertheless, a clear drop in intensity of the 3-layer-system annealed at 1 bar is due to direct sublimation of volatile IrO_x.

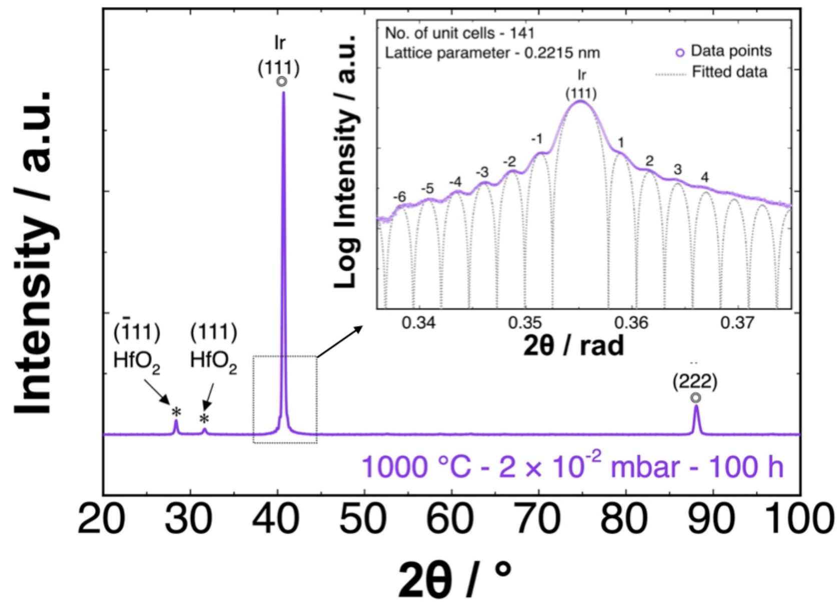

Figure 4.13: Diffraction pattern of a 3-layer-system ex-situ annealed at 1000 °C for 100 h at 2 $\times 10^{-2}$ mbar, the inset shows presence of higher order satellite peaks due to coherent scattering and sharp interfaces between the layers.

To test the durability of the 3-layer-system from an application point of view, annealing measurements were performed at 1000 °C for 100 h at 2 $\times 10^{-2}$ mbar, the diffractograms (Figure 4.13) show no sign of oxidation even at an increased time frame. The (111) Ir peak highlighted in a black frame

contains more minor oscillations at the foot of the peak.

The oscillations are distinctly visible in the inset containing intensity plotted in the log scale. These oscillations are satellite peaks from the primary (111) Ir Bragg peak. The satellite peaks are formed due to crystalline coherence and a sharp interface between the top and bottom Ir/HfO_2 interfaces. These peaks are absent in the as-prepared sample and are visible in the 3-layer-system only after annealing the sample above 900 °C due to higher ordering and the fact that the grains span the full thickness of the Ir layers. The peaks in the inset are fitted using the following function [140],

$$I(\theta) = \left[\frac{\mathrm{Sin}\left(\frac{\pi\, n\, c\, \mathrm{Sin}\,\theta}{\lambda}\right)}{\mathrm{Sin}\left(\frac{\pi\, c\, \mathrm{Sin}\,\theta}{\lambda}\right)} \right]^2 \tag{4.3}$$

Where c is the lattice parameter in the out-of-the-plane direction, n is the number of unit cells that can be accommodated in the out-of-the-plane direction, λ is the wavelength of x-rays (for Cu K_α radiation: λ=0.15046 nm), and θ is the Bragg angle in radians. The lattice parameter c is 0.2215 nm and the number of unit cells n are 141, for the 3-layer-system annealed at 1000 °C for 100 h, at 2×10^{-2} mbar. The product of these two parameters can also be used to calculate the thickness of the film [141]. Satellite peaks can be used as a critical marker to determine the stability of the layer structure in a 3-layer-system using X-rays. A change in peak position or absence of higher-order peaks indicates a change in film thickness or loss of coherence due to agglomeration of Ir.

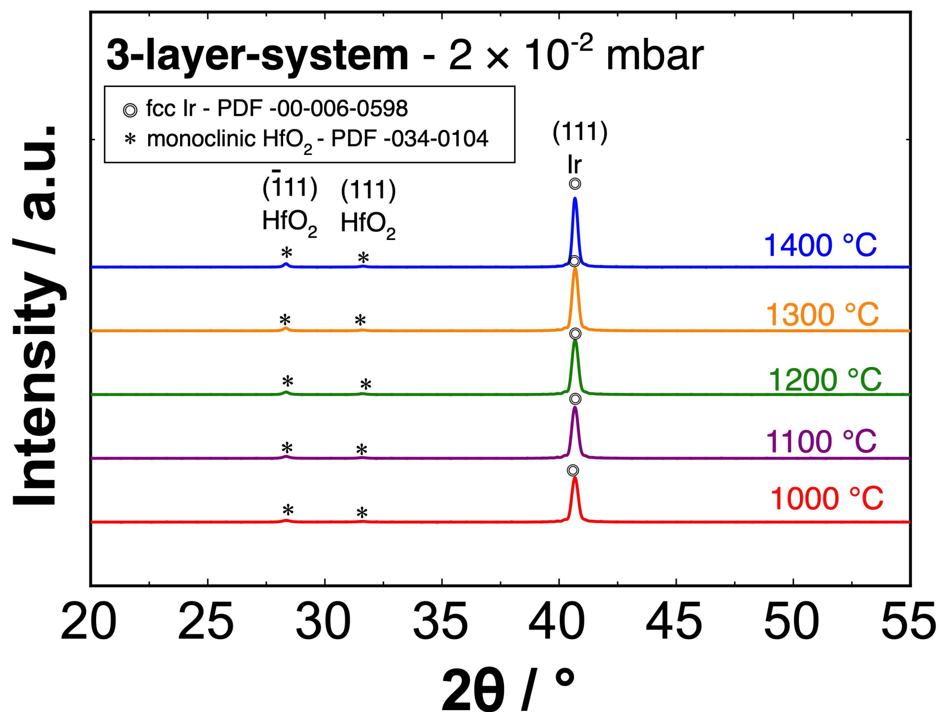

Figure 4.14: X-ray diffractograms of a 3-layer-system ex-situ annealed at different temperature at 2×10^{-2} mbar for 6 h. Only prominent peaks from (111)fcc Ir and (-111) monoclinic HfO_2 are visible. All scans are normalized to the background.

3-layer-system ex-situ annealed at a vacuum pressure of 2×10^{-2} mbar at different temperatures for a duration of 6 h are shown in Figure 4.14. Higher-order satellite reflections from the primary (111) Ir peak are magnified in a logarithmic scale in Figure 4.15. The 3-layer-system displays good oxidation resistance at all temperatures with no sign of IrO_2 formation. It is worthwhile to mention for the same vacuum pressure W gets oxidized to form WO_2 starting from 1100 °C [40], [41]. Satellite peaks up to 8 orders are visible for

the Ir sample annealed at 1000 °C All the satellite peaks were fitted using the equation (4.3) and the fit parameters are shown in the table 4.2 .

Temperature °C	d_{111} / nm	No. of unit cells	Thickness / nm
1000	0.2215	141	31.2
1100	0.2215	141	31.2
1200	0.2215	141	31.2
1300	0.2215	145	32.1
1400	0.2215	154	34.1

Table 4.2: Simulated parameters of the satellite peaks after annealing at different temperatures at 2 $\times 10^{-2}$ mbar for 6 h.

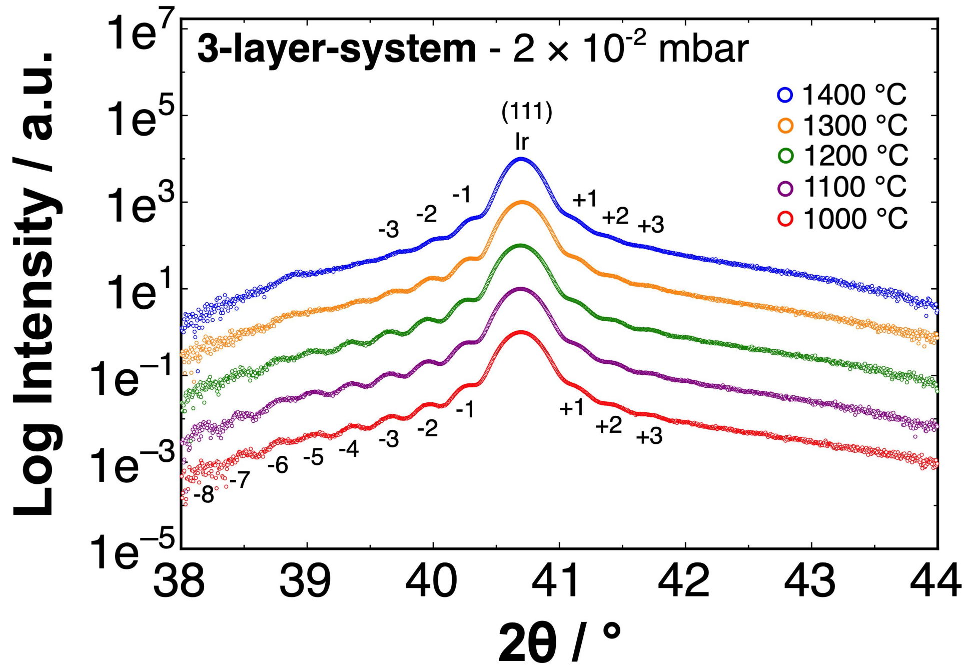

Figure 4.15: Higher order satellite peaks from the primary (111) fcc Ir Bragg peak from the 3-layer-system ex-situ annealed at different temperature for 6 h. Some of higher order peaks start to vanish above 1200 °C. All scans are normalized to the peak maximum.

In the 3-layer-system annealed at 2×10^{-2} mbar Figure 4.15, the position of the 1st order (-1) peak is 40.24° for the 3-layer-system annealed up to 1200 °C. A shift of the (-1) peak towards the higher angle for the sample annealed at 1300 °C (40.26°) and 1400 °C (40.3°) is observed. The 3-layer-system annealed at 1400 °C revealed the disappearance of 5 higher-order peaks, indicating loss of crystalline coherence.

4.4 Durability between Ir/HfO$_2$ and W/HfO$_2$ selective emitters

After testing the 3-layer-system at different pressures and temperatures, an Ir/HfO$_2$ multilayered metamaterial selective emitter was fabricated and tested for long-term durability as seen in Figure 4.16 B. An experimental comparison is also made with a W/HfO$_2$ system Figure 4.16 F. In-situ annealing experiments were performed at 1000 ° C for 100 h at 2×10^{-6} mbar to study the kinetics, and check the influence of oxidation of both the metals in a multilayered metamaterial selective emitter.

Figure 4.16 A shows the integrated intensity of (111) fcc Ir and (110) bcc W as a function of time during the isothermal annealing at 1000 °C. The intensity of Ir is almost stable over the entire duration, whereas a gradual drop in intensity is observed for W due to oxidation and later sublimation of volatile WO$_x$. The FTIR measurements (Figure 4.17) also shows less absorption compared to the as-prepared sample and the desired long wavelength

suppression above the cut of the wavelenght of a InGaAsSb PV cell.

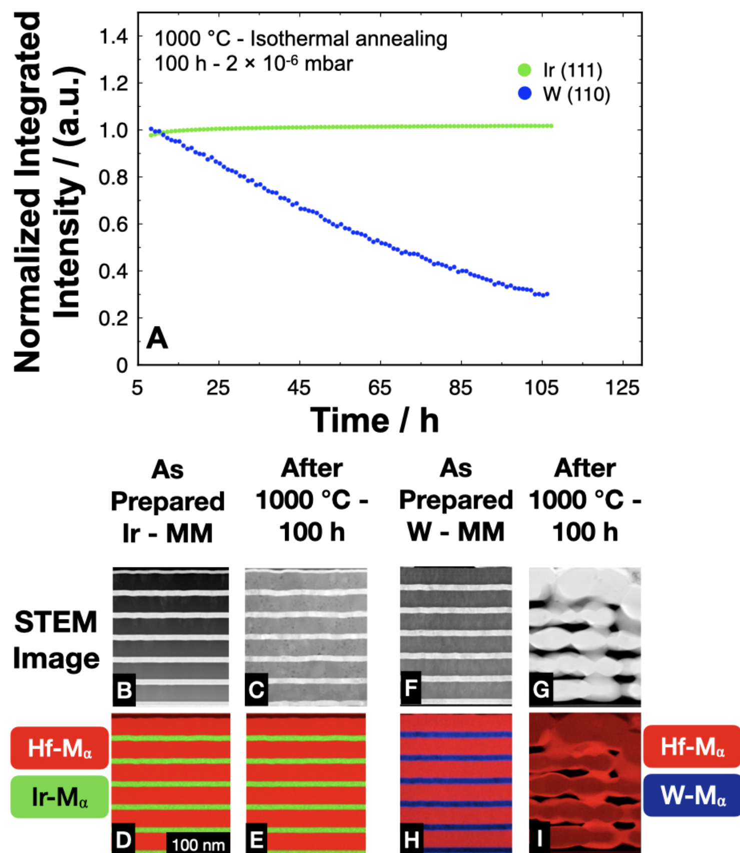

Figure 4.16: (A) Normalized integrated intensity of (111) fcc Ir and (110) bcc W during isothermal annealing as a function of time annealed over 100 h at 1000 °C in a pressure of 2×10^{-2}mbar.(B-I) STEM-EDS analysis of the Ir/HfO_2 and W/HfO_2 metamaterial, as-prepared and annealed at 1000 °C for 100 h. (B and C) STEM-HAADF images of Ir/HfO_2 metamaterial, (D and E) Ir -M_α(green) and Hf -M_α (red) mix elemental mapping, (F and G) STEM-HAADF images of W/HfO_2 metamaterial , (H and I) W -M_α(blue) and Hf -M_α (red) mix elemental mapping. All the images have the same scale as indicated in (D).

The x-rays results are also validated by the STEM-EDS measurements

(Figure 4.16 D, E, H and I). The Ir/HfO_2 metamaterial is unaltered (Figure 4.16 E) in comparison to the as-prepared sample, there is no sign of oxidation in the Ir layer or agglomeration of Ir after 100 h. However, in the W/HfO_2 there is almost no signal from the W layer after 100 h (Figure 4.16 I), as the W layer is first oxidized and directly the formed W oxide is sublimated. Also an increased roughness is observed in the HfO_2 layers. The above experiments demonstrates that Ir is a more suitable material for selective emitters in comparison to W.

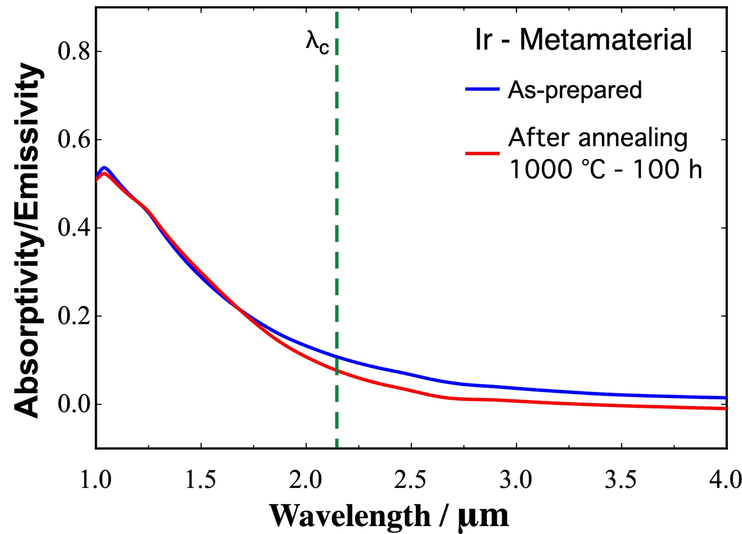

Figure 4.17: Experimental absorptivity/emissivity spectrum of an as-prepared (blue) and ex-situ annealed (red) Ir metamaterial after 1000 °C,100 h. Where λ_c is the cut-off wavelength of the InGaAsSb PV cell at 2.25 μm.

A summary of the chapter is represented by a schematic shown in Figure 4.18. The thermal stability and the oxidation resistance of a 3-layer-system (30 nm Ir, sandwiched between two 100 nm HfO_2 layers) was tested using

ex-situ annealing at different temperatures, pressures and time duration. At 1 bar pressure , the 3-layer-system is stable at 500 °C up to 6 h. On further increasing the temperature, direct sublimation of Ir starts at 800 °C and is more rapid at 1000 °C. At a pressure of 2×10^{-2} mbar the 3-layer-system is stable at 1200 °C up to 100 h. The stability of the layers are validated by x-ray satellite peaks that are formed above 900 °C due to crystalline coherence and sharp interface. Above 1200 °C higher order satellite peaks start to vanish due to agglomeration of Ir. There is no sign of oxidation in the diffractograms. On moving to 2×10^{-5} mbar (ex-situ annealing), the 3-layer-system exhibits no sign of oxidation and is stable up to 1300 °C.

In-situ annealing experiments were performed on the 3-layer-system, between 800 °C and 1240 °C at 2×10^{-6} m bar pressure for a duration of 6 h to understand the mechanism of failure. Grain growth in the Ir layer reaches a value of 30 nm, equal to the layer and remains stable during isothermal annealing up to 1000 °C. On increasing the temperature, grains size reaches value above 40 nm higher than the layer thickness. Annealing on a bilayer sample without a top HfO_2 layer show agglomeration of Ir to minimize surface energy. Therefore the mechanism of failure in Ir is dominated by agglomeration and not by oxidation. As a further step towards application, a multilayered metamaterial (Ir/HfO_2) selective emitter was fabricated and annealed at 1000 °C for 100 h. In comparison to a W metamaterial, Ir shows very good thermal stability. Therefore the oxidation-resistant nature of Ir makes it a durable material for a selective emitter used in thermophotovoltaics.

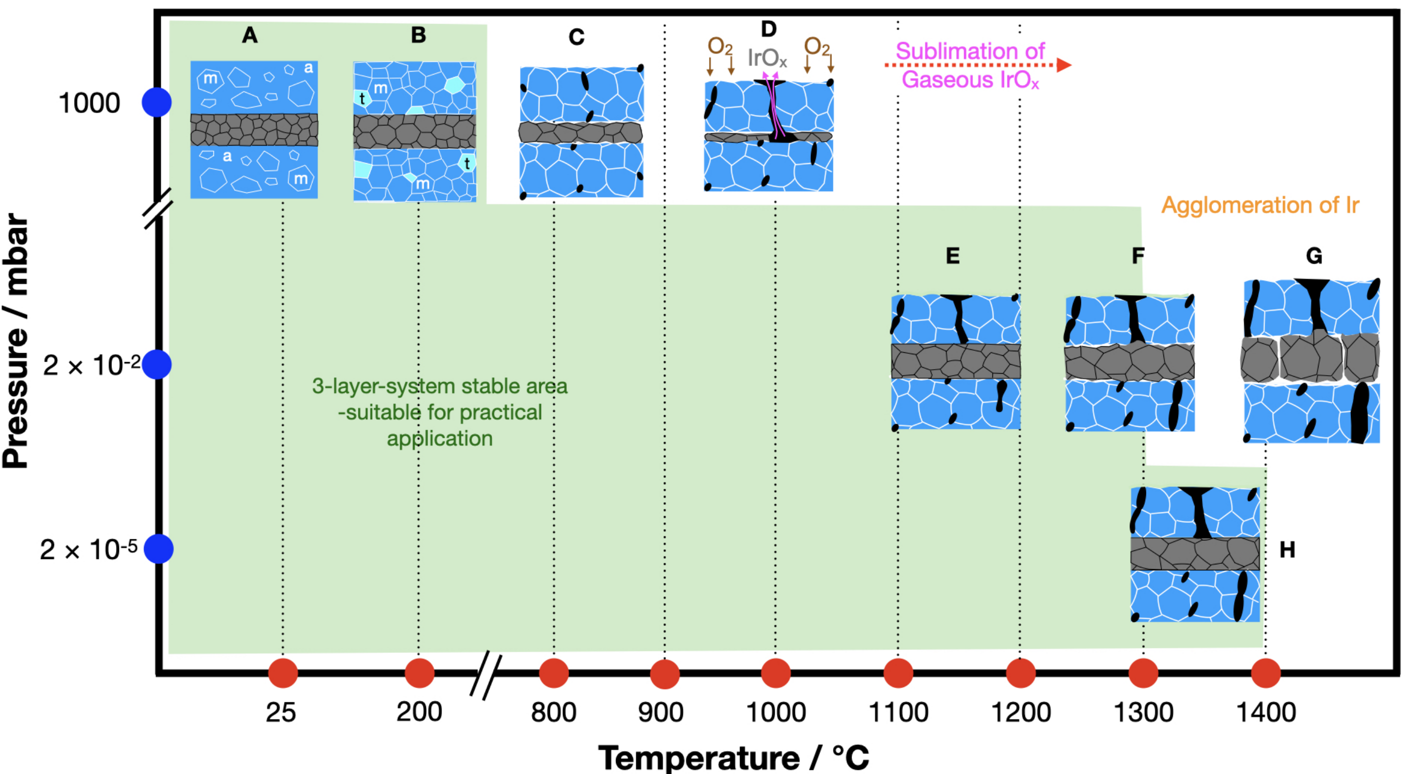

Figure 4.18: Schematic representing the failure mechanism in a Ir 3-layer-system at different temperature and pressure ranges. (A) As-prepared 3-layer-system, HfO_2 exist in monoclinic and amorphous phase, (B) Amorphous HfO_2 transforms to tetragonal HfO_2, (C) Tetragonal HfO_2 transforms completely into monoclinic HfO_2, resulting in void formation, due to 3.5% increase in unit cell volume, (D) Oxygen molecules travel through the developed transport channel and oxidize Ir forming volatile IrO_x that sublimate, (E) Ir layer is stable with sharp interfaces at (F) Roughness increase at the Ir/HfO_2 interfaces, (G) Ir grains grow more than 30 nm and the layer size increases at 1400 °C for 6 h at 2×10^{-2} mbar, and (H) 3-layer-system stable below 1300 °C for 6 h at 2×10^{-5} mbar. The zone in green represents the area where the 3-layer-system can perform efficiently for a duration over 100 h.

Chapter 5

Conclusion and Outlook

In this thesis, a combination of magnetron sputtered thin films, high-temperature annealing, and characterization by XRD is used to elucidate the thermal stability of selective emitters. The scientific investigations have been carried out under different working conditions. The experimental parameters include selection of material systems, film thickness, annealing temperature, vacuum pressure, various layer structures in the samples, i.e., bilayer, 3-layer-system, and multilayered metamaterial. Based on the material system, W/HfO_2 and Ir/HfO_2 different processes like oxidation or agglomeration is explained that lead to the selective emitter's failure at high temperatures. This thesis gives a perspective to systematically fabricate, perform high temperature annealing experiments and characterize the thermal stability of multilayered selective emitters used in TPV applications. From these insights the thesis work intends to provide criteria and guidelines for material choices

and designs of selective TPV emitters.

Summary of major contribution:

Thermal validation

Prior to performing experiments, a systematic procedure for temperature validation of high-temperature measurements using strip heaters that can reach very high temperatures up to 2000 °C in a in-situ XRD set up is developed. Thermal expansion coefficients for W, MgO, and sapphire are measured using x-rays at a low vacuum pressure below 3×10^{-6} mbar.

Tungsten - Hafnia System

The first part of experimental results focus on W/HfO_2 thin film material system

- The first set of ex-situ experiments were performed at different vacuum pressure between 2×10^{-2} mbar - 2×10^{-5} mbar, and validate the highest temperature, at which the selective emitter is thermally stable. An ex-situ annealed six bilayer W/HfO_2 metamaterial is stable at 1400 °C for 6 h at 2×10^{-5} mbar. The layered structure is disrupted by further increasing the temperature, failing to meet the required optical properties. At 2×10^{-2} mbar, the metamaterial fails above 1100 °C due to oxidation of W.

- The second set of ex-situ experiments are conducted in Ar atmosphere to reduce the impact of O_2 partial pressure. An ex-situ annealed six bilayer W/HfO_2 metamaterial was stable at 1300 °C for 6 h, on further increasing the temperature, an increase in absorption was observed, leading to degradation of optical properties. The reason for the increase in absorption is due to the presence of voids in the W and HfO_2 layers.

- The third set of in-situ experiments were performed on a simplified 3-layered-system (HfO_2/W/HfO_2). Annealing experiments were done at different temperatures between 300 °C - 1520 °C, for different duration 6 h, 20 h and 40 h at vacuum pressure below 3×10^{-6} mbar. An amorphous to tetragonal phase transformation between 125 °C - 200 °C is observed in the HfO_2 layer followed by tetragonal - monoclinic phase transformation between 200 °C - 800 °C. The phase transition leads to volume changes in the unit cell finally resulting in void formation in the HfO_2 layer. These voids agglomerate and act as transport channels for the residual O_2 present in the chamber to reach the W layer, and form WO_x that sublimate at higher temperatures and low vacuum pressure. The disappearance of W is validated by a drop in integrated intensity of (110) W peak, and an activation energy of 1.2 eV is calculated for the process. The disappearance is also validated by STEM-EDX and RBS measurements. One of the key findings of the first part of the thesis was determining the failure mechanism for W/HfO_2 thin-film selective emitter.

Iridium - Hafnia System

The second part of experimental results focus on Ir/HfO_2 material system

- The objective was to use Ir as a replacement for W due to its small negative Gibbs energy of formation upon oxidation and verify its expected resistance to oxidation. Initially, in-situ annealing was done on a 3-layer-system (HfO_2/Ir/HfO_2/substrate) between 800 °C - 1240 °C at a pressure below 3×10^{-6}mbar. In the bilayer without a top HfO_2 protection layer, the Ir layer starts to agglomerate by surface diffusion above 900 °C. Whereas, in the 3-layer-system annealed at 1000 °C for 6 h, HfO_2 acts as an excellent top layer preventing surface diffusion of Ir.

- In the second part, ex-situ annealing of the 3-layer-system was done at different temperatures between 500 °C - 1400 °C and in a pressure range between 1 bar and 2×10^{-5} mbar. At 1 bar the 3-layer-system failed by direct sublimation of Ir above 500 °C. The 3-layer-system exhibits good thermal stability without any oxidation up to 1200 °C, 100 h at 2×10^{-2} mbar. Diffractograms show presence of satellite peaks that appear adjacent to the primary (111) fcc Ir peak after annealing the sample above 900 °C. The satellite peak serves as marker to determine the thermal stability of the layer structure.

- Based on the thermal stability of the 3-layer-system at 1000 °C, a comparison study between two multilayered selective emitters Ir/HfO_2 and

W/HfO_2 was performed. Both the metamaterials were annealed at 1000 °C for 100 h at 2×10^{-2} mbar. Future work is focused on increasing the stability of Ir above 1000 °C as discussed in the next sub-section. The Ir emitter shows very good thermal stability with no sign of layer disruption or agglomeration or any oxidation of Ir, which is also validated by FTIR measurements that show good spectral emissivity and less absorption at higher wavelengths. However, in the W emitter gradual oxidation and sublimation of volatile WO_x was observed. The Ir/HfO_2 system presents a new outlook on Ir as suitable material for selective emitters in thermophotovoltaic applications.

Future Work:

- Regarding metals, extensive work is done focused on W and Ir layers because of their high melting points and low vapor pressures. However, in comparison to W, Ir exhibits better oxidation resistance. The possibility to prevent oxidation in W is to be tested by alloying it with a second element like Re, Mo or Rh to increase it's oxidation resistance.

- Voids in HfO_2 layer are generated due to phase transformations (amorphous → tetragonal → monoclinic). The fabrication process should be modified to prepare HfO_2 layer above 900 °C to directly obtain the monoclinic phase and test for structural stability of a W/HfO_2 3-layer-system. Also doping HfO_2 with Y can stabilize the tetragonal phase

and prevent phase transformation. The next ideal choice will be using yttrium stabilized zirconia (YSZ), with 7.8% yttria that stabilizes the cubic phase and evades phase transformation in zirconia.

- Alloying Ir with W can address the problem of grain growth in Ir films and further testing is required to validate the thermal stability at a temperature higher than 1000 °C. The W atoms pin the grain boundaries and prevent grain growth in Ir.

- The thermal stability of selective emitters can also be enhanced by using inter-diffusion layers between the metal and dielectric stack.

- Current work focuses on developing the material system for selective emitters. The long-term strategy of developing a fully functioning TPV system for practical applications still needs validation of thermal stability of selective emitters over 1000 h.

Bibliography

[1] Spencer Dale. Bp energy outlook. https://www.bp.com/content/dam/bp/business-sites/en/global/corporate/pdfs/energy-economics/energy-outlook/bp-energy-outlook-2022.pdf, 2022.

[2] Michael Papapetrou, George Kosmadakis, Andrea Cipollina, Umberto La Commare, and Giorgio Micale. Industrial waste heat: Estimation of the technically available resource in the eu per industrial sector, temperature level and country. *Applied Thermal Engineering*, 138:207–216, 2018.

[3] David Vance, Sachin Nimbalkar, Arvind Thekdi, Kristina Armstrong, Thomas Wenning, Joseph Cresko, and Mingzhou Jin. Estimation of and barriers to waste heat recovery from harsh environments in industrial processes. *Journal of Cleaner Production*, 222:539–549, 2019.

[4] Sarah Brückner, Selina Liu, Laia Miró, Michael Radspieler, Luisa F. Cabeza, and Eberhard Lävemann. Industrial waste heat recovery technologies: An economic analysis of heat transformation technologies. *Applied Energy*, 151:157–167, 2015.

[5] David B. Go, John R. Haase, Jeffrey George, Jochen Mannhart, Robin Wanke, Alireza Nojeh, and Robert Nemanich. Thermionic energy conversion in the twenty-first century: Advances and opportunities for space and terrestrial applications. *Frontiers in Mechanical Engineering*, 3:13, 2017.

[6] Nesrine Jaziri, Ayda Boughamoura, Jens Müller, Brahim Mezghani, Fares Tounsi, and Mohammed Ismail. A comprehensive review of thermoelectric generators: Technologies and common applications. *Energy*

Reports, 6:264–287, 2020. SI:Energy Storage - driving towards a clean energy future.

[7] Nurettin Sezer and Muammer Koç. A comprehensive review on the state-of-the-art of piezoelectric energy harvesting. *Nano Energy*, 80:105567, 2021.

[8] R.M Swanson. A proposed thermophotovoltaic solar energy conversion system. *Proceedings of the IEEE*, 67(3):446–447, 1979.

[9] T. Bauer. *Thermophotovoltaics: Basic Principles and Critical Aspects of System Design*. Green Energy and Technology. Springer Berlin Heidelberg, 2011.

[10] Zunaid Omair, Gregg Scranton, Luis M. Pazos-Outón, T. Patrick Xiao, Myles A. Steiner, Vidya Ganapati, Per F. Peterson, John Holzrichter, Harry Atwater, and Eli Yablonovitch. Ultraefficient thermophotovoltaic power conversion by band-edge spectral filtering. *Proceedings of the National Academy of Sciences*, 116(31):15356–15361, 2019.

[11] Vidya Ganapati, T. Patrick Xiao, and Eli Yablonovitch. Ultra-efficient thermophotovoltaics exploiting spectral filtering by the photovoltaic band-edge. *arxiv preprint arxiv:1611.03544*, 2016.

[12] Svetlana V. Boriskina, Martin A. Green, Kylie Catchpole, Eli Yablonovitch, Matthew C. Beard, Yoshitaka Okada, Stephan Lany, Talia Gershon, Andriy Zakutayev, Mohammad H Tahersima, et al. Roadmap on optical energy conversion. *Journal of Optics*, 18(7):073004, 2016.

[13] Richard M. Swanson. Silicon photovoltaic cells in thermophotovoltaic energy conversion. In *1978 International Electron Devices Meeting*, pages 70–73. IEEE, 1978.

[14] Manohar Chirumamilla, Anisha Chirumamilla, Yuanqing Yang, Alexander S. Roberts, Peter Kjær Kristensen, Krishnakali Chaudhuri, Alexandra Boltasseva, Duncan S. Sutherland, Sergey I Bozhevolnyi, and Kjeld Pedersen. Large-area ultrabroadband absorber for solar thermophotovoltaics based on 3d titanium nitride nanopillars. *Advanced Optical Materials*, 5(22):1700552, 2017.

[15] Christopher J. Crowley, Nabil A. Elkouh, Susan Murray, and Donald L. Chubb. Thermophotovoltaic converter performance for radioisotope power systems. In *AIP Conference Proceedings*, volume 746, pages 601–614. American Institute of Physics, 2005.

[16] A. Datas and A. Martí. Thermophotovoltaic energy in space applications: Review and future potential. *Solar Energy Materials and Solar Cells*, 161:285–296, 2017.

[17] Hongyu Wang, Xiaobin Tang, Yunpeng Liu, Zhiheng Xu, Zicheng Yuan, Kai Liu, Zhengrong Zhang, and Tongxin Jiang. Thermal emission-enhanced and optically modulated radioisotope thermophotovoltaic generators. *Energy Technology*, 8(3):1901170, 2020.

[18] Robert E. Nelson. A brief history of thermophotovoltaic development. *Semiconductor Science and Technology*, 18(5):S141, 2003.

[19] T.J. Coutts. A review of progress in thermophotovoltaic generation of electricity. *Renewable and sustainable energy reviews*, 3, 1999.

[20] C. Ferrari, F. Melino, Michele Pinelli, Pier Ruggero Spina, and Mauro Venturini. Overview and status of thermophotovoltaic systems. *Energy Procedia*, 45:160–169, 2014.

[21] Yang Wang, Haizhou Liu, and Jia Zhu. Solar thermophotovoltaics: Progress, challenges, and opportunities. *APL Materials*, 7(8):080906, 2019.

[22] E. Hecht. *Optics*. Pearson, 2016.

[23] Max Planck. *The theory of heat radiation*. Blakiston, 1914.

[24] Donald Chubb. *Fundamentals of thermophotovoltaic energy conversion*. Elsevier, 2007.

[25] Sean Molesky, Christopher J. Dewalt, and Zubin Jacob. High temperature epsilon-near-zero and epsilon-near-pole metamaterial emitters for thermophotovoltaics. *Optics express*, 21(101):A96–A110, 2013.

[26] Jiafang Li, M.D. Muntasir Hossain, Baohua Jia, Dario Buso, and Min Gu. Three-dimensional hybrid photonic crystals merged with localized plasmon resonances. *Optics express*, 18(5):4491–4498, 2010.

[27] Eden Rephaeli and Shanhui Fan. Absorber and emitter for solar thermo-photovoltaic systems to achieve efficiency exceeding the shockley-queisser limit. *Optics express*, 17(17):15145–15159, 2009.

[28] David L.C. Chan, Marin Soljačić, and J.D. Joannopoulos. Thermal emission and design in 2D-periodic metallic photonic crystal slabs. *Optics express*, 14(19):8785–8796, 2006.

[29] Xianliang Liu, Talmage Tyler, Tatiana Starr, Anthony F. Starr, Nan Marie Jokerst, and Willie J. Padilla. Taming the blackbody with infrared metamaterials as selective thermal emitters. *Physical Review Letters*, 107(4):045901, 2011.

[30] Reyu Sakakibara, Veronika Stelmakh, Walker R. Chan, Michael Ghebrebrhan, John D. Joannopoulos, Marin Soljacic, and Ivan Čelanović. Practical emitters for thermophotovoltaics: a review. *Journal of Photonics for Energy*, 9(3):032713, 2019.

[31] Nicole. A. Pfiester and Thomas. E. Vandervelde. Selective emitters for thermophotovoltaic applications. *Physica status solidi (a)*, 214(1):1600410, 2017.

[32] David N. Woolf, Emil A. Kadlec, Don Bethke, Albert D. Grine, John J. Nogan, Jeffrey G. Cederberg, D. Bruce Burckel, Ting Shan Luk, Eric A. Shaner, and Joel M. Hensley. High-efficiency thermophotovoltaic energy conversion enabled by a metamaterial selective emitter. *Optica*, 5(2):213–218, 2018.

[33] M.G. Mauk, O.V. Sulima, J.A. Cox, and R.L. Mueller. Low-bandgap (0.3 to 0.5 ev) inassbp thermophotovoltaics: assessment for open-circuit voltage improvements. In *3rd World Conference onPhotovoltaic Energy Conversion, 2003. Proceedings of*, volume 1, pages 224–227 Vol.1, 2003.

[34] A.W Bett and O.V Sulima. Gasb photovoltaic cells for applications in tpv generators. *Semiconductor science and technology*, 18(5):S184, 2003.

[35] Veronika Rinnerbauer, Yi Xiang Yeng, Walker R. Chan, Jay J. Senkevich, John D. Joannopoulos, Marin Soljačić, and Ivan Celanovic. High-temperature stability and selective thermal emission of polycrystalline tantalum photonic crystals. *Optics express*, 21(9):11482–11491, 2013.

[36] Arvind Narayanaswamy and Gang Chen. Thermal emission control with one-dimensional metallodielectric photonic crystals. *Physical Review B*, 70(12):125101, 2004.

[37] Zhu Wang, Ting Shan Luk, Yixuan Tan, Dengxin Ji, Ming Zhou, Qiaoqiang Gan, and Zongfu Yu. Tunneling-enabled spectrally selective thermal emitter based on flat metallic films. *Applied Physics Letters*, 106(10):101104, 2015.

[38] Gerardo Silva-Oelker, Carlos Jerez-Hanckes, and Patrick Fay. Study of tungsten/hafnia grating selective thermal emitters for thermophotovoltaic applications. *Optics express*, 26(22):A929–A936, 2018.

[39] Andrea Alu, Mário G. Silveirinha, Alessandro Salandrino, and Nader Engheta. Epsilon-near-zero metamaterials and electromagnetic sources: Tailoring the radiation phase pattern. *Physical Review B*, 75(15):155410, 2007.

[40] Pavel N. Dyachenko, Sean Molesky, A. Yu Petrov, Michael Störmer, Tobias Krekeler, Slawa Lang, Martin Ritter, Zubin Jacob, and Manfred Eich. Controlling thermal emission with refractory epsilon-near-zero metamaterials via topological transitions. *Nature communications*, 7(1):1–8, 2016.

[41] Manohar Chirumamilla, Gnanavel Vaidhyanathan Krishnamurthy, Katrin Knopp, Tobias Krekeler, Matthias Graf, Dirk Jalas, Martin Ritter, Michael Störmer, Alexander Yu Petrov, and Manfred Eich. Metamaterial emitter for thermophotovoltaics stable up to 1400 °C. *Scientific reports*, 9(1):1–11, 2019.

[42] Igor L. Shabalin. *Ultra-high temperature materials II*. Springer, 2019.

[43] J. Hlavac. Melting temperatures of refractory oxides: Part i. *Pure and Applied Chemistry*, 54(3):681–688, 1982.

[44] J. Wang, H.P Li, and R. Stevens. Hafnia and hafnia-toughened ceramics. *Journal of materials science*, 27(20):5397–5430, 1992.

[45] Harish N.S. Krishnamoorthy, Zubin Jacob, Evgenii Narimanov, Ilona Kretzschmar, and Vinod M. Menon. Topological transitions in metamaterials. *Science*, 336(6078):205–209, 2012.

[46] A. Poddubny, I. Iorsh, P. Belov, and Y. Kivshar. Hyperbolic metamaterials, nat. photonics 7 (12), 948–957, 2013.

[47] Zhaowei Liu, Hyesog Lee, Yi Xiong, Cheng Sun, and Xiang Zhang. Far-field optical hyperlens magnifying sub-diffraction-limited objects. *science*, 315(5819):1686–1686, 2007.

[48] J. Kim, Vladimir P. Drachev, Z. Jacob, Gururaj V. Naik, Alexandra Boltasseva, Evgenii E. Narimanov, and Vladimir M. Shalaev. Improving the radiative decay rate for dye molecules with hyperbolic metamaterials. *Optics express*, 20(7):8100–8116, 2012.

[49] Dmitriy Korobkin, Burton Neuner, Chris Fietz, Nikoletta Jegenyes, Gabriel Ferro, and Gennady Shvets. Measurements of the negative refractive index of sub-diffraction waves propagating in an indefinite permittivity medium. *Optics express*, 18(22):22734–22746, 2010.

[50] Heon-Ju Lee, Katherine Smyth, Stephen Bathurst, Jeffrey Chou, Michael Ghebrebrhan, John Joannopoulos, Nannaji Saka, and Sang-Gook Kim. Hafnia-plugged microcavities for thermal stability of selective emitters. *Applied Physics Letters*, 102(24):241904, 2013.

[51] Sunwoo Han, Ju-Hyeon Shin, Pil-Hoon Jung, Heon Lee, and Bong Jae Lee. Broadband solar thermal absorber based on optical metamaterials for high-temperature applications. *Advanced Optical Materials*, 4(8):1265–1273, 2016.

[52] Manohar Chirumamilla, Alexander S. Roberts, Fei Ding, Deyong Wang, Peter Kjær Kristensen, Sergey I Bozhevolnyi, and Kjeld Pedersen. Multilayer tungsten-alumina-based broadband light absorbers for high-temperature applications. *Optical Materials Express*, 6(8):2704–2714, 2016.

[53] Pavel N. Dyachenko, J.J. do Rosário, E.W. Leib, A. Yu Petrov, Michael Störmer, Horst Weller, Tobias Vossmeyer, Gerold A Schneider, and Manfred Eich. Tungsten band edge absorber/emitter based on a monolayer of ceramic microspheres. *Optics express*, 23(19):A1236–A1244, 2015.

[54] Jeffrey B. Chou, Yi Xiang Yeng, Yoonkyung E. Lee, Andrej Lenert, Veronika Rinnerbauer, Ivan Celanovic, Marin Soljačić, Nicholas X.

Fang, Evelyn N. Wang, and Sang-Gook Kim. Enabling ideal selective solar absorption with 2D metallic dielectric photonic crystals. *Advanced Materials*, 26(47):8041–8045, 2014.

[55] Veronika Stelmakh, Walker R. Chan, Michael Ghebrebrhan, Jay Senkevich, John D. Joannopoulos, Marin Soljačić, and Ivan Celanović. Sputtered tantalum photonic crystal coatings for high-temperature energy conversion applications. *IEEE Transactions on Nanotechnology*, 15(2):303–309, 2016.

[56] Veronika Stelmakh, Veronika Rinnerbauer, John D. Joannopoulos, Marin Soljačić, Ivan Celanovic, Jay J. Senkevich, Charles Tucker, Thomas Ives, and Ronney Shrader. Evolution of sputtered tungsten coatings at high temperature. *Journal of Vacuum Science & Technology A: Vacuum, Surfaces, and Films*, 31(6):061505, 2013.

[57] Manohar Chirumamilla, Gnanavel Vaidhyanathan Krishnamurthy, Surya Snata Rout, Martin Ritter, Michael Störmer, Alexander Yu Petrov, and Manfred Eich. Thermal stability of tungsten based metamaterial emitter under medium vacuum and inert gas conditions. *Scientific reports*, 10(1):1–10, 2020.

[58] Gnanavel Vaidhyanathan Krishnamurthy, Manohar Chirumamilla, Surya Snata Rout, Kaline P Furlan, Tobias Krekeler, Martin Ritter, Hans-Werner Becker, Alexander Yu Petrov, Manfred Eich, and Michael Störmer. Structural degradation of tungsten sandwiched in hafnia layers determined by in-situ xrd up to 1520 °C. *Scientific reports*, 11(1):1–12, 2021.

[59] M. Ohring. *Materials Science of Thin Films*. Elsevier Science, 2001.

[60] D.L. Smith and Hoffman D.W. *Thin-Film Deposition: Principles and Practice*. McGraw-Hill Education, 1995.

[61] E. Ashworth Underwood. Wilhelm conrad röntgen (1845–1923) and the early development of radiology. *Proceedings of the Royal Society of Medicine*, 38(12):697–706, 1945.

[62] M. Eckert. Max von Laue and the discovery of x-ray diffraction in 1912. *Annalen der Physik*, 524(5):A83–A85, 2012.

[63] B.D. Cullity. *Elements of X-ray Diffraction*. Addison-Wesley metallurgy series. Addison-Wesley Publishing Company, 1956.

[64] H.P. Klug and L.E. Alexander. *X-ray Diffraction Procedures for Polycrystalline and Amorphous Materials*. Wiley, 1954.

[65] J Il Langford and AJC Wilson. Scherrer after sixty years: a survey and some new results in the determination of crystallite size. *Journal of applied crystallography*, 11(2):102–113, 1978.

[66] C. Suryanarayana and M.G. Norton. *X-Ray Diffraction: A Practical Approach*. Artech House Telecommunications. Springer US, 1998.

[67] Frank Smith. *Industrial applications of X-ray diffraction*. CRC press, 1999.

[68] P. Ramminger, R. Tessadri, R. Krismer, and P. Wilhartitz. Application of high temperature x-ray diffraction as a tool for material characterization and product optimization. 2001.

[69] Harald Ibach and Hans Lüth. *Solid-state physics: an introduction to theory and experiment*. Springer Science & Business Media, 2012.

[70] Charles Kittel and John Wiley. *Elementary solid state physics: A short course*. Wiley, 1962.

[71] Andrew Jones Andreas Pein, Barbara Puhr. *Principles of non-ambient X-ray diffraction*. Anton Paar GmbH, 2018.

[72] Alan A. Coelho. Topas and topas-academic: an optimization program integrating computer algebra and crystallographic objects written in c++. *Journal of Applied Crystallography*, 51(1):210–218, 2018.

[73] Lyman G. Parratt. Surface studies of solids by total reflection of x-rays. *Physical Review*, 95(2):359, 1954.

[74] David Attwood. *Soft X-Rays and Extreme Ultraviolet Radiation: Principles and Applications*. Cambridge University Press, 1999.

[75] Manfred R Schuster, H Göbel, Lutz Brügemann, D Bahr, F Burgäzy, Carsten Michaelsen, Michael Störmer, P Ricardo, Reiner Dietsch,

Thomas Holz, et al. Laterally graded multilayer optics for x-ray analysis. In *EUV, X-Ray, and Neutron Optics and Sources*, volume 3767, pages 183–198. SPIE, 1999.

[76] Masahiro Tosa. *Surface Profilometer*, pages 679–682. Springer Singapore, Singapore, 2018.

[77] Erik Lassner and Wolf-Dieter Schubert. Properties, chemistry, technology of the element, alloys, and chemical compounds. *Vienna University of Technology, Vienna, Austria, Kluwer*, pages 124–125, 1999.

[78] J.P. Hiernaut, R. Beukers, M. Hoch, T. Matsui, and R.W. Ohse. Determination of the melting point and of the spectral and total emissivities of tungsten, tantalum, and molybdenum in the solid and liquid states with a six-wavelength pyrometer. *High Temperatures. High Pressures (Print)*, 18(6):627–633, 1986.

[79] K. Salamon, O. Milat, N. Radić, P. Dubček, M. Jerčinović, and S. Bernstorff. Structure and morphology of magnetron sputtered w films studied by x-ray methods. *Journal of Physics D: Applied Physics*, 46(9):095304, 2013.

[80] K. Bouziane, M. Mamor, and F. Meyer. Dc magnetron sputtered tungsten: W film properties and electrical properties of W/Si Schottky diodes. *Applied Physics A*, 81(1):209–215, 2005.

[81] Nuria Gordillo, Miguel Panizo-Laiz, E. Tejado, Iván Fernández-Martínez, A. Rivera, José Y. Pastor, C. Gómez de Castro, J. del Rio, J.M. Perlado, and Raquel Gonzalez-Arrabal. Morphological and microstructural characterization of nanostructured pure α-phase W coatings on a wide thickness range. *Applied Surface Science*, 316:1–8, 2014.

[82] F.T.N. Vüllers and Ralph Spolenak. Alpha-vs. beta-tungsten nanocrystalline thin films: A comprehensive study of sputter parameters and resulting materials' properties. *Thin Solid Films*, 577:26–34, 2015.

[83] M.J. O'keefe and J.T. Grant. Phase transformation of sputter deposited tungsten thin films with a-15 structure. *Journal of applied physics*, 79(12):9134–9141, 1996.

[84] Stacy Gates-Rector and Thomas Blanton. The powder diffraction file: a quality materials characterization database. *Powder Diffraction*, 34(4):352–360, 2019.

[85] P. Petroff, T.T. Sheng, A.K. Sinha, G.A. Rozgonyi, and F.B. Alexander. Microstructure, growth, resistivity, and stresses in thin tungsten films deposited by rf sputtering. *Journal of Applied Physics*, 44(6):2545–2554, 1973.

[86] Y.G. Shen, Y.W. Mai, Q.C. Zhang, D.R. McKenzie, W.D. McFall, and W.E. McBride. Residual stress, microstructure, and structure of tungsten thin films deposited by magnetron sputtering. *Journal of Applied Physics*, 87(1):177–187, 2000.

[87] K.L. Chopra, M.R. Randlett, and R.H. Duff. Face-centered-cubic tungsten films obtained by. *Applied Physics Letters*, 9(11):402–405, 1966.

[88] S. Basavaiah and S.R. Pollack. Superconductivity in β-tungsten films. *Journal of Applied Physics*, 39(12):5548–5556, 1968.

[89] K.L. Chopra, M.R. Randlett, and R.H. Duff. Face-centred cubic modification in sputtered films of tantalum, molybdenum, tungsten, rhenium, hafnium and zirconium. *Philosophical Magazine*, 16(140):261–273, 1967.

[90] John A. Thornton. Influence of apparatus geometry and deposition conditions on the structure and topography of thick sputtered coatings. *Journal of Vacuum Science and Technology*, 11(4):666–670, 1974.

[91] B. Hertel and J. Diehl. On the formation of vacancy clusters in copper irradiated with 5 keV argon ions. *physica status solidi (a)*, 33(2):K73–K75, 1976.

[92] F.M. d'Heurle and J.M.E. Harper. Note on the origin of intrinsic stresses in films deposited via evaporation and sputtering. *Thin Solid Films*, 171(1):81–92, 1989.

[93] Mary F. Doerner and William D. Nix. Stresses and deformation processes in thin films on substrates. *Critical Reviews in Solid State and Material Sciences*, 14(3):225–268, 1988.

[94] C.A. Davis. A simple model for the formation of compressive stress in thin films by ion bombardment. *Thin solid films*, 226(1):30–34, 1993.

[95] I.A. El-Shanshoury, V.A. Rudenko, and I.A. Ibrahim. Polymorphic behavior of thin evaporated films of zirconium and hafnium oxides. *Journal of the American Ceramic Society*, 53(5):264–268, 1970.

[96] John Huminik. *High-temperature inorganic coatings*. Reinhold Publishing Corporation, 1963.

[97] P.J. Spencer, von Goldbeck, et al. Hafnium: physico-chemical properties of its compounds and alloys. 1981.

[98] Frank H Chung and Richard W Scott. A new approach to the determination of crystallinity of polymers by x-ray diffraction. *Journal of Applied Crystallography*, 6(3):225–230, 1973.

[99] N. T. Wakelyn and P. R. Young. Crystallinity index of poly(ethylene terephthalate) by x-ray diffractometry and differential scanning calorimetry. *Journal of Applied Polymer Science*, 10(10):1421–1438, 1966.

[100] Per Kofstad. High temperature corrosion((book)). *London and New York, Elsevier Applied Science, 1988, 568*, 1988.

[101] H.A. Wriedt. The O-W (oxygen-tungsten) system. *Bulletin of Alloy phase diagrams*, 10(4):368–384, 1989.

[102] I. Barin and G. Platzki. *Thermochemical Data of Pure Substances, Thermochemical Data of Pure Substances*. Thermochemical Data of Pure Substances. Wiley, 1995.

[103] Sergey V. Ushakov, Alexandra Navrotsky, Y. Yang, Susanne Stemmer, Kaupo Kukli, Mikko Ritala, MA Leskelä, Peter Fejes, Alex Demkov, Cathy Wang, et al. Crystallization in hafnia-and zirconia-based systems. *physica status solidi (b)*, 241(10):2268–2278, 2004.

[104] Chao Zhao, Vincent Cosnier, P.J. Chen, Olivier Richard, Gert Roebben, Jan Maes, Sven Van Elshocht, Hugo Bender, Edward Young, Omer Van der Biest, et al. Thermal stability of high k layers. *MRS Online Proceedings Library (OPL)*, 745, 2002.

[105] Y.S. Touloukian and D.P. DeWitt. Thermophysical properties of matter-The TPRC data series. Volume 8. Thermal radiative properties-nonmetallic solids. Technical report, Thermophysical and electronic properties information analysis centre, 1972.

[106] Milton Ohring. Chapter 4—discharges, plasmas, and ion–surface interactions. *Materials Science of Thin Films*, pages 145–202, 2002.

[107] E.J. Mittemeijer and P. Scardi. *Diffraction Analysis of the Microstructure of Materials*. Springer Series in Materials Science. Springer Berlin Heidelberg, 2003.

[108] C.G. Bergeron, V.J. Tennery, and A.L. Friedberg. Reaction studies of ceramic-coated tungsten. *Journal of the American Ceramic Society*, 44(4):156–160, 1961.

[109] J Lou, BJ Ye, HM Weng, HJ Du, ZB Wang, and XP Wang. The influence of filament temperature and oxygen concentration on tungsten oxide nanostructures by hot filament metal oxide deposition. *Journal of Physics D: Applied Physics*, 41(15):155410, 2008.

[110] Earl A. Gulbransen and W.S. Wysong. Thin oxide films on aluminum. *The Journal of Physical Chemistry*, 51(5):1087–1103, 1947.

[111] E.A. Gulbransen and K.F. Andrew. Kinetics of the oxidation of pure tungsten from 500 ° C to 1300 ° C. *Journal of the Electrochemical Society*, 107(7):619, 1960.

[112] E.A. Gulbransen, K.F Andrew, and F.A. Brassart. Kinetics of oxidation of pure tungsten, 1150 ° C -1615 °C. *Journal of the Electrochemical Society*, 111(1):103, 1964.

[113] H.U. Anderson. Kinetic studies of the reactions occurring between tungsten and gases at low pressure and high temperatures (thesis). Technical report, California Univ., Berkeley, CA (US). Lawrence Radiation Lab., 1962.

[114] J.A. Becker, E.J. Becker, and Re G. Brandes. Reactions of oxygen with pure tungsten and tungsten containing carbon. *Journal of Applied Physics*, 32(3):411–423, 1961.

[115] Harland G. Tompkins. *A user's guide to ellipsometry*. Courier Corporation, 2006.

[116] J.H. Singleton. Interaction of oxygen with hot tungsten. *The Journal of Chemical Physics*, 45(8):2819–2826, 1966.

[117] P.O. Schissel and O.C. Trulson. Mass-spectrometric study of the oxidation of tungsten. *The Journal of Chemical Physics*, 43(2):737–743, 1965.

[118] R.J. Ackermann, E.G. Rauh, R.J. Thorn, and M.C. Cannon. A thermodynamic study of the thorium - oxygen system at high temperatures1. *The Journal of Physical Chemistry*, 67(4):762–769, 1963.

[119] Ryan P. Haggerty, Pankaj Sarin, Zlatomir D. Apostolov, Patrick E. Driemeyer, and Waltraud M. Kriven. Thermal expansion of HfO_2 and ZrO_2. *Journal of the American Ceramic Society*, 97(7):2213–2222, 2014.

[120] L.B. Hunt. A history of iridium. *Platinum Metals Review*, 31(1):32–41, 1987.

[121] Dwight. E. Gray. American institute of physics handbook. *American Journal of Physics*, 32(5):389–389, 1964.

[122] P. Atkins and L. Jones. *Chemical Principles: The Quest for Insight*. W. H. Freeman, 2007.

[123] Shuxin Bai, Hong Zhang, Yicong Ye, Wei Gao, et al. Long-term high-temperature oxidation of iridium coated rhenium by electrical resistance heating method. *International Journal of Refractory Metals and Hard Materials*, 44:42–48, 2014.

[124] EHP Cordfunke and G Meyer. The system Iridium-Oxygen i. Measurements on the volatile oxide of Iridium. *Recueil des Travaux Chimiques des Pays-Bas*, 81(6):495–504, 1962.

[125] R. Ted Wimber and Hal G. Kraus. Oxidation of iridium. *Metallurgical and Materials Transactions B*, 5(7):1565–1571, 1974.

[126] Dean E. Peterson. Thermodynamics and transport of gaseous iridium oxides in multi-hundred-watt thermoelectric generators. Technical report, Los Alamos Scientific Lab., N. Mex.(USA), 1976.

[127] E.H.P. Cordfunke. The enthalpy of formation of IrO_2 and thermodynamic functions. *Thermochimica Acta*, 50(1-3):177–185, 1981.

[128] Hermann Jehn. High temperature behaviour of platinum group metals in oxidizing atmospheres. *Journal of the Less Common Metals*, 100:321–339, 1984.

[129] Hugh St. C. O'Neill and Johan Nell. Gibbs free energies of formation of Ruo_2, Iro_2, and OsO_2: A high-temperature electrochemical and calorimetric study. *Geochimica et Cosmochimica Acta*, 61(24):5279–5293, 1997.

[130] Sandeep Kohli, David Niles, Christopher D. Rithner, and Peter K. Dorhout. Structural and optical properties of Iridium films annealed in air. *JCPDS-International Centre for Diffraction Data, Advances in X-ray Analysis*, 45:352–358, 2002.

[131] Yuxue Liu, Hiroshi Masumoto, and Takashi Goto. Preparation of IrO_2 thin films by oxidating laser-ablated Ir. *Materials Transactions*, 45(3):900–903, 2004.

[132] Babu R. Chalamala, Yi Wei, Robert H. Reuss, Sanjeev Aggarwal, Bruce E. Gnade, R. Ramesh, John M. Bernhard, Edward D. Sosa, and David E. Golden. Effect of growth conditions on surface morphology and photoelectric work function characteristics of iridium oxide thin films. *Applied Physics Letters*, 74(10):1394–1396, 1999.

[133] H. Alex Hsain, Younghwan Lee, Gregory Parsons, and Jacob L. Jones. Compositional dependence of crystallization temperatures and phase evolution in hafnia-zirconia (Hf_xZr_{1-x}) O_2 thin films. *Applied Physics Letters*, 116(19):192901, 2020.

[134] Shigehisa Shibayama, Tomonori Nishimura, Shinji Migita, and Akira Toriumi. Thermodynamic control of ferroelectric-phase formation in Hf $_x$ Zr_{1-x} O_2 and ZrO_2. *Journal of Applied Physics*, 124(18):184101, 2018.

[135] Richard W. Siegel. Cluster-assembled nanophase materials. *Annual Review of Materials Science*, 21(1):559–578, 1991.

[136] Mohammad Delower Hossain, Trent Borman, Corey Oses, Marco Esters, Cormac Toher, Lun Feng, Abinash Kumar, William G Fahrenholtz, Stefano Curtarolo, Donald Brenner, et al. Entropy landscaping of high-entropy carbides. *Advanced Materials*, 33(42):2102904, 2021.

[137] David Turnbull. Metastable structures in metallurgy. *Metallurgical Transactions B*, 12(2):217–230, 1981.

[138] Carl V. Thompson. Solid-state dewetting of thin films. *Annual Review of Materials Research*, 42:399–434, 2012.

[139] Omar Elmazria and Thierry Aubert. Wireless saw sensor for high temperature applications: Material point of view. In *Smart Sensors, Actuators, and MEMS V*, volume 8066, page 806602. International Society for Optics and Photonics, 2011.

[140] Two-dimensional and three-dimensional vortex lattice dynamics in DyBa $_2$ Cu $_3$ O $_7$(Y $_{1-x}$ Pr x) Ba $_2$ Cu $_3$ O $_7$ coupled heterostructures, author=Triscone, J.M and Fivat, Patrice and Andersson, Magnus and Decroux, Michel and others, journal=Physical Review B, volume=50, number=2, pages=1229, year=1994, publisher=APS.

[141] Jay A. Switzer, James C. Hill, Naveen K. Mahenderkar, and Ying-Chau Liu. Nanometer-thick gold on silicon as a proxy for single-crystal gold for the electrodeposition of epitaxial cuprous oxide thin films. *ACS Applied Materials & Interfaces*, 8(24):15828–15837, 2016.

Appendix A

Thermal validation of various materials

A.1 W- strip

W has a bcc (body centered) cubic structure. Therefore it is required to calculate only a single lattice parameter. The lattice parameter of bulk W is a = 0.31648 nm (PDF 00 -004 -08061). The thermal expansion W required for calibration in two different temperature ranges is extracted from literature can be calculated using equation A.1 and A.2 [105].

$$\frac{\Delta a}{a_0} = 4.266 \times 10^{-4}(T - 293) + 8.479 \times 10^{-8}(T - 293)^2 - 1.974 \times 10^{-11}(T - 293)^3 \tag{A.1}$$

(293 <T < 1395)

$$\frac{\Delta a}{a_0} = 0.548 + 5.416 \times 10^{-4}(T - 1395) + 1.952 \times 10^{-8}(T - 1395)^2 + 4.422 \times 10^{-11}(T - 1395)^3 \quad (A.2)$$

(1395 <T < 2495)

T / K	T / °C	$\frac{a-a_0}{a_0}$ / %	$\frac{a-a_0}{a_0}$/ 100	($\frac{a-a_0}{a_0}$/ 100)+1	(($\frac{a-a_0}{a_0}$/ 100)+1)a_0 / nm
293	20	0	0	1	0.31648
400	127	0.048	0.00048	1.00048	0.31663
500	227	0.093	0.00093	1.00093	0.31677
600	327	0.014	0.0014	1.0014	0.31692
700	427	0.188	0.00188	1.00188	0.31707
800	527	0.237	0.00237	1.00237	0.3172
900	627	0.287	0.00287	1.00237	0.31738
1000	727	0.339	0.00339	1.00339	0.31755
1200	927	0.444	0.00444	1.00444	0.31788
1400	1127	0.551	0.00551	1.00551	0.31822
1600	1327	0.661	0.00661	1.00661	0.31857
1800	1527	0.774	0.00774	1.00774	0.3189
2000	1727	0.893	0.00893	1.00893	0.31930
2200	1927	1.02	0.0102	1.0102	0.31970
2400	2127	1.157	0.0115	1.0115	0.32014

Table A.1: Calculated lattice parameter for thermal expansion of W

- The first step in the temperature validation process is to obtain a calculated lattice parameter 'a' as a function of temperature in Kelvin, and is calculated using the equation A.1 and A.2 are shown in the 2nd column of Table A.1.

- The 4th column is then added by 1. The value one comes from the derivation below.

$$\Delta a = a - a_0$$

$$\frac{\Delta a}{a_0} \times a_0 = a - a_0 \text{ (Multiplying and diving left side by } a_0\text{)}$$

$$a = a_0 + \left(\frac{\Delta a}{a_0}\right) \times a_0$$

$$a = a_0 \times \left(1 + \frac{\Delta a}{a_0}\right)$$

- Column 5 is multiplied by the lattice parameter of bulk W at room temperature $a_0 = 3.1648$ nm. The plot of calculated lattice parameter 'a' as a function of temperature is shown in Figure A1
- An inverse expansion function is calculated from the above plot, equation A.3

$$F^{-1}(T) = -184260 + 58158.9a - 0.000132249a^2 + 1.381 \times 10^{-5}a^3 \quad \text{(A.3)}$$

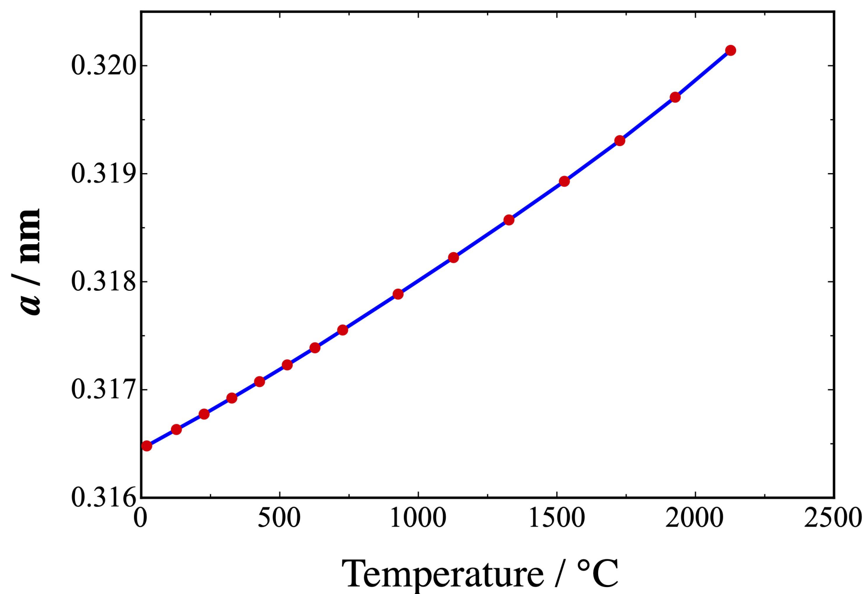

Figure A1: W lattice parameter as a function of Temperature

The second step in the temperature validation is for the experimental part. The vacuum chamber containing the W-strip is pumped down to a pressure less than 3×10^{-6} mbar. The Z-stage is aligned to the 2θ position 35.5° of (200) tungsten peak (PDF 00-004-0806 (tungsten)). The temperature is increased from 25°C up to 2000°C with a heating rate of 120° C min^{-1}. At every 100°C interval, a diffractogram was recorded from 20° to 120° with a step size of 0.02° and 0.1 s for each step. Rietveld refinement was done using TOPAS Bruker software on all the recorded diffractograms.

Apparent Temp. / °C	Rietveld (a) / nm	Actual Temp °C
25	0.3167	31
200	0.3169	53
400	0.3171	176
600	0.3173	357
800	0.3175	547
1000	0.3177	745
1200	0.3179	949
1400	0.3180	1163
1600	0.3183	1391
1800	0.3188	1639
2000	0.3192	1887

Table A.2: W lattice parameters calculated by Rietveld refinement and the actual temperature calculated by the inverse expansion curve

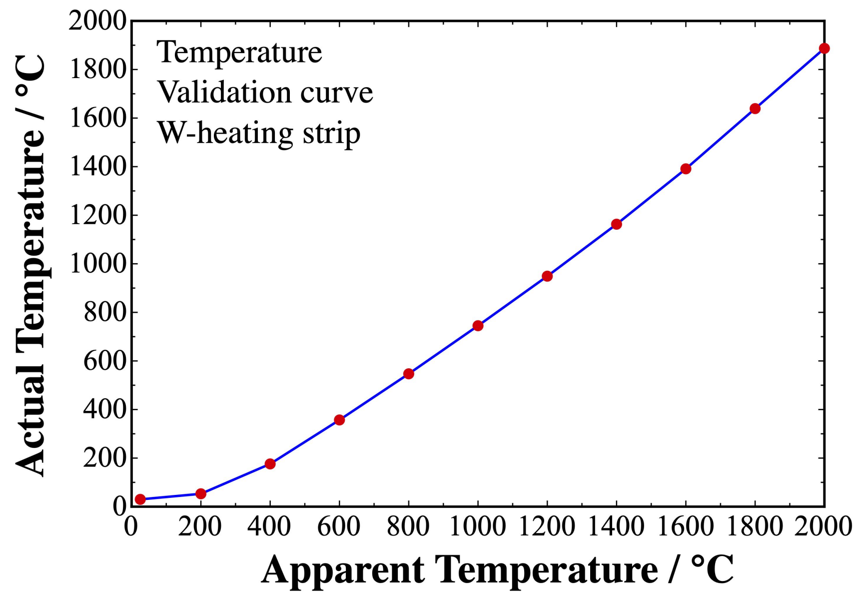

Figure A2: Actual temperature versus controller apparent temperature of W heating strip.

The refined lattice parameters (Table A.2) are plugged in equation A.3 to obtain the real temperature of the W-strip. The desired output, actual temperature as a function of apparent temperature, is shown in Figure A2.

A.2 MgO substrate

Similar to W, MgO also has a cubic structure. The whole process of temperature validation is identical to that of W. The z-stage of the diffractometer is aligned according to the peak positions in PDF 00-45-946. The lattice parameters are calculated using equation A.5, and the values are tabulated in Table A.3 and the lattice parameter of bulk MgO is 0.42112 nm (PDF 00-45-946). By fitting the points between the calculated lattice parameters and temperature, the inverse thermal expansion function can be calculated as in equation A.5 [105].

$$\begin{aligned}\frac{\Delta a}{a_0} = & -0.326 + 1.040 \times 10^{-3}(T) + 2.581 \times 10^{-7}(T)^2 \\ & -2.834 \times 10^{-11}(T)^3\end{aligned} \tag{A.4}$$

Annealing experiments were done on 10 cm × 10 cm × 0.5 cm thick MgO substrate at a pressure less than 3×10^{-6} mbar from 25 °C up to 1400 °C. Diffractograms were recorded at every 200 °C, and the data was refined using the Rietveld method. The refined lattice parameters are shown in Table A.4, and the actual temperature (Figure A3) is evaluated by plugging in the values in equation A.5.

T / K	T / °C	$\frac{a-a_0}{a_0}$ / %	$\frac{a-a_0}{a_0}$ / 100	$(\frac{a-a_0}{a_0}$ / 100)+1	$((\frac{a-a_0}{a_0}$ / 100)+1)a_0 / nm
293	25	0	0	1	0.4211
473	200	0.22067	0.0022067	1.00221	0.4220
673	400	0.48218	0.0048218	1.00482	0.4231
873	600	0.75977	0.0075977	1.00760	0.4243
1073	800	1.05207	0.01052	1.01052	0.4255
1273	1000	1.35772	0.01358	1.01358	0.4268
1473	1200	1.67535	0.01675	1.01675	0.4282
1673	1400	2.00362	0.02004	1.02004	0.4295

Table A.3: Calculated lattice parameter for thermal expansion of MgO

$$F^{-1}(T) = -1.79 \times 10^7 + 1.246 \times 10^7 a - 2.89 \times 10^6 a^2 + 224240 a^3 \quad \text{(A.5)}$$

ApparentTemp. / °C	Rietveld (a) / nm	Actual Temp °C
25	0.4211	30
200	0.4213	51
400	0.4214	70
600	0.4215	392
800	0.4217	128
1000	0.4220	185
1200	0.4223	251
1400	0.4250	720

Table A.4: MgO lattice parameters calculated by Rietveld refinement and the actual temperature calculated by the inverse expansion curve

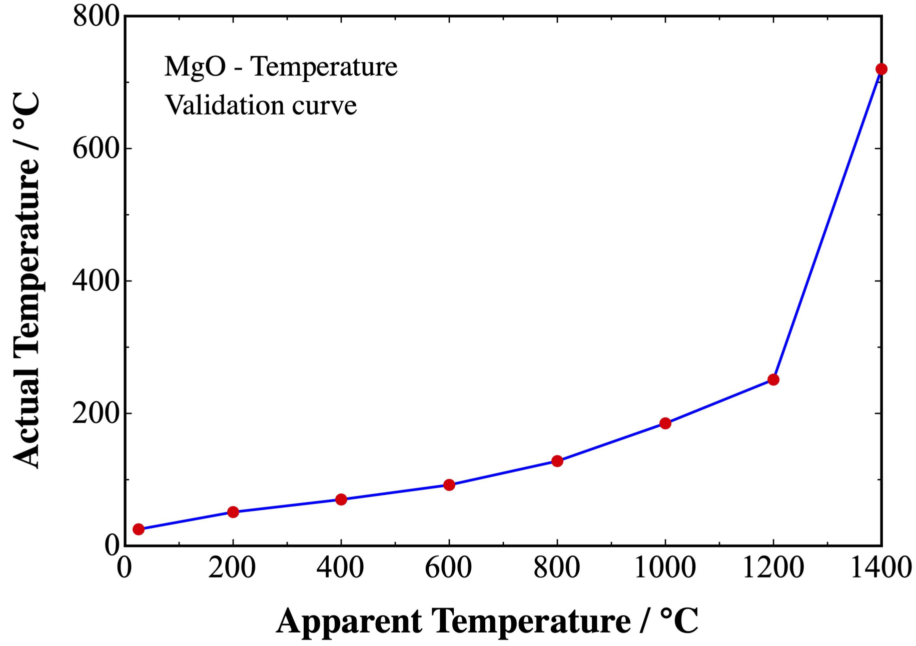

Figure A3: Actual temperature versus controller apparent temperature of MgO substrate

A.3 Sapphire substrate (Al_2O_3)

Unlike W and MgO, sapphire has a hexagonal crystal structure and exhibits anisotropic properties. Therefore the thermal expansion should be verified for two lattice parameters, 'a' and 'c.' The thermal expansion along the 'a' and 'c' directions are calculated using equations A.6 and A.7 [105].

$$\begin{aligned}\frac{\Delta a}{a_0} = & -0.176 + 5.431 \times 10^{-4}(T) + 2.150 \times 10^{-7}(T)^2 \\ & -2.810 \times 10^{-11}(T)^3\end{aligned} \tag{A.6}$$

$$\frac{\Delta c}{c_0} = -0.192 + 5.927 \times 10^{-4}(T) + 2.142 \times 10^{-7}(T)^2 - 2.207 \times 10^{-11}(T)^3 \tag{A.7}$$

The calculated values are tabulated in Table A.5. However, unlike W or MgO, the temperature cannot be directly evaluated from the lattice parameter due to anisotropy in thermal expansion. Therefore, the 2θ peak position for a high angle peak (036) is calculated as a function of temperature from the following expression.

$$\frac{1}{d^2} = \frac{4}{3}\left(\frac{h^2 + kh + k^2}{a^2}\right) + \left(\frac{l^2}{c^2}\right) \tag{A.8}$$

The calculated 2θ as a function is shown in Figure A4. Using the latter plot, the inverse expansion function for sapphire is generated, shown in equation A.9.

Annealing experiments were done on 10 cm × 10 cm × 0.5 cm r-cut sapphire substrates having the orientation (1-102). The z-stage of the diffractometer is aligned according to the peak positions in PDF 01-82-1467. The equilibrium lattice parameter values are $a_0 = 0.4763$ nm and $c_0 = 1.3003$ nm (Crystec data sheet). The substrate was heated from 25 °C up to 1600 °C with a heating rate of 120 °C. At every 200 °C interval, a diffractogram was recorded from 20 °C to 130 °C with a step size of 0.02° and 0.1 s for each step. A full pattern fit was done on all the measured diffractograms and the lattice parameter 'a' and 'c' were refined are shown in Table A.6. Due to

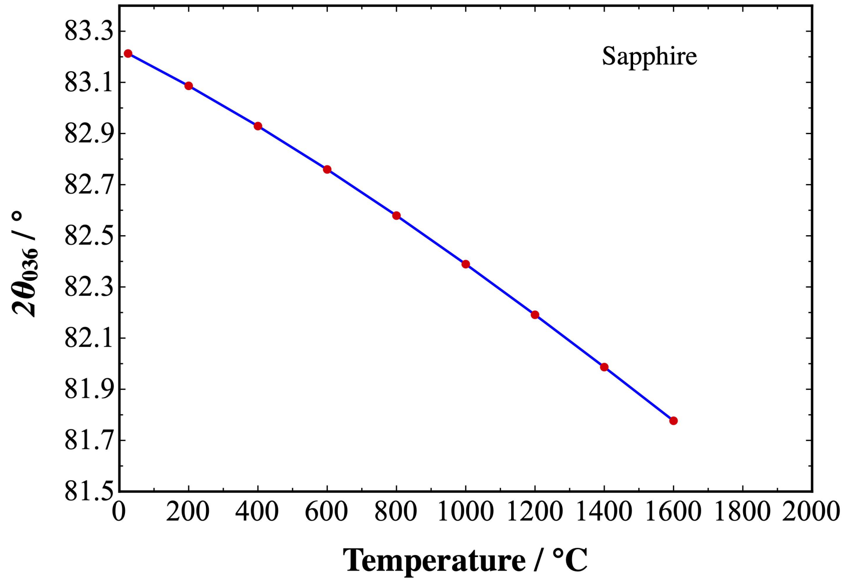

Figure A4: Temperature versus $2\theta_{036}$ of sapphire substrate

fluctuation in lattice parameter 'c', 2θ values were plugged in equation A.9 to determine the actual temperature.

$$F^{-1}(T) = 3.417 \times 10^7 - 1.25 \times 10^6 a + 15330.5 \times 10^6 a^2 - 62.56 a^3 \quad \text{(A.9)}$$

A plot of the actual temperature as a function of apparent temperature is shown in Figure A5. At 1600 °C, there is a difference of 555 °C between the apparent temperature and the actual temperature. There are a couple of factors that are to be considered during temperature validation. One among them is the pressure at which the validation is done. For direct strip heaters, the temperature deviation between the substrate surface and the thermocouple spot weld is the highest under vacuum as the heat transfer by

convection is missing.

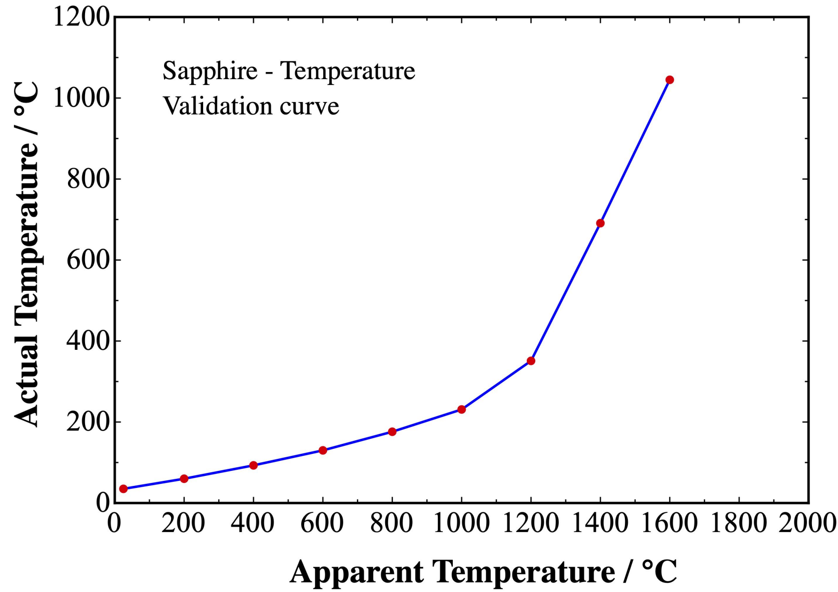

Figure A5: Actual temperature versus controller apparent temperature of sapphire substrate

The thermal conductivity of He (5.193 kJ kg$^{-1}K^{-1}$) is greater than N_2 (1.040 kJ kg$^{-1}K^{-1}$), therefore to minimize the temperature deviation, annealing measurements can be done in the He environment. In this work, all annealing experiments are performed at high vacuum conditions. It is good to perform temperature validation in similar conditions as the experiment to obtain better results. Another essential factor that influences the temperature deviation is the substrate thickness. Substrates having minimum thickness are recommended to minimize temperature deviation. Holes in the sample, poor or non-homogeneous contact of the sample with the heating

strip also impact the heat transfer and should be considered before performing experiments.

T / K	T / °C	$\frac{\left(\frac{a-a_0}{a_0}\right)}{100}$	$\left(\left(\frac{\left(\frac{a-a_0}{a_0}\right)}{100}\right)+1\right) a_0$ / nm	$\frac{\left(\frac{c-c_0}{c_0}\right)}{100}$	$\left(\left(\frac{\left(\frac{c-c_0}{c_0}\right)}{100}\right)+1\right) c_0$ / nm	$2\theta_{036}$
298	25	0.0000419	0.4758	0.0000306	1.2993	83.212
473	200	0.00126	0.4764	0.00134	1.3010	83.086
673	400	0.00278	0.4771	0.00297	1.3031	82.929
873	600	0.00443	0.4779	0.00474	1.3054	82.759
1073	800	0.00620	0.4788	0.00663	1.3079	82.579
1273	1000	0.00806	0.4797	0.00864	1.3105	82.389
1473	1200	0.01001	0.4806	0.01075	1.3132	82.191
1673	1400	0.01203	0.4815	0.01296	1.3161	81.986
1873	1600	0.01411	0.4825	0.01525	1.3190	81.776

Table A.5: Calculated lattice parameter for thermal expansion of sapphire substrate.

Apparent Temp. / °C	Rietveld (a) / nm	Rietveld (c) / nm	2θ / °	Actual Temp °C
25	0.4759	1.2997	83.203	35
200	0.4757	1.3013	83.189	60
400	0.4760	1.3002	83.165	93
600	0.4763	1.2997	83.138	130
800	0.4763	1.3011	83.102	176
1000	0.4767	1.3004	83.060	231
1200	0.4769	1.3035	82.966	351
1400	0.4785	1.3052	82.678	691
1600	0.4801	1.3096	82.345	1045

Table A.6: Sapphire $2\theta_{036}$ calculated from Rietveld refinement and the actual temperature calculated by the inverse expansion curve.

List of Tables

2.1 Equipment details used for annealing experiments. 21

3.1 Simulated XRR thickness and roughness of 20 nm W films. The experimental error of thickness determination is ± 0.5 nm. 42

3.2 Simulated XRR thickness and roughness of HfO_2 films. The experimental error of thickness determination is ± 0.5 nm. . . 47

4.1 Simulated XRR thickness and roughness of 30 nm Ir and 100 nm HfO_2 films. The experimental error of thickness determination is ± 0.5 nm. 98

4.2 Simulated parameters of the satellite peaks after annealing at different temperatures at 2 $\times 10^{-2}$ mbar for 6 h. 116

A.1 Calculated lattice parameter for thermal expansion of W . . . 144

A.2 W lattice parameters calculated by Rietveld refinement and the actual temperature calculated by the inverse expansion curve 147

A.3 Calculated lattice parameter for thermal expansion of MgO . . 149
A.4 MgO lattice parameters calculated by Rietveld refinement and the actual temperature calculated by the inverse expansion curve 149
A.5 Calculated lattice parameter for thermal expansion of sapphire substrate. 155
A.6 Sapphire $2\theta_{036}$ calculated from Rietveld refinement and the actual temperature calculated by the inverse expansion curve. 156

List of Figures

1.1 Potential waste heat recovery above 1000 °C (4 %) from the iron and steel industry in the UK during 2015 [2]. 10
1.2 Potential waste heat recovery above 1000 °C (3 %) from the glass, steel, aluminum and cement industry in the US during 2014 [3]. 11
1.3 Schematic of a thermophotovoltaic system (TPV). 13
1.4 (A) Peak maximum shifts towards lower wavelengths for higher temperatures shown according to Wien's displacement law. (B) Suppression of longer wavelengths by a selective emitter to enhance the efficiency of the TPV system. 13

2.1 (A) Sputtering facility at Hereon. (B) Schematic of the sputtering chamber. 19
2.2 Bragg condition required for diffraction of X-rays. 22
2.3 Important peak parameter in x-ray diffraction. Inset showing the longer range and all indexed peaks of a 160 nm thick W layer. 25
2.4 Cross section of an in-situ annealing chamber. 27
2.5 Total potential energy for interaction of pair of atoms as a function of interatomic distance. 30

3.1 X-ray diffractograms showing α and β phase of two separate 20 nm W films. All scans are background normalized. 39

3.2 X-ray reflectivity measured and simulated scans of two 20 nm containing α and β W. 40
3.3 (A) X-ray diffractograms of tungsten thin films with thickness 5 nm, 10 nm and 20 nm, normalized to the peak maximum. Diffractogram in pink is the scan of the uncoated sapphire substrate. (B) X-ray diffractograms of tungsten thin films with thickness 20 nm, 40 nm, 80 nm and 160 nm, normalized to the background. For reference purpose diffractogram of the 20 nm tungsten film is added in both of the plots. 43
3.4 Schematic explaining the effect of sputtering gas on the morphology of the film growth during sputtering. (A) At lower sputtering pressure, there are less gas atoms, therefore the mean free path is higher (lesser collisions) resulting in higher kinetic energy of the arriving atoms. The films grown under such conditions are more densified having a higher d-value ($d_c > d_{bulk}$) and the films are under compressive stress.(B) At higher sputtering pressure, there are more gas atoms, therefore the mean free path is lesser (more collisions) resulting in lower kinetic energy of the arriving atoms. The films grown under such conditions are less densified having a lower d-value ($d_t < d_{bulk}$) and the films are under tensile stress. 45
3.5 d-spacing versus Ar pressure in a 20 nm W layer. The data point shown in green is the bulk value of W at ambient pressure. 46
3.6 Phase diagram of hafnium-oxygen system showing the monoclinic phase at room temperature and the high temperature tetragonal and cubic phases [97]. 48
3.7 Layer thickness comparison between characterization methods - XRR and stylus profilometer for a single layer HfO_2. 49
3.8 XRR scans and XRD diffractograms of single layer HfO_2 having different film thickness. 50

3.9 Quantitative analysis of amorphous and nanocrystalline phase of a single layer HfO_2. 51

3.10 Schematic representation of a W-Metamatrial with HfO_2 dielectric interlayers and a top protective layer of HfO_2. 53

3.11 Phase diagram of W-O system. WO_3 has been identified by several names like tungsten oxide , tungsten(VI) oxide, tungstic oxide, tungsten trioxide, tungstic anhydride, tungstic acid, tungstite and α tungsten oxide. Most or all of these names were used before its polymorphism and non-symmetry transitions were known. Therefore the author [101] decided to arbitrarily denote the solid WO_3 variety occurring in equilibrium with liquid WO_3 by WO_3-A, WO_3-B, WO_3-C, and WO_3-D, each successive variety formed with falling temperature for which a report of evidence was found in literature. 55

3.12 Ex-situ diffractograms of W-metamaterial annealed in vacuum pressure of 2×10^{-2} mbar. The heating rate was 10 °C /min, holding time during isothermal annealing was 6 h and the cooling rate was 10 °C /min. All scans are normalized to the background. 57

3.13 Experimental spectral aborptivity/emissivity of the layered metamaterial emitter structures. Comparison of structures as-fabricated and after 6 h annealing at various temperatures at 2 $\times 10^{-2}$ mbar vacuum pressure. 58

3.14 A cross section STEM-EDS analysis to validate oxidation of W in a W-metamaterial after annealing at 1100 °C and 1200 °C. For comparison purpose an as-prepared metamaterial is also shown. STEM-HAADF images (a,e and i), W-M_α elemental mapping (b,f and j), Hf-M_α elemental mapping(c,g and k) and O-K_α elemental mapping(d,k and l). Presence of oxygen in the W layers are visible in (h and l) due to oxidation of W layers. 59

3.15 Ex-situ diffractograms of W-metamaterial annealed in vacuum pressure of 2×10^{-3} mbar. The heating rate was 10 °C /min, holding time during isothermal annealing was 6 h and the cooling rate was 10 °C /min. All scans are normalized to the background. 60
3.16 Cross section of a FIB- SEM image showing W metamaterial after annealing it at 1300 °C for 6 h at 2×10^{-3} mbar vacuum pressure. Absence of W or presence of holes in the W layer is seen due to sublimation of volatile tungsten oxide. 61
3.17 Ex-situ diffractograms of W-metamaterial annealed in vacuum pressure of 2×10^{-5} mbar. The heating rate was 10 °C /min, holding time during isothermal annealing was 6 h and the cooling rate was 10 °C /min. All scans are normalized to the background. 62
3.18 A cross section STEM-EDS showing degradation of W above 1450 °C . For comparison purpose an as-prepared metamaterial is also shown. STEM-HAADF images(a,e and i),W-M_α elemental mapping(b,f and j), Hf-M_α elemental mapping (c,g and k) and O-K_α elemental mapping (d,k and l). None of the tungsten layers are oxidized. Above 1400 °C the layered structure is lost, as W tries to form spheres in order to reduce interface free energy. 63

3.19 Ex-situ diffractograms of W-metamaterial (100 nm HfO_2 - Top layer /(30 nm -W / 100 nm - HfO_2)×6/ 200 nm - W bottom layer) annealed in Ar gas atmosphere. All scans are normalized to the background. The scan in orange is the W metamaterial (100 nm HfO_2 - Top layer /(20 nm -W / 100 nm - HfO_2)×6/ 200 nm - W bottom layer) annealed in a vacuum pressure of 2×10^{-6} mbar without any argon atmosphere, as for comparison purpose. Absence of WO_2 peaks is observed in all the scans. 65
3.20 SEM image of W-metamaterial annealed in Ar gas atmosphere at (a) 1300 °C for 6 h and (b) 1400 °C for 1 h [57]. 66
3.21 Schematic of the 3-layer-system used in the annealing experiment. A 3-layer-system is a sub-unit extracted from a multilayered metamaterial containing only a single metal layer sandwiched between two dielectric layers. 67
3.22 In-situ XRD diffractograms of a 3-layer-system from room temperature until 1520 °C at 3×10^{-6} mbar vacuum conditions. During this temperature increase (represented by thick blue line in the inset, which shows the whole annealing experiment) a tetragonal phase of HfO_2 appears around 200 °C and later slowly disappears above 800 °C. 69
3.23 In-situ X-ray diffraction measurements of a 3-layer-system performed during isothermal annealing at 1520 °C for 6 h at 3×10^{-6} mbar. The inset shows the whole annealing experiment with the isothermal part marked by a thick blue line. The (-111) peak of the monoclinic HfO_2 phase is unchanged, however, the (110) peak of the bcc W phase is decreased successively. The last diffractogram colored in brown is measured at room temperature, at the end of the annealing experiment. . . 71

3.24 Interplanar spacing d_{110} of bcc W in the 3-layer-system (A) as a function of temperature during annealing ramp and (B) as a function of time during isothermal annealing. Blue markers represent 650 °C and red markers represent 1520 °C. The duration of the isothermal part is 6 h. 73
3.25 Interplanar spacing d_{-111} of monoclinic HfO_2 in the 3-layer-system (A) as a function of temperature during annealing ramp and (B) as a function of time during isothermal annealing. Blue markers represent 650 °C and red markers represent 1520 °C. The duration of the isothermal part is 6 h. 73
3.26 Integrated intensity of (110) bcc W in 3-layer-systems annealed for 6 h at temperatures 650 °C (blue markers) and 1520 °C (red markers) (A) as a function of temperature during annealing ramp and (B) as a function of time during isothermal annealing. 75
3.27 Determined grain size values using the (110) bcc W peak (A) as a function of temperature during annealing ramp, and (B) as a function of time during isothermal annealing of the 3-layer-systems annealed for 6 h at 650 °C (blue markers) and 1520 °C (red markers) at 3×10^{-6} mbar. 77
3.28 Determined grain size values of (-111) monoclinic HfO_2 peak (A) as a function of temperature during annealing ramp, and (B) as a function of time during isothermal annealing of the 3-layer-systems annealed for 6 h at 650 °C (blue markers) and 1520 °C (red markers) at 3×10^{-6} mbar.(C) A SEM picture of the top HfO_2 layer of a 3-layer-system after annealing it at 1520 °C for 6 h, shows the grain size in the in-plane direction having an average grain size value of 75 nm. 78

3.29 STEM-EDS analysis of the 3-layer-system, as-prepared, annealed at 650 °C and 1520 °C for 6 h at 2 × 10^{-6} mbar. STEM-HAADF images (a-c), W-M_α elemental mapping (d-f), Hf-M_α elemental mapping (g-i). These images have the same scale as indicated in image (c). 79
3.30 (a) Morphology of the top HfO_2 layer with a void in the middle and (b) Cross section view along the interfaces across the same void (FIB section) after annealing it at 1520 °C for 40 h, at 3 × 10^{-6} mbar vacuum pressure. 80
3.31 XRD diffractogram of the vaporized constituents collected on a sapphire substrate in the chamber during the 40 h annealing experiment at 1520 °C, 3 × 10^{-6} mbar. 82
3.32 RBS spectra of the 3-layer-system as-prepared (green markers), annealed at 650 °C (blue markers), and 1520 °C (red markers). 83
3.33 Schematic explaining the oxidation mechanism of W at various temperature and pressure ranges. 85
3.34 SEM cross section of the 3-layer-system annealed at different temperatures for a period of 20 h. a) 300 °C, b) 650 °C, c) 800 °C, d) 1000 °C, e) 1240 °C, and f) 1520 °C. All the images have the same scale as indicated in image (a). 87
3.35 (A) Integrated intenstiy of (110)W peak in the 3-layer-system during isothermal annealing at 800 °C, 1000 °C, 1240 °C and 1520 °C for 20 h at 3 × 10^{-6} mbar vacuum pressure. The data point represented in filled dots are used for linear regression, the hollow dots are the remaining data points. (B) The change in volume fraction of W is represented as an Arrhenius plot used to calculate an activation energy of 1.2 eV for the oxidation process. 89

3.36 Mechanisms during annealing of a 3-layer-system up to 1520 °C: phase transformation and channel formation in the HfO_2 layers and the loss of W due to oxidation through the transport channels. 91

4.1 Shape of d-orbitals showing the presence of nodes [122]. 93
4.2 Comparison of ΔG_f as a function of temperature between IrO_2 and $WO_{2.7}$. 94
4.3 As prepared Ir films first forms an oxide (IrO_2 (s))layer above 600 °C, on further heating above 700 ° C the formed oxide sublimates (IrO_3 (g)) leaving fresh metal behind at 1 bar pressure. 95
4.4 Measured and simulated x-ray reflectivity (XRR) as a function of the scattering angle 2θ of as-prepared single 100 nm thick HfO_2 layer (blue), single 30 nm thick Ir layer (green), bilayer (30 nm Ir/100 nm HfO_2) (magenta), a 3-layer-system (100 nm HfO_2 / 30 nm Ir/100 nm HfO_2) (orange) prepared on a silicon substrate and each combination is simulated (dotted lines). On the right to the scans, schematics of a bilayer and 3-layer-system are shown. 97
4.5 In-situ XRD diffractograms of a 3-layer-system from room temperature up to 1000 °C represented in blue. Diffractograms in red represent isothermal annealing at 1000 °C for 6 h. The last scans in green is measured at room temperature at the end of the annealing experiment. The annealing experiment is performed in a vacuum pressure of 2×10^{-6} mbar. 99
4.6 X-ray diffractogram of a 3-layer-system between 20° - 38° after preparation. The (-111) peak at 28° belongs to the monoclinic phase and the broad bump at 31° belongs to the amorphous phase of HfO_2. 101

4.7 Measured interplanar spacings d_{111} fcc Ir as a function of temperature during annealing ramp (A) and as a function of time during isothermal annealing (B) in the 3-layer-system. After 24 h, slow cool-down transfers the samples back to room temperature (RT). 104
4.8 Measured grain size of fcc Iridium as a function of temperature during annealing ramp (A) and as a function of time during isothermal annealing (B) in the 3-layer-system; calculated from the FWHM of the (111) peak of the fcc Ir phase. 106
4.9 STEM-EDS analysis of the 3-layer-system, as-prepared, annealed at 1000 °C and 1100 °C for 6 h at 2×10^{-6} mbar. STEM-HAADF images (a-c), Ir-M_α elemental mapping (d-f), Hf-M_α elemental mapping (g-i), O-K_α elemental mapping (j-l).These images have the same scale as indicated in image (l). The top of the 3-layer-system is coated with Au in order to circumvent the effect of charging. 107
4.10 Measured grain size of fcc Iridium as a function of temperature during annealing ramp (A) and as a function of time during isothermal annealing (B) in the bilayer system; calculated from the FWHM of the (111) peak of the fcc Ir phase. 109
4.11 AFM images of (A) as-prepared morphology of Ir top layer (Bilayer- Ir/ HfO_2), (B) morphology of the same bilayer showing agglomeration of Ir into net like structures after annealing at 1000 °C for 6 h, (C) conductive AFM- showing flow of current from Ir areas and non-conducting parts from the HfO_2 layer (D) height profile of the bilayer before and after annealing. 110

4.12 Normalized diffraction patterns of a 3-layer-system measured at room temperature, after annealing it at 1000 °C for 6 h at different pressures. All scans in the plot are background normalized for comparison. 112

4.13 Diffraction pattern of a 3-layer-system ex-situ annealed at 1000 °C for 100 h at 2 $\times 10^{-2}$ mbar, the inset shows presence of higher order satellite peaks due to coherent scattering and sharp interfaces between the layers. 113

4.14 X-ray diffractograms of a 3-layer-system ex-situ annealed at different temperature at 2×10^{-2} mbar for 6 h. Only prominent peaks from (111)fcc Ir and (-111) monoclinic HfO_2 are visible. All scans are normalized to the background. 115

4.15 Higher order satellite peaks from the primary (111) fcc Ir Bragg peak from the 3-layer-system ex-situ annealed at different temperature for 6 h. Some of higher order peaks start to vanish above 1200 °C. All scans are normalized to the peak maximum. 116

4.16 (A) Normalized integrated intensity of (111) fcc Ir and (110) bcc W during isothermal annealing as a function of time annealed over 100 h at 1000 °C in a pressure of 2×10^{-2}mbar.(B-I) STEM-EDS analysis of the Ir/HfO_2 and W/HfO_2 metamaterial, as-prepared and annealed at 1000 °C for 100 h. (B and C) STEM-HAADF images of Ir/HfO_2 metamaterial, (D and E) Ir -M_α(green) and Hf -M_α (red) mix elemental mapping, (F and G) STEM-HAADF images of W/HfO_2 metamaterial , (H and I) W -M_α(blue) and Hf -M_α (red) mix elemental mapping. All the images have the same scale as indicated in (D). 118

4.17 Experimental absorptivity/emissivity spectrum of an as-prepared (blue) and ex-situ annealed (red) Ir metamaterial after 1000 °C,100 h. Where λ_c is the cut-off wavelength of the InGaAsSb PV cell at 2.25 μm. 119
4.18 Schematic representing the failure mechanism in a Ir 3-layer-system at different temperature and pressure ranges. (A) As-prepared 3-layer-system, HfO_2 exist in monoclinic and amorphous phase, (B) Amorphous HfO_2 transforms to tetragonal HfO_2, (C) Tetragonal HfO_2 transforms completely into monoclinic HfO_2, resulting in void formation, due to 3.5% increase in unit cell volume, (D) Oxygen molecules travel through the developed transport channel and oxidize Ir forming volatile IrO_x that sublimate, (E) Ir layer is stable with sharp interfaces at (F) Roughness increase at the Ir/HfO_2 interfaces, (G) Ir grains grow more than 30 nm and the layer size increases at 1400 °C for 6 h at 2 × 10^{-2} mbar, and (H) 3-layer-system stable below 1300 °C for 6 h at 2× 10^{-5} mbar. The zone in green represents the area where the 3-layer-system can perform efficiently for a duration over 100 h. 121

A1 W lattice parameter as a function of Temperature 146
A2 Actual temperature versus controller apparent temperature of W heating strip. 147
A3 Actual temperature versus controller apparent temperature of MgO substrate 150
A4 Temperature versus $2\theta_{036}$ of sapphire substrate 152
A5 Actual temperature versus controller apparent temperature of sapphire substrate 153